EFFECT OF LITHIUM COATING ON THE IMPURITIES AND SHIELDING EFFECT OF PLASMA ON THE RESONANT MAGNETIC PERTURBATIONS FIELD IN THE STOR-M TOKAMAK PLASMA

A Thesis Submitted to the College of

Graduate and Postdoctoral Studies

in Partial Fulfillment of the Requirements

for the Degree of Master of Science

in the Department of Physics and Engineering Physics

University of Saskatchewan

Saskatoon

By

Adedapo Joseph Adegun

Permission to Use

In presenting this thesis in partial fulfillment of the requirements for a Postgraduate degree from the University of Saskatchewan, I agree that the Libraries of this University may make it freely available for inspection. I further agree that permission for copying of this thesis in any manner, in whole or in part, for scholarly purposes may be granted by the professor or professors who supervised my thesis work or, in their absence, by the Head of the Department or the Dean of the College in which my thesis work was done. It is understood that any copying or publication or use of this thesis or parts thereof for financial gain shall not be allowed without my written permission. It is also understood that due recognition shall be given to me and to the University of Saskatchewan in any scholarly use which may be made of any material in my thesis.

Requests for permission to copy or to make other use of material in this thesis in whole or part should be addressed to:

Head of the Department of Physics and Engineering Physics

University of Saskatchewan

116 Science Place

Saskatoon, Saskatchewan

Canada S7N 5E2

Abstract

Effects of lithium coating of the chamber wall on the impurities in the STOR-M tokamak plasma were studied in this thesis work. Impurities have been identified as one of the major concerns since the beginning of tokamak plasma research, as they enhance the radiation losses and prevent plasma from being heated to a desired high temperature. The radiation losses are primarily due to line radiation from incomplete stripped impurity ions. Impurities are introduced into the plasma from the walls of the tokamak due to plasma-wall interactions, and the type of impurities observed in a tokamak is partially determined by the kind of material used for the tokamak chamber wall and the gases absorbed in the wall. In the STOR-M tokamak, inner surface walls are made of bare stainless steel, and the major impurities observed are from carbon and oxygen. The emission lines from these impurities are in the visible range of the electromagnetic spectrum. They are CIII which is observable at 464.74 nm, CVI at 529.05 nm, and OV at 650.02 nm.

Before the chamber was coated with lithium, the intensities of the impurity lines were measured and then compared to the intensities after the lithiumization of the chamber wall. The intensities of the impurity lines were recorded during the stable period of plasma before and after the lithium coating using a spectrometer and an intensified charge-coupled device (ICCD) camera. It was observed that the intensities of the impurities reduced during the discharges immediately after the lithium coating. Further experimental analysis revealed that the freshly coated lithium caused plasma density to decrease, and increase after 300 plasma discharge shots. It was also found that after 600 and 900 plasma discharge shots, lithium coating does not appear to play any role in the reduction of the impurity intensities, but repetitive plasma discharge cleaning may be responsible for the decrease in the impurity intensities.

In another experiment, an internal radial magnetic probe array was used to investigate effects of plasma and tokamak chamber wall on resonant magnetic perturbation (RMP) field applied externally to plasma. An internal magnetic probe array was used to measure the magnetic field at four radial locations at plasma edge after the application of RMP current. The plasma response magnetic field measured was subtracted from the vacuum field measured when RMP current was fired without plasma. The time delay caused by the plasma and tokamak chamber wall to the RMP field was also studied by calculating the difference between the RMP current waveform peak time and the magnetic field waveforms peak times in plasma. It was observed that RMP field in vacuum

was 50% larger than the RMP field in plasma, and the penetration time of the RMP fields decreased as they penetrate through the vacuum wall into the plasma. The RMP field was found to travel faster in plasma than in vacuum.

Acknowledgements

I appreciate the God Almighty, who gave me the grace to be part of the plasma physics research group of the University of Saskatchewan for my academic development. I also appreciate the moral and financial support I received from my supervisor, Dr. Chijin Xiao. Thank you for being patient with me, and I appreciate the fact that you did not give up on me even when I gave up on myself, ultimately, thank you for your understanding.

I sincerely acknowledge the International Dean's Scholarship award I received from the college of graduate and postdoctoral studies of the University of Saskatchewan.

I acknowledge the technical assistance I received from David McColl, Jiping Zhang, and all the staff of Physics machine shop. Thank you for your support.

I would also like to acknowledge the assistance of my fellow students, colleagues, and friends; Sayf Gamudi Elgriw, Reza Behbahani, Akbar Rohollahi, Ekow Lewis, Sandeep Bains, Gregory Tomney, Masaru Nakajima, Michael Patterson, Deb Basu, Geoffrey Jacobs, Dotun Oladimeji, Arnab Majumdar, Zahra Abooali, and Adefunbi Kehinde for their undiluted and immeasurable support, words are insufficient to describe how awesome you guys are. You are part of the best people I have ever met in my life. If everybody that populates the earth can be like you guys, this planet earth would be the safest place to live. Thank you for your hands of friendship.

I would like to extend my deepest gratitude to my Dad; Mr. Jacob Adedotun Adegun for his parental role in my life. His effort and words of encouragement to bring the best out of me cannot be quantified; I do not want to imagine what would have happened without you in my life. “Daddy Mi,” as I fondly call you, I am happy to say that your discipline and chastisement contributed positively to what is made of me today. May God keep you for me.

To my siblings: Adedeji, Titilade, Adedoyin, Adeola, and Adejumoke. You guys are the greatest gifts of all, thanks for being there always, I love you all. To my step-mother: Mrs. Folashade Adegun, thank you for the role you played in my achievements, may God bless you. However, a special appreciation goes to my Uncle, Mr. Adetayo Adegun, the best Uncle I ever had. I am so sure without God sending you across my ways; I would not have gone this far. Uncle Tayo, you are indeed a God sent, I am forever indebted to you, and may God keep you for me.

This acknowledgment will be incomplete if I fail to appreciate Prof. Adekunle Adegun and Prof. (Mrs.) Olajire Adegun, my big Mummy; Mrs. Oluremi Adegun, my big Daddy; Mr. Samson Adegun, Mr. David Adeoti, Mr. Adewole Adeoti, Mrs. Olubunmi Adeoti. My cousins, Yemi Adegun, Tosin Adegun, Tobi Adegun, Peter and Paul Adeoti for their financial supports, words of encouragement, and understanding throughout my program. May good God continue to foster the love that binds us together; I love you all.

I will like to appreciate Prof. Matthew F. Ojelabi, my teacher, and a mentor. She supervised my Bachelor degree project work. Thanks for always being there for me ma. You and Dr. Chijin Xiao are the best mentor and teacher I have ever had, thanks for your readiness to assist me every time, may God bless and keep you for me.

Furthermore, I am indebted to Pastor Titus Adedapo and the family, Mr. Ademola Kehinde and the family, Deacon Jonathan Onijingin and the family, Deacon Funso Oderinde and the family, Dr. Marcus Ilesanmi and the family, Mr. Noah Dairo and the family, the youths, the choristers and all the members of the Redeemed Christian Church of God, Grace Sanctuary Parish, Saskatoon. These people are the best body of Christ I have ever fellowshipped with, they are my family, and they are my home. My prayer is that God in His infinite mercy will give us the grace to be partakers of His kingdom at the end our Christian race in this world, keep fighting the good fight of faith.

I would also like to extend my sincere appreciation to Dr. Akira Hirose, the director of the plasma physics laboratory, for his support. Finally, this research work was supported by the grants from the Natural Sciences and Engineering Research Council of Canada (NSERC) and the Sylvia Fedoruk Canadian Centre for Nuclear Innovation.

Dedication

Dedicated to my late Mother: Late (Mrs.) Eunice Adebola Adegun

(1960 - 2006)

TABLE OF CONTENTS

PERMISSION TO USE ..... **I**

ABSTRACT ..... **II**

ACKNOWLEDGEMENTS ..... **IV**

DEDICATION ..... **VI**

LIST OF TABLES ..... **IX**

LIST OF FIGURES ..... **X**

LIST OF ABBREVIATIONS ..... **XII**

LIST OF SYMBOLS ..... **XIII**

CHAPTER 1 ..... **1**

INTRODUCTION **1**

1.1 ENERGY 1

1.2 NUCLEAR FUSION 1

1.3 THESIS MOTIVATION AND OBJECTIVES 5

1.4 THESIS OUTLINE 9

CHAPTER 2 ..... **10**

STOR-M TOKAMAKS AND ITS DIAGNOSTICS **10**

2.1 INTRODUCTION 10

2.2 MAGNETIC CONFINEMENT CONFIGURATION 10

2.3 STOR-M TOKAMAK 14

2.4 STOR-M DIAGNOSTICS 15

2.4.1 Microwave Interferometer 16

2.4.2 Position Sensing Coils 17

2.4.3 Loop Voltage Pickup Coil 18

2.4.4 The Czerny-Turner Spectrometer 19

2.4.5 Helmholtz Coil System 19

2.4.6 Integrator 20

2.4.7 Internal Radial Magnetic Probe Array 23

2.4.8 Rogowski Coil 27

2.4.9 Resonant Magnetic Perturbations (RMPs) Systems 28

2.4.9.1 RMP coil 29

2.4.9.2 Slow Resonant Magnetic Perturbation (SRMP) 30

2.4.9.3 Fast Resonant Magnetic Perturbations (FRMPs) 31

CHAPTER 3 33

EFFECTS OF LITHIUM COATING ON THE IMPURITIES IN THE STOR-M TOKAMAK 33

3.1 INTRODUCTION 33
3.2 PIMAX-3 INTENSIFIED CHARGE COUPLED DEVICE (ICCD) CAMERA 33
3.3 THE SPECTRAPRO-300I IMAGING SPECTROMETER 35
3.4 OPTICAL FIBER BUNDLE 37
3.5 THE STOR-M TOKAMAK'S OVAL PORT 38
3.6 MERCURY-NEON SPECTRAL LAMP 39
3.7 RELATIVE INTENSITY CALIBRATION 39
3.8 MAJOR IMPURITIES IN THE STOR-M TOKAMAK 42
3.9 EXPERIMENTAL DATA ANALYSIS 43
3.10 PLASMA PARAMETERS IN THE STOR-M TOKAMAK DURING NORMAL DISCHARGE 43
3.11 EFFECTS OF LITHIUM COATING ON THE IMPURITIES 44
3.12 EFFECTIVE LIFETIME OF COATED LITHIUM IN THE STOR-M TOKAMAK 49
3.13 EFFECT OF LITHIUM ON PLASMA DENSITY 51

CHAPTER 4 53

SHIELDING EFFECT OF PLASMA ON RMP FIELDS IN THE STOR-M TOKAMAK 53

4.1 INTRODUCTION 53
4.2 SKIN EFFECTS IN PLASMA 53
4.3 EXPERIMENTAL SET-UP 57
4.4 DATA ANALYSIS 60
4.5 EXPERIMENTAL RESULTS 64

CHAPTER 5 69

SUMMARY AND SUGGESTED FUTURE WORK 69

5.1 SUMMARY 69
5.2 SUGGESTED FUTURE WORK 71

REFERENCES 73

List of Tables

Table 2.1: STOR-M tokamak parameters ……15

Table 2.2: Major diagnostics tools installed on the STOR-M tokamak……15

Table 2.3: Calibration factors of the internal magnetic probes…….....26

Table 3.1: Labeling and corresponding minor radius of divided oval port……37

Table 3.2: Relative calibration factors of the optical fiber bundle……41

Table 3.3: Emission lines in the STOR-M tokamak with their transition……..….42

Table 3.4: Quantitative intensity before and after lithium coating……45

Table 4.1: New internal magnetic probe calibration factors…….....57

List of Figures

Figure 1.1: Plot of cross-section against energy for D-T, D-D, and D-He_3 fusion reactions. (The figure is taken from [3])……... 3
Figure 1.2: Suppression of MHD instabilities. (The figure is taken from [11])…… 8
Figure 2.1: Schematic diagram of a tokamak. (The figure is taken from [32])……... 11
Figure 2.2: Particle drifts in a toroidal magnetic field. (The figure is taken from [33])……..12
Figure 2.3: The toroidal (red), poloidal (green) field directions and the resultant helical magnetic field. The resultant twist of the field lines (blue) is exaggerated for illustration purpose. (The figure is taken from [34])……...13
Figure 2.4: Diagnostics ports on the STOR-M tokamak (The figure is taken from [28])……... 16
Figure 2.5: Position sensing coils. (The figure is taken from [38])…… 17
Figure 2.6: Loop voltage pickup circuit. (The figure is taken from [38])……18
Figure 2.7: Pin-out diagram of an operational amplifier (OP-AMP). (The figure is taken from [40])……21
Figure 2.8: Typical active integrator circuit…… 21
Figure 2.9: Schematic diagram of the radial internal probe array and the alumina tube……24
Figure 2.10: Installation of the radial magnetic probe and RMP coil on the STOR-M tokamak…… 25
Figure 2.11: (Left) The magnetic field waveform from the Helmholtz coil. (Right) The uncalibrated signals of the internal radial magnetic probe array……..26
Figure 2.12: Schematic diagram of Rogowski coil with an active integrator. (The figure is taken from [43])…… 27
Figure 2.13: Layout of RMP coil in STOR-M tokamak. (The figure is taken from [11])……30
Figure 2.14: Typical SRMP current waveform……31
Figure 2.15: Typical FRMP current waveform……32
Figure 3.1: Major components of the ICCD. (The figure is taken from [49])……34
Figure 3.2: ICCD camera mounted to an imaging spectrometer…… 35
Figure 3.3: Typical plasma current showing the time when ICCD camera was triggered…….. 35
Figure 3.4: Schematic diagram of an imaging spectrometer……... 36
Figure 3.5: End view of the entrance slit…… 37
Figure 3.6: Schematic diagram of the optical fiber bundle line of view. (Where the center of the chamber is denoted with solid black dot)……... 38
Figure 3.7: Spectrum of Mercury - Neon spectral lamp. The horizontal axis is pixels' number……40
Figure 3.8: Intensity distribution of Mercury-Neon spectral lamp……... 41
Figure 3.9: Plasma parameters during normal discharge……44

Figure 3.10: Intensity profile of CIII before and after lithium coating……45
Figure 3.11: Intensity profile of CVI before and after lithium coating……45
Figure 3.12: Intensity profile of OV before and after lithium coating…… 46
Figure 3.13: Plasma density vs. base pressure before and after lithium……..47
Figure 3.14: Intensity profiles of the impurity lines at different base pressures with lithium (panels on the left), and without lithium (panels on the right)…… 48
Figure 3.15: Intensity of lithium……... 49
Figure 3.16: Line integrated intensity of CIII……...50
Figure 3.17: Line integrated intensity of CVI……..50
Figure 3.18: Line integrated intensity of OV……...51
Figure 3.19: Plasma density with and without lithium…… 52
Figure 4.1: Un-integrated signal of the internal magnetic probes……57
Figure 4.2: Integrated waveform using an analog integrator (left) and digitally integrated waveform (right)……... 58
Figure 4.3: RMP magnetic field in air integrated digitally……...59
Figure 4.4: Plasma current waveform with the red vertical line indicating the time when the RMP current was applied……...60
Figure 4.5: Plasma parameters during disruption: plasma current (left) loop voltage (right)…… 61
Figure 4.6: Digitally integrated magnetic field measured when RMP current was applied in plasma (top) and in vacuum (bottom)……... 62
Figure 4.7: Magnetic field waveform: correction process (left) and corrected waveforms (right)……..63
Figure 4.8: Plasma effect on RMP field……...64
Figure 4.9: RMP field by the magnetic probe array in plasma…… 65
Figure 4.10: RMP field by the magnetic probe array in vacuum…… 66
Figure 4.11: RMP field penetration time…… 66

List of Abbreviations

AWG – American Wire Gauge

BNC – Bayonet Nut Connector

DAQ – Data Acquisition

ELMs - Edge Localized Modes

FB – Feedback

FRMP – Fast Resonant Magnetic Perturbation

GW - Gate Width

ICCD – Intensified Charge-Coupled Device

IDS – Ion Doppler Spectroscopy

IGBT – Insulated-Gate Bipolar Transistor

ITER – International Thermonuclear Experimental Reactor

MATLAB – Matrix Laboratory

MHD – Magnetohydrodynamic

OH – Ohmic Heating

PFCs – Plasma Facing Components

PPL – Plasma Physics Laboratory

RMP – Resonant Magnetic Perturbation

STOR-M – Saskatchewan Torus-Modified

SCR – Silicon-Controlled Rectifier

SRMP – Slow Resonant Magnetic Perturbation

TOKAMAK – TOroidal'naya KAmeras MAgnitnymi Katushkami (from Russian)

List of Symbols

C – Capacitance

c – Speed of light

B – Magnetic field

E – Electric field

e – Electron charge

B_θ – Poloidal Magnetic field

B_t – Toroidal Magnetic field

I_p – Plasma current

V_l – Loop voltage

Δm – Mass defect

n_e – Electron density

R – Major radius

R_p – Plasma resistance

r – Minor radius

I_{RMP} – RMP current

T – Tritium

D – Deuterium

m – Poloidal mode number

n – Toroidal mode number

P_b – Base pressure

p – Proton

n – Neutron

He – Helium

Li – Lithium

L_p – Plasma inductance

m_e – Electron mass

ms - Millisecond

T_e – Electron temperature

τ_E – Energy confinement time

δ – Skin depth

τ – Penetration time

ΔH – Plasma position

Z – Ion charge number

eV - Electron volt

β_p - Plasma poloidal beta

μ_0 – Permeability of free space

ω – Frequency

λ – Wavelength

$ln\Lambda$ - Logarithmic coulomb

Chapter 1

Introduction

1.1 Energy

Clean, abundant, and cheap energy is one of the critical factors defining the development of a country. The importance of energy cannot be overemphasized due to the multiple ways it is used in improving living standards. Energy is required for the production of foods, lighting, heating of homes, offices, industries and hospitals, lighting up streets, operating telecommunication systems, and in many other aspects affecting the living standard. In general, energy is fundamental to daily life, and its abundance at an affordable price means a high quality of life. With the recognition of the importance of energy to life, many of the countries in the world today, especially underdeveloped and developing countries, understand their difficult energy situation and the likelihood that their problems will get worse due to population increase and development if there is a lack of sufficient energy to meet the needs of these countries.

There are many sources of energy that can meet global energy demand. These include energy from the fossils, the wind, the Sun, geothermal, hydropower, nuclear fission and nuclear fusion. Amongst all these sources of energy in the world, nuclear fusion has been predicted to be the most abundant source of energy which will meet global energy demand when fusion reactors become a viable means of generating electricity.

1.2 Nuclear Fusion

Nuclear fusion energy has been predicted to be the future primary power source. In the past, uncontrolled nuclear fusion reactions in the form of thermonuclear explosions using isotopes of hydrogen have been achieved on Earth, meanwhile if fusion energy were harnessed on Earth in a controlled manner, it could produce virtually inexhaustible clean energy without direct greenhouse gas emissions, no proliferation risk, no danger of catastrophic accidents, and radioactive waste is at a very low level and indirect. Unlike most fission reactors, a nuclear fusion reactor holds only a small amount of fuel at any given time and is therefore completely safe without a risk of meltdown or runaway chain reactions. A loss of control in a nuclear fusion reactor means a stop of the energy output.

Nuclear fusion is the fusing of light nuclei to form a heavier nucleus producing a significant amount of energy. The energy released during a nuclear fusion reaction is calculated by the Einstein equation;

$$\Delta E = \Delta m c^2 \tag{1.1}$$

Where Δm is the mass defect of nuclei involved in the fusion reaction and c is the speed of light. A good example of where fusion occurs naturally and continuously is within the Sun and the stars. However, on Earth, in the laboratory to be precise, nuclear fusion can be achieved by fusing isotopes of hydrogen atom together. Some of the examples of the fusion reactions are listed below [1]:

$$^{2}_{1}\mathrm{D} + {}^{3}_{1}\mathrm{T} \rightarrow {}^{4}_{2}\mathrm{He}(3.5\ \mathrm{MeV}) + {}^{1}_{0}\mathrm{n}(14.1\ \mathrm{MeV}) \tag{1.2}$$

$$^{2}_{1}\mathrm{D} + {}^{2}_{1}\mathrm{D} \rightarrow {}^{3}_{1}\mathrm{He}(0.82\ \mathrm{MeV}) + {}^{1}_{0}\mathrm{n}(2.45\ \mathrm{MeV})\ \ (50\%) \tag{1.3}$$

$$^{2}_{1}\mathrm{D} + {}^{2}_{1}\mathrm{D} \rightarrow {}^{3}_{1}\mathrm{T}(1.01\ \mathrm{MeV}) + {}^{1}_{1}\mathrm{p}(3.02\ \mathrm{MeV})\quad (50\%) \tag{1.4}$$

$$^{2}_{1}\mathrm{D} + {}^{3}_{2}\mathrm{He}\ \rightarrow {}^{4}_{2}\mathrm{He}(3.6\ \mathrm{MeV}) + {}^{1}_{1}\mathrm{p}(14.7\ \mathrm{MeV}) \tag{1.5}$$

Where He is Helium, n is a neutron, p is a proton, D is deuterium, and T is tritium. All of these reactions occur when the fuels are heated to high temperatures. In Equation 1.3 and 1.4, the reaction of D-D has two branches, each of the branches has 50% chance, that is the product of D-D reaction can either result in a $^{3}_{2}\mathrm{He}$ and a neutron or in a $^{3}_{1}\mathrm{T}$ and a proton.

Among the reactions stated above, Equation (1.2) to Equation (1.5), the most preferred reaction for a fusion reactor is Equation 1.2, the fusion of deuterium and tritium (D-T) which produces an alpha particle with the release of a neutron and large amount of energy of 17.6 MeV per reaction (energy of both alpha particle and a neutron). Besides appreciably higher reactivity, (reactivity is the probability of reaction per unit time per unit density of target nuclei, and it is given by the product of $<\sigma v>$ averaged over velocity, where σ is the cross section and v is the speed of the particles), occurs in this reaction at lower temperatures compared to D-D and D-He_3 reactions. Figure 1.1 shows the plot of cross-section against energy for some prominent fusion reactions.

The deuterium fuel that is used in the fusion reaction is plentiful and virtually inexhaustible. Deuterium is found as the so-called heavy water mixed in natural water. Tritium, on the other hand,

does not occur naturally on earth because it is neutron-rich and is therefore unstable to beta decay with a half-life of 12.3 years. Tritium can, however, be bred from lithium using neutron produced during fusion reactions [2]. The relevant exothermic and endothermic reactions that are involved in the breeding of tritium are:

$$^{6}_{3}\mathrm{Li} + ^{1}_{0}\mathrm{n} \rightarrow ^{4}_{2}\mathrm{He} + ^{3}_{1}\mathrm{T} + 4.8\ \mathrm{MeV} \tag{1.6}$$

$$^{7}_{3}\mathrm{Li} + ^{1}_{0}\mathrm{n} \rightarrow ^{4}_{2}\mathrm{He} + ^{3}_{1}\mathrm{T} + ^{1}_{0}\mathrm{n} - 2.5\ \mathrm{MeV} \tag{1.7}$$

The neutron in the reactant of the Equation 1.6 and 1.7 is the neutron that was produced by the D-T fusion reaction in Equation 1.2. The neutron reacts with lithium contained in the blanket surrounding the reactor core where D-T reactions occur, and then breeds tritium. The tritium reacts with deuterium to produce fusion energy, and the cycle of reaction continues with deuterium and tritium as the net fuels. The energy released during the D-T fusion reaction can be used either to heat the fuel or to be absorbed by the same lithium blanket, transforming the energy into heat which is then carried away by a suitable coolant to drive turbines to generate electricity.

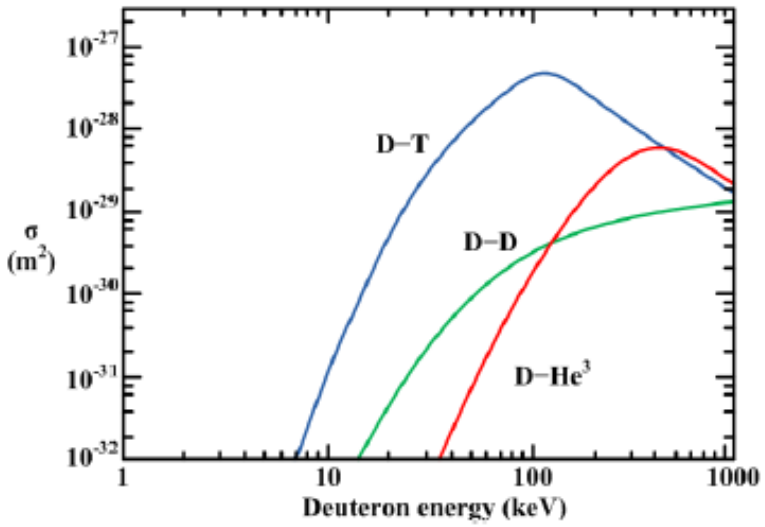

Figure 1.1: Plot of cross-section against energy for D-T, D-D, and D-He_3 fusion reactions. (The figure is taken from [3]).

As it is seen in Figure 1.1, the D-T reaction reaches the highest cross-section at the lowest temperature compared to D-D and D-He_3 reaction. Besides D-T fusion reaction releases a large amount of energy compared to all other conventional sources of energy on Earth including wind,

solar, fossil fuels, geothermal, nuclear fission. For example, the energy released when hydrogen reacts with oxygen is about 2.96 eV:

$$2H_2 + O_2 \rightarrow 2H_2O + 2.96\ \text{eV} \tag{1.8}$$

whereas, the energy released by the D-T fusion per reaction is about 17.6 MeV (Eq. (1.2)) which is 10^7 orders of magnitudes higher than the energy released per chemical reaction as in Equation 1.8.

To make a fusion reactor works on earth, conditions of sufficiently high temperature and density must be created, and the fusion reactants must be held confined enough for a sufficiently long time. The fuels at high temperature are in the ionized state called plasma. There are two main approaches to confine fusion reactants: magnetic confinement approach and inertial confinement approach. Magnetic confinement approach is to date the most promising approach to confine fusion reactants. There are different magnetic confinement configurations including tokamaks, stellarators, reversed field pinch devices, and spheromaks. The most successful and technically mature way of confining the fusion reactant among these devices is tokamak. A tokamak is a torus shaped device which uses a magnetic field to confine a plasma at high temperatures. Tokamak, amongst all magnetic confinement configurations, currently holds the record of longest confinement time. It has been demonstrated in the Experimental Advanced Superconducting Tokamak (EAST) that a tokamak can sustain a fusion reaction for 102 seconds [4].

In an attempt to prove that nuclear fusion reactor works, the European Union, India, Japan, China, Russia, South Korea and the United States in 2006 signed an agreement to jointly build the world's largest experimental tokamak fusion reactor in Cadarache, France. The project is called International Thermonuclear Experimental Reactor (ITER). The project is aimed at demonstrating the feasibility of a fusion energy with a net energy gain [5]. To achieve this goal, some problems that are associated with the tokamak reactors must be solved before the technology is available for commercial use.

One of the problems is the development of the tokamak wall materials to withstand the heat fluxes from the plasma [6]. The thermal heat fluxes from the plasma can cause melting of components such as divertor plate and guard limiter for the radio-frequency (RF) antenna, which then leads to the liberation of impurities. The type of impurity liberated in tokamaks is determined by the kind

of the tokamak wall materials. The plasma-facing walls for some large tokamaks such as National Spherical Torus Experiment (NSTX) are made from carbon tiles [7], and some of the major impurities observe in tokamaks generally are of carbon, iron, and oxygen.

Another important issue for a tokamak fusion reactor is the magnetohydrodynamic (MHD) instabilities. One of the causes of MHD instabilities is a misalignment of toroidal magnetic field coils. MHD instabilities destroy plasma magnetic surfaces, degrade plasma confinement, and cause abrupt termination of tokamak discharge [8]. However, application of external radial magnetic fields called resonant magnetic perturbations (RMP) is one of the methods used to suppress the MHD activities.

1.3 Thesis Motivation and Objectives

The experiments reported in this thesis work were conducted on the Saskatchewan Torus-Modified (STOR-M) tokamak, the only tokamak currently in operation in Canada. Most recent experiments carried out on the STOR-M tokamak are compact torus injection [9], measurement of toroidal flow velocity [10], suppression of Mirnov instabilities [11], and lithium coating among other experiments. The details of the STOR-M tokamak will be introduced in Chapter two of this thesis.

In this section, the motivations for the study of the effect of the lithium coating on the impurity content of the STOR-M tokamak discharge and the shielding effect of plasma on the penetration of the Resonant Magnetic Perturbation (RMP) field will be discussed.

The problems of impurities in tokamak plasmas have been recognized since the start of nuclear fusion research. In early experiments, in which glass vacuum vessels were used to hold plasma, impurities released from the walls of the glass surface prevented the plasma from being heated above 50 eV [1]. In the case of tokamaks with the inner walls made from carbon tiles or stainless steels, the released impurities are often carbon, oxygen, or iron depending on the type of the material used for plasma facing components. When the impurities released by plasma-wall interactions enter the plasma, they are ionized upon colliding with hot plasma. The energy loss from the plasma is enhanced by impurities through the enhanced line emission, Bremsstrahlung radiation, and recombination radiation, leading to cooling of the plasma temperature.

When plasma interacts with the incompletely stripped ion of the impurities, plasma energy is lost through line emission. The electron energy state can be excited through collisions with electrons or ions in the plasma, and light is emitted during the transition from the excited energy state to the lower energy state. The wavelength of the line emission is the fingerprints of the types of impurities and its ionization stage. Also, plasma energy is also lost through Bremsstrahlung radiation when electrons are accelerated upon scattering by the impurity ions. Bremsstrahlung continuum radiation power is proportional to the charge Z of the impurity ions as shown in Equation 1.9 [12].

$$P_{Br} = 1.69 \times 10^{-32} n_e Z^2 {T_e}^{1/2} \tag{1.9}$$

where n_e is the electron density, T_e the electron temperature, and Z the charge state of the ion. With a large density of high Z impurities in the tokamak, energy loss is greatly enhanced through Bremsstrahlung radiation. Concurrently, the line emission from different ionization stage of the impurities is also enhanced and observable (which is the focus of this research work).

Lithium, on the other hand, is one of the most important elements that is very useful in nuclear fusion experiments. Besides being used to breed tritium [13-15], lithium can be used to coat the inner surface walls of tokamak to avoid the direct bombardment of energetic particles on the bulk material of the tokamak chamber wall. Lithium is a chemical element with a low atomic number of $Z = 3$. It is a soft, silver-white metal that belongs to the alkali metal on the periodic table. Lithium has a melting point of 180 ℃ and boiling point of 1330 ℃. Lithium has one electron in its outermost shell ([He]$2s^1$), thus it is highly reactive, for example, for hydrogen retention [16]. It also has a strong chemical activity for effectively trapping gas impurities such as O_2, N_2, CO, H_2O and CO_2 [16]. Because of its low atomic number Z, lithium, unlike carbon, iron, and oxygen, gives lowest possible energy loss by radiation through Bremsstrahlung continuum radiation or line radiation even if it ends up in the plasma [17].

Lithium coating was used on Current Drive eXperiment-Upgrade (CDX-U) device in the year 2005. The bottom of the chamber of this machine was filled with liquid lithium, and during the series of experiments performed in that year, the highest energy confinement time in the history of the machine was recorded. The energy confinement time of the device increased by a factor of six [18]. This result led to the construction of Lithium Tokamak Experiment (LTX) device.

LTX is an upgraded version of CDX-U with an increased vertical field supplied by the addition of the internal field coils. It had its first operation (plasma discharge) without lithium-coated walls in 2008 [19], and its first plasma with lithium-coated walls in 2010 [18].

The effects of lithium-coated walls on LTX are [20]

- Increased plasma currents (from 15 kA to about 50 kA) with freshly coated lithium.
- Absorption of the neutral particles (plasma fuel). The decrease in plasma density.
- Long plasma discharge time (more than 15 ms compared to less than 10 ms with bare stainless-steel wall).
- Reduction in the neutral flux into the plasma from the wall.
- Reduction in the H_α emission, an indication of reduced hydrogen fuel released from the chamber wall.

Moreover, it was reported in National Spherical Torus Experiment (NSTX) device that line emission from carbon and oxygen were reduced following the introduction of lithium [21]. Subsequent results from the experiment conducted on NSTX, in both normal (L) and improved confinement (H) mode regime after the introduction of lithium showed that plasma particles were better controlled, inductive flux consumption was decreased, electron temperature, ion temperature, and energy confinement time were increased, plasma density was decreased, and neutron production rate in the deuterium plasma was increased. It was also observed that the unwanted Edge Localized Modes (ELMs) activity was completely suppressed in the H-mode regime after a continuous increase in lithium coverage on the tokamak wall [17]. Meanwhile, reduction in the intensity of OI, OV, and Fe-XV impurity lines and an increase in plasma electron temperature were observed in Aditya tokamak [22]. Besides results similar to what has been seen in the tokamaks discussed above have also been observed in EAST [23], HT-7 [24], TJ-II (stellarator) [25], TFTR [26], and FT-U [27] devices.

The average electron temperature in the STOR-M tokamak was measured up to 220 eV at the plasma center and around 20 eV at the plasma edge [28]. It is well known that the ionization stage depends on the electron temperature in the plasma. At this temperature, bright emission lines from carbon and oxygen (CIII, CVI, and OV) [10] are observable in the tokamak at different radial

locations, and these line emissions will be used to characterize the effect of lithium coating on the impurity contents in the STOR-M tokamak plasma.

In the STOR-M tokamak, a resonant magnetic perturbation (RMP) systems have been used to suppress magnetohydrodynamic (MHD) activities [11]. The RMP field is induced during plasma discharge by passing a current pulse through a set of coils installed outside the STOR-M vacuum chamber. The details of the RMP systems will be discussed in Chapter two under the diagnostics installed on the STOR-M tokamak. It was observed during the RMP experiment that suppression of MHD activities, represented by the reduction of the amplitude of the oscillating magnetic field ($\dot{\widetilde{B_\theta}}$) measured, did not occur immediately as shown in Figure 1.2. The delay in suppression was attributed to the time delay of the RMP field to penetrate the plasma and the chamber wall since the application of any externally applied field to plasma will experience attenuation and time delay because of the conducting chamber wall and the plasma.

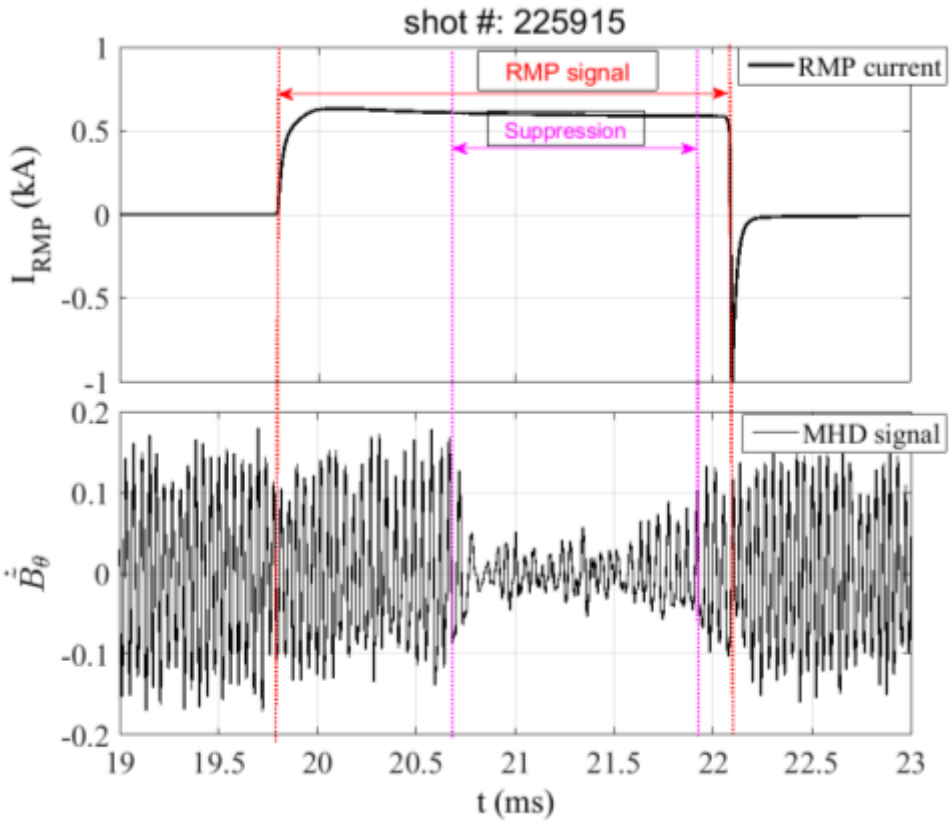

Figure 1.2: Suppression of MHD instabilities. (The figure is taken from [11]).

The trace on the top shows that the RMP current is applied during the discharge between 19.8 ms and 22.1 ms. The trace on the bottom illustrates the delay of ~ 1 ms between the onset of the suppression of the magnetic fluctuation and the start of the RMP current pulse.

In this thesis work, effects of lithium coating on the impurities in the STOR-M tokamak will be investigated based on the intensity of line radiation from impurities. We will also examine the shielding effect of STOR-M tokamak chamber walls and the plasma on the resonant magnetic perturbation (RMP) fields using an array of the internal radial magnetic probe. More specifically the following tasks have been completed during the research:

i. Set-up, installation, and calibration of a newly acquired intensified charge-coupled device (ICCD) camera.
ii. Development of a MATLAB script to analyze the results recorded by the ICCD camera.
iii. Design, installation, and calibration of an internal radial magnetic probe array to study the plasma effects on RMP field.

1.4 Thesis Outline

In the first chapter, an introduction to nuclear fusion energy was explained, the motivation for the thesis was discussed, and the thesis goals were presented.

Chapter 2 introduces tokamak and its principles of operation. Specifically, the features of the STOR-M tokamak, the RMP coil system, the available diagnostics will be discussed and introduced. The design and the calibration of the internal radial magnetic probe used during this research will be described.

Chapter 3 presents the set-up of the intensified charge-coupled device (ICCD) camera the results of the lithium coating experiment.

Chapter 4 presents the results of the shielding effect of STOR-M tokamak chamber wall and plasma on RMP fields.

Chapter 5 summarizes the major findings of this research and also suggests future work.

Chapter 2

STOR-M Tokamaks and its Diagnostics

2.1 Introduction

Tokamak was a brilliant idea of Oleg Lavrentiev, but it was invented by two Soviet physicists Igor Tamm and Andrei Sakharov in the 1950s [29]. Tokamak is an acronym from Russian for TOroidal'naya KAmeras MAgnitnymi Katushkami which means toroidal chamber with axial magnetic coils; it can also be abbreviated as "tochamac" in English [30]. Tokamak is a toroidal plasma confinement system; it employs both internally produced magnetic field and the magnetic field generated by external coils to confine the high temperature and high-density plasma. Plasma is known as the fourth state of matter and is defined as a quasi-neutral gas of charged and neutral particles characterized by a collective behavior [31].

In this chapter, the working principle of tokamaks, in general, will be explained. The STOR-M tokamak, its parameters, the RMP system, and the installed diagnostics will be presented. The active integrator and the internal magnetic probe that was designed for the experiment reported in this thesis will be described in sections 2.4.6 and 2.4.7 respectively.

2.2 Magnetic Confinement Configuration

Tokamak is one of the magnetic confinement configurations that are used for plasma confinement. It works on the principle of a rotating motion of charged particles around the magnetic field lines, preventing the free movement across the magnetic field lines. Tokamak is a donut-shaped device. The primary magnetic field in a tokamak is the toroidal field B_t (in larger circumference direction in Figure 2.1), which circles around the torus. The toroidal field is generated by driving a current through the magnetic coils oriented in the poloidal direction (blue rings in the smaller circumference direction) as shown in Figure 2.1. The toroidal field alone is not sufficient for the confinement of plasma because a pure toroidal magnetic field in a tokamak is not uniform in all area of the vacuum vessel. The magnetic field is higher at the inner side of the torus, and smaller at the outer side of the torus. The inner side of the torus is regarded as high field side (HFS), and the outer side is known as low field side (LFS). Because of the inhomogeneous field, there is a gradient in the inward direction of the toroidal chamber which leads to Grad-B particle drift in the

vertical direction, and the drift direction depends on the polarity of the charged particle. The Grad-B drift is expressed as

$$\vec{v}_{\nabla B} = -\frac{mv^2}{2q}\frac{\nabla B \times \vec{B}}{B^3} \tag{2.1}$$

where *m* is mass of the charged particle, *v* is the perpendicular components of the particle velocity relative to the magnetic field, and *B* is the toroidal magnetic field.

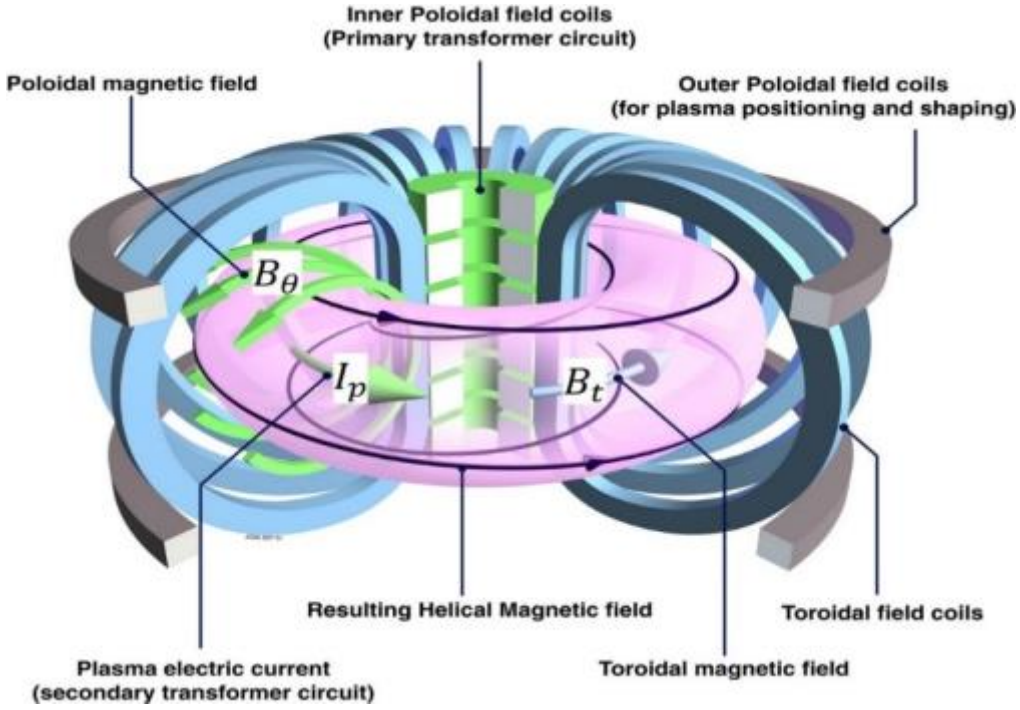

Figure 2.1: Schematic diagram of a tokamak. (The figure is taken from [32]).

In a tokamak with only a toroidal magnetic field, positively charged ions drift upward, and negatively charged electrons drift downward. In the configuration shown in Figure 2.2, the electrons (ions) drift downwards (upwards) producing a downwards electric field.

In the magnetized plasma, there exists another drift called $\vec{E} \times \vec{B}$ drift with a drift indepent of the sign of the charge.

$$v_{E\times B} = \frac{\vec{E}\times\vec{B}}{B^2} \tag{2.2}$$

where $\vec{E}$ is the electric field created by charge separation, and $\vec{B}$ is the magnetic field in the toroidal direction. The Grad-B drift and the $\vec{E} \times \vec{B}$ drift are shown in the Figure 2.2;

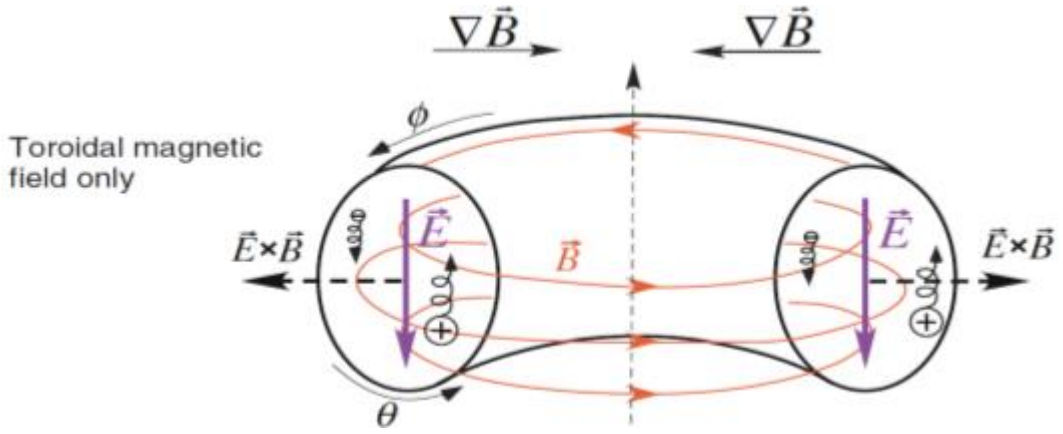

Figure 2.2: Particle drifts in a toroidal magnetic field. (The figure is taken from [33]).

The combined Grad-B drift and the $\vec{\boldsymbol{E}} \times \vec{\boldsymbol{B}}$ drift cause the whole plasma to drift towards the outer side of the torus, leading to the unwanted particle loss as shown in Figure 2.2. To avoid the drifts described above, a poloidal magnetic field B_θ is needed. This poloidal magnetic field is produced mainly by the plasma current. The poloidal magnetic field direction is orthogonal to the toroidal field as shown in Figure 2.1. The plasma current I_p is induced by a transformer action, with the inner poloidal magnetic field coil in Figure 2.1 acting as the primary winding and the plasma as the secondary winding. This plasma current flows in the toroidal direction, and induces magnetic field in the poloidal direction called the poloidal field B_θ. This current and field are shown in Figure 2.1 (the current highlighted in green in the toroidal direction, and the associated field highlighted in green in the poloidal direction). The toroidal field B_t combines with the poloidal field B_θ to form a helical magnetic field around the chamber torus and then confines the plasma. Figure 2.3 shows the schematic diagram of the toroidal field, the poloidal field and the resultant exaggerated helical magnetic field. The role of the helical magnetic field is to guide the charged particle to flow along the magnetic field line to neutralize the charge accumulation on the top or bottom so the downward electric field is "shorted-out".

Although the poloidal magnetic field is much smaller than the major toroidal magnetic field, $B_\theta \ll B_t$, it has to be maintained during the discharge by the plasma current for the resultant helical magnetic field lines to confine plasma. For steady-state tokamak operation, the plasma current has to be maintained by the non-inductive methods.

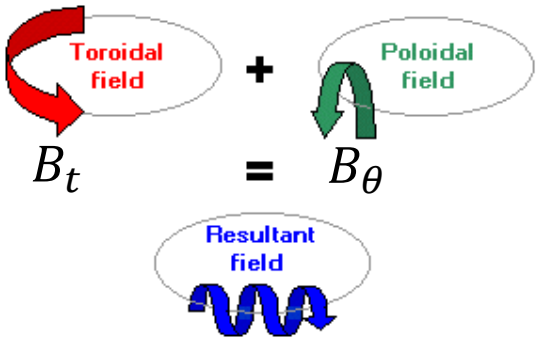

Figure 2.3: The toroidal (red), poloidal (green) field directions and the resultant helical magnetic field. The resultant twist of the field lines (blue) is exaggerated for illustration purpose. (The figure is taken from [34]).

In Figure 2.1, the outer poloidal fields coils (gray) are responsible for plasma positioning and shaping; they guide the plasma along the magnetic field axis.

In tokamaks, there is a need to heat plasma enough to enable deuterium and tritium fusion reactions as explained in Chapter 1. The required temperature to heat plasma is in the range of 10-30 keV [1]. The major primary plasma heating comes from the plasma current itself; this type of heating is called Ohmic heating. Ohmic heating becomes inefficient at high temperatures because the plasma conductivity increases with the temperature [35]. Other forms of plasma heating are necessary to achieve the required temperature for fusion reactors. The common heating methods include:

- Neutral beam injection (NBI). This involves injecting neutral atoms at high speed into the plasma. The neutral atoms get ionized and trapped by the magnetic field when they get into the plasma, and they transfer their energy to the plasma and heat it.
- Radio frequency (RF) heating. This involves transferring large amounts of energy to the plasma when high-frequency oscillating currents are induced in the plasma by external coils.
- Ultimately, during the steady-state self-burning operation in a tokamak, the 3.5 MeV He particle produced in the reaction shown in Equation (1.2) will be utilized for heating the plasma.

2.3 STOR-M Tokamak

The Saskatchewan Torus Modified (STOR-M) tokamak is currently the only tokamak device in operation in Canada. It is a small iron core tokamak built in the year 1987 [36]. A limiter, which is made up of stainless steel, is installed on the inner wall of the STOR-M tokamak chamber to prevent plasma from having direct contact with the chamber wall. This limiter reduces the minor radius of the tokamak from 16.2 cm to 12 cm. A base vacuum of about 6.0×10^{-8} Torr (1Torr=133.3 Pa) can be achieved by using a rotary pump and a turbo-molecular pump. The STOR-M tokamak uses pure hydrogen gas to make plasma. The hydrogen gas is constantly fed to the chamber through a piezoelectric valve to maintain a base pressure that ranges from 0.6×10^{-4} to 1.2×10^{-4} Torr during discharge. The toroidal magnetic field of the STOR-M tokamak is produced by a set of evenly spaced 16 circular coils located outside the chamber of the tokamak. The coils have a total inductance and resistance of 2.06 mH and 13.5 Ω respectively. Each of the 16 coils has 9 turns of copper conductor with cross section of $70 \times 6.4\ mm^2$. The toroidal field coils are powered by a capacitor bank of 15 mF that can be charged to up to 7 kV to produce a toroidal magnetic field B_t between 0.5-1 T. In the STOR-M tokamak, plasma heating is achieved mainly by ohmic (OH) heating. The ohmic heating coil circuit consists of a fast bank (450 V, 200 mF) and slow bank (100 V, 10 F). The fast bank is used for initial gas ionization and current ramp-up, while the slow bank is used to sustain a relatively constant plasma current. The position of plasma is controlled by a vertical magnetic field provided by an image current on the chamber and a pre-programmed and feedback-controlled vertical field [37]. Typically, the toroidal field B_t and ohmic heating capacitor banks are charged in 2 minutes 50 seconds and are discharged within approximately 40 ms. There is an approximately one-minute time for data transfer and for all the capacitor banks to cool down. The parameters of plasma are measured during the discharged time using the appropriate diagnostics tools. Table 2.1 lists the plasma parameters of the STOR-M tokamak during normal discharge.

Table 2.1: STOR-M Tokamak parameters.

PARAMETERS	SYMBOLS	VALUES
Major radius	R (cm)	46
Minor radius	r (cm)	12
Toroidal magnetic field	B_t (T)	0.5-1
Plasma current	I_p (kA)	20-50
Average electron density	n_e (m^{-3})	10^{19}
Electron temperature	T_e (eV)	220
Ion temperature	T_i (eV)	50
Discharge time	τ_D (ms)	40
Energy confinement time	τ_E (ms)	2-5

2.4 STOR-M Diagnostics

The parameters of the plasma in the STOR-M tokamak are measured using different probes, some of these probes are installed internally to measure the plasma parameters at the colder region (edge) while some are used outside the chamber. The diagnostics tools that are installed both internally and externally into the STOR-M tokamak are listed in Table 2.2, and Figure 2.4 shows the various diagnostics locations on the tokamak.

Table 2.2: Major diagnostics tools installed on the STOR-M tokamak.

PLASMA PARAMETER	DIAGNOSTICS TOOLS
Currents (Plasma, RMP, etc.)	Rogowski Coils
Loop voltage	Pickup Coils
Electron density	4 mm Microwave Interferometer
MHD fluctuations	Mirnov Coils
Plasma position	Position Sensing Coils
Toroidal flow velocity	Ion Doppler Spectroscopy (IDS)
Magnetic field	Magnetic Probes
MHD instabilities	Resonant Magnetic Perturbation System

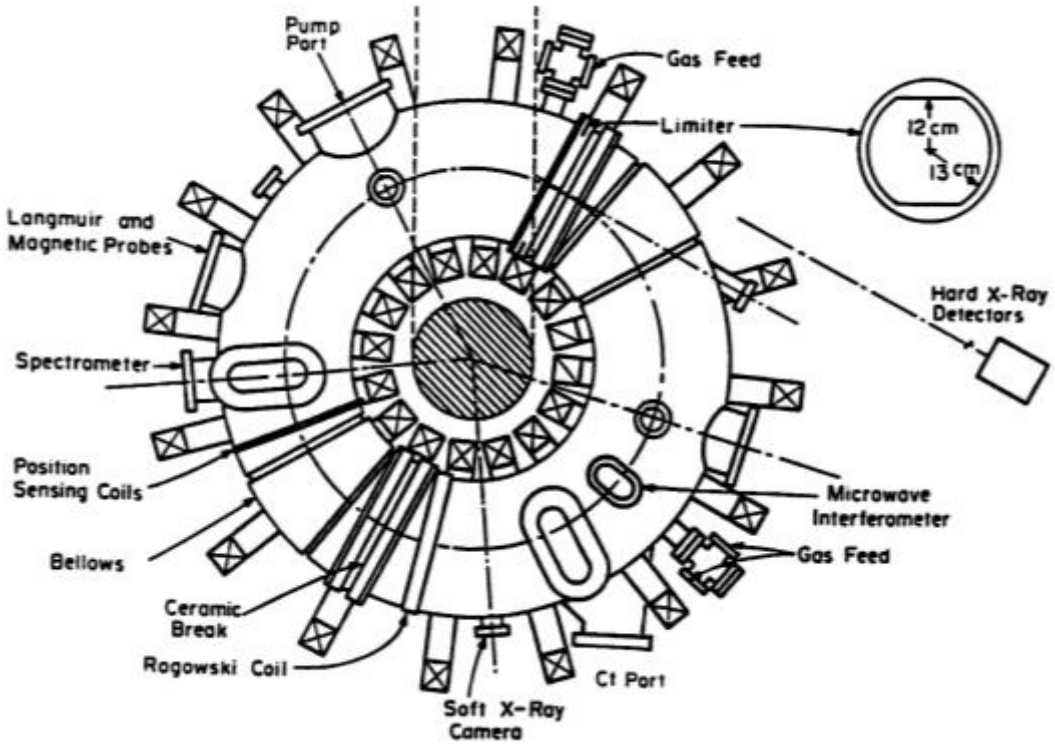

Figure 2.4: Diagnostics ports on the STOR-M tokamak (The figure is taken from [28]).

2.4.1 Microwave Interferometer

Microwave interferometer is a non-invasive system used on the STOR-M tokamak to measure the line-averaged electron density in the plasma. A Gunn diode microwave source operating at the frequency of 75 GHz is utilized for the density measurement. The microwaves are divided into three paths with one path going through the plasma, and the other two paths serving as the reference waves. The wave going through the plasma experiences a phase shift relative to the reference waves in vacuum. The phase shift caused by the plasma path is calculated theoretically as

$$\Delta\phi = \frac{2\pi}{\lambda}\int\left(1-\sqrt{1-\frac{n_e(x)}{n_c}}\right)dx \tag{2.3}$$

where λ is the wavelength of the microwave, $n_e(x)$ is the local electron density and n_c is the cut-off electron density. The cut-off electron density is given by

$$n_c = \frac{m\varepsilon_0\omega^2}{e^2} \tag{2.4}$$

where m is a mass of the electron, ω is the frequency of microwave, ε_0 is the permittivity of free space and e is the electron charge.

At an electron density n_e less than the cut-off density n_c, the microwave will propagate through the plasma, otherwise, the wave will not propagate.

2.4.2 Position Sensing Coils

The quality of plasma discharge depends on the position of the plasma column at any given time. In the STOR-M tokamak, plasma position is measured using six magnetic coils installed outside the vacuum chamber at a minor radius, r = 17 cm as shown in Figure 2.5. The position information is then used to control the position of plasma through feedback algorithm.

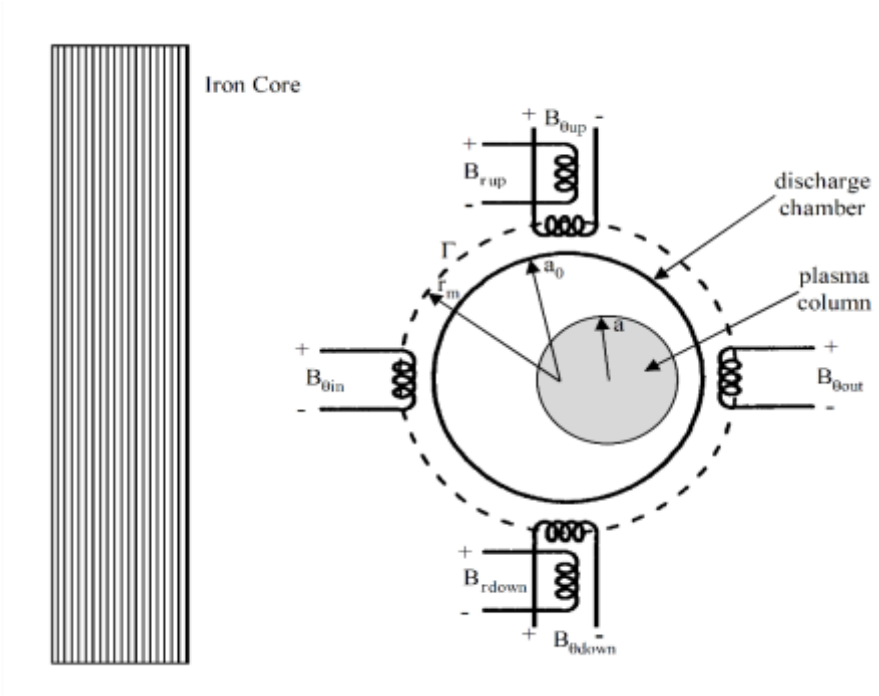

Figure 2.5: Position sensing coils. (The figure is taken from [38]).

Four of the magnetic coils, as shown in Figure 2.5 above, are arranged to detect poloidal magnetic field B_θ at different poloidal angles 90°. The remaining two magnetic probes are oriented to detect the radial component of the magnetic field B_r at an angle = ±90° at the top and bottom. Also, the position sensing coils pick up stray fields that come from misalignment and imperfections of the

toroidal coil system. A compensation circuit is used to eliminate the unwanted signal. This is done by measuring the current waveforms that produce the stray field with a Rogowski coil, and then add (subtract) the waveforms to (from) the position sensing coils output signals to cancel out the unwanted magnetic field contribution.

2.4.3 Loop Voltage Pickup Coil

The coil provides a measurement of the loop voltage of the plasma. The loop voltage is needed to estimate how resistive and hot the plasma is. The loop voltage coil on the STOR-M tokamak is a single turn loop, and it is installed on the top of the vacuum chamber parallel to the plasma current direction. A voltage divider is used to match the output voltage signal to the data acquisition. Figure 2.6 shows the schematic diagram of the loop voltage circuit installed on the STOR-M tokamak. The measured loop voltage of the plasma contains the plasma resistance and the plasma inductance contributions. The expression to calculate of the loop voltage is

$$V_l = R_p I_p + \frac{d(L_p I_p)}{dt} \tag{2.5}$$

where I_p is the plasma current, R_p the plasma resistance, and L_p the plasma inductance. During the current flat-top, the time derivative term in Eq. (2.5) can be ignored.

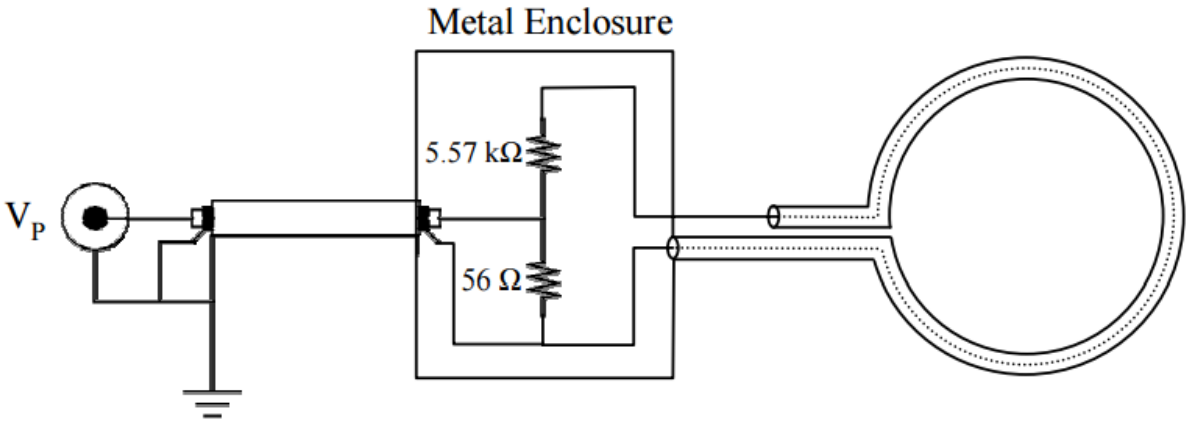

Figure 2.6: Loop voltage pickup circuit. (The figure is taken from [38]).

2.4.4 The Czerny-Turner Spectrometer

The Czerny-Turner spectrometer is used to measure the time evolution of the intensity of line emissions during the plasma discharges. The system consists of a photomultiplier tube (PMT), an optical fiber, and a spectrometer. The spectrometer has two concave mirrors. The light collected from the plasma by an optical fiber cable is conveyed to the input slit of the spectrometer, the light is then collimated by the first concave mirror to a grating with a groove density of 1200 grooves/mm for diffraction. The last concave mirror focuses the diffracted light to the exit port of the spectrometer. The diffraction grating is mounted on a manual motor drive with adjustable wavelength scanning whose speed ranging from 0.04 nm/min to 100 nm/min. The entrance slit of the spectrometer can be increased up to 3 mm with a division of 2 μm. The output line emission spectral profile from the spectrometer is detected and recorded by a photomultiplier tube (PMT) array. The PMT works on the principle of the photoelectric effect. It consists of photocathode, dynodes, and anode. The photomultiplier tube can detect light in the wavelength range between 165 nm and 850 nm. The Czerny-Turner spectrometer has been used to measure the toroidal flow velocity in the STOR-M tokamak based on Doppler shift [10]. In this thesis work, the spectrometer system will be used to measure the integrated intensity of lithium, the result of the measurement is reported in Chapter 3 of this thesis work.

2.4.5 Helmholtz Coil System

A Helmholtz coil system, which consists of two coils of the same radius and separated by a distance equal to the radius of the coil on the same axis, is used to produce nearly uniform magnetic field between the coils. It was named after the German physicist Hermann von Helmholtz [39]. The Helmholtz coil system in the Plasma Physics Laboratory at the University of Saskatchewan consists of a capacitor bank (8 mF, 80 V), an inductor (110 μH), a trigger circuit and a Silicon-Controlled Rectifier (SCR) switch. The capacitor bank can be charged to 80 V to drive a current of about 230 A. The voltage is discharged into an inductor through an SCR switch connected in series to it. The Helmholtz coils have a radius of 15 cm, and the distance between the two coils is 15 cm. There are ten turns of the coil in each of the coils. The uniform magnetic field produced at the center of the coil is calculated by the Equation 2.6:

$$B = \left(\frac{4}{5}\right)^{\frac{3}{2}} \frac{\mu_0 NI}{R} \tag{2.6}$$

Where μ_0 is permeability of free space, N is a number of turns, I is current to the coils, R is the radius of the coil. The current depends on the charging voltage, and the current was already calibrated against the Pearson probe previously. Using Equation 2.6 and the parameters of the Helmholtz coil, I = 230 A, R = 0.15 m, N=10 turns, the magnetic field generated at the center of the two coils is 138 Gauss (G). The Helmholtz coil system is often used to calibrate magnetic probes for the STOR-M experiments and was also used for the internal magnetic probe arrays I designed and fabricated. The details of the internal radial magnetic probe array are described in Section 2.4.6.

2.4.6 Integrator

Integrators are important in experiments that involve magnetic field and current measurements. Integrators are used with magnetic probes and home-made Rogowski coils; these two diagnostics are presented in the Section 2.4.7 and Section 2.4.8 respectively.

Integrators can be active or passive. An active integrator comprises a resistor and a capacitor, and an Operational Amplifier (OP-AMP). A simple passive integrator consists of only a resistor and a capacitor. Either of the integrators can be used to integrate signals collected by either magnetic probes or home-made Rogowski coils. The active integrator is mostly preferred because of its time response, and it gives the more accurate integrated signal. The most critical component in an active integrator is operational amplifier (OP-AMP).

An operational amplifier (OP-AMP) is an active device which performs integration operation when a resistor is connected to its inverting or non-inverting pin, and a capacitor is connected in parallel to either its pin 2 or pin 3 and pin 6. The pin 2 and pin 3 of the OP-AMP act as virtual ground when a resistor is connected to it. The pin-out of the LM741operational amplifier used for the integrator used in this thesis is shown in Figure 2.7.

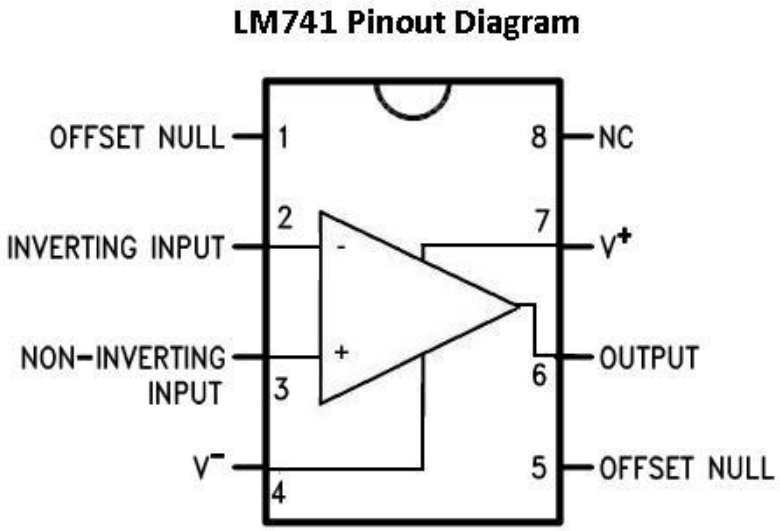

Figure 2.7: Pin-out diagram of an operational amplifier (OP-AMP). (The figure is taken from [40]).

Figure 2.8 shows the circuit diagram of an active integrator designed, assembled and optimized for the experiments reported in this thesis.

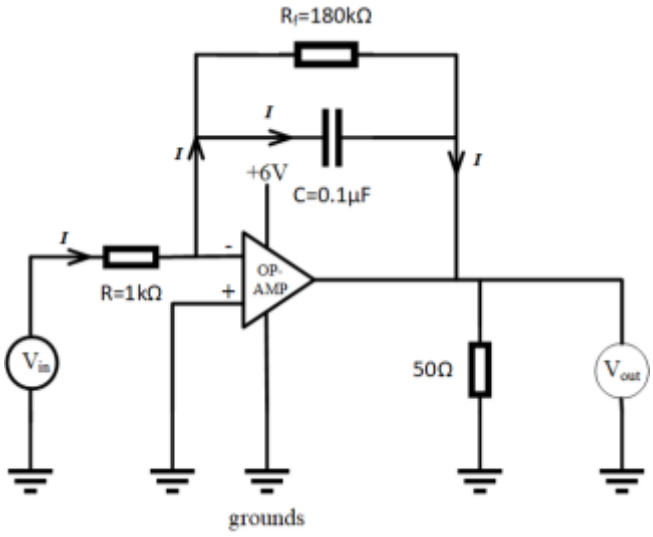

Figure 2.8: Typical active integrator circuit.

The voltage induced in magnetic probe coil or home-made Rogowski coil is inputted through the V_{in} of the integrator above, and an integrated signal is measured through the V_{out} pin. The input resistance R is 1 kΩ, and the capacitance of the capacitor connected in parallel across the OP-AMP

is 0.1 μF. A resistor with massive resistance R_f =180 kΩ is connected in parallel across the capacitor to drain the excess power in the capacitor to avoid saturation in the output signal V_{out}. The OP-AMP is equipped with a 6 V DC power source. A 50 Ω resistor is connected in parallel to the output signal of the integrator to avoid any reflection of the signal due to the high impedance of the data acquisition that was used to record the output signal. For a good approximation, the current going into the OP-AMP is very small, and the negative terminal (pin 2) is a virtual ground. Therefore, the voltage across the input resistor is equal to the input voltage to the circuit which is:

$$V_{in} = IR \tag{2.7}$$

Moreover, the voltage across the capacitor is equal to the output voltage of the circuit which is:

$$V_{out} = \frac{-1}{C}\int_0^T Idt \tag{2.8}$$

Substituting for I in Equation 2.8 using Equation 2.7, the output voltage, Equation 2.8, becomes

$$V_{out} = \frac{-1}{RC}\int_0^T V_{in}dt \tag{2.9}$$

The V_{in} is the voltage induced in the magnetic probe or home-made Rogowski coils while V_{out}. The input voltage will be explained in the next Sections, under integrator circuit and Rogowski coil.

It is seen from Equation 2.9 that the output voltage of the integrator is a function of the time constant $\tau=RC$. The resistance and the capacitance are made as small as possible to increase the sensitivity of the circuit. However, too small an integration time leads to inaccuracy of the integration. Several τ = 0.1 ms and $\tau = 0.4$ ms active integrators were made to integrate magnetic probe array and home-made Rogowski coil signal respectively.

In place of the electronic integrator, digital integration can be performed on the raw signals of the magnetic probes or the home-made Rogowski coils. Digital integration can be done using MATLAB built-in command called ‘cumsum or cumtrapz.' The integration performed by MATLAB command is mostly preferred to active integrator because no electronic noise is involved. In the thesis work, digital integration will be used for the magnetic probes signal integration.

2.4.7 Internal Radial Magnetic Probe Array

The design and calibration of internal radial magnetic probe array are necessary for this thesis to investigate the attenuation and time delay of the external radial magnetic field and the plasma responses, such as resonant magnetic perturbation (RMP), caused by the tokamak chamber walls and the plasma in the STOR-M tokamak.

The internal radial magnetic probe array is an insertable probe that can be introduced into the plasma edge to measure the radial magnetic field component in STOR-M. The insertion depth of the probe array is limited because the heat flux from the high-temperature plasma can damage the probes and perturb the plasma and change the characteristics of the plasma, which may then lead to disruption and terminate plasma discharge. That is why the probe is used to measure edge plasma properties. Despite this drawback, internal magnetic probes have proven exceedingly useful in many plasma devices including large tokamaks.

The radial internal magnetic probe array installed on the STOR-M tokamak consists of four small probes wound around Delrin plastic material. The probes are oriented to measure the plasma radial magnetic field at four different radial locations at the same time. The Delrin plastic material has a diameter and a length of 6 mm and 72.5 mm, respectively. Each probe consists of 60 turns of 32 AWG magnet wire with a winding cross section of 5×6 mm^2. The distance between two adjacent probes, center to center, is 1 cm. The innermost probe in the array, which is the probe closer to the plasma edge, is denoted P1, while the external probe is sequentially labeled P4.

The two ends of the AWG magnet wire of each probe are twisted around each other to prevent pick up of the unwanted stray magnetic field; the twisted wires are insulated from one another and are then fed through a hole at the end of the Delrin plastic. The radial magnetic probe array is inserted into an alumina ceramic tube to protect it from the hot plasma. The tube has a minor diameter of 7 mm, a thickness of 2 mm and a length of 65 mm. Figure 2.9 shows the schematic diagram of the probe array and the alumina ceramic tube.

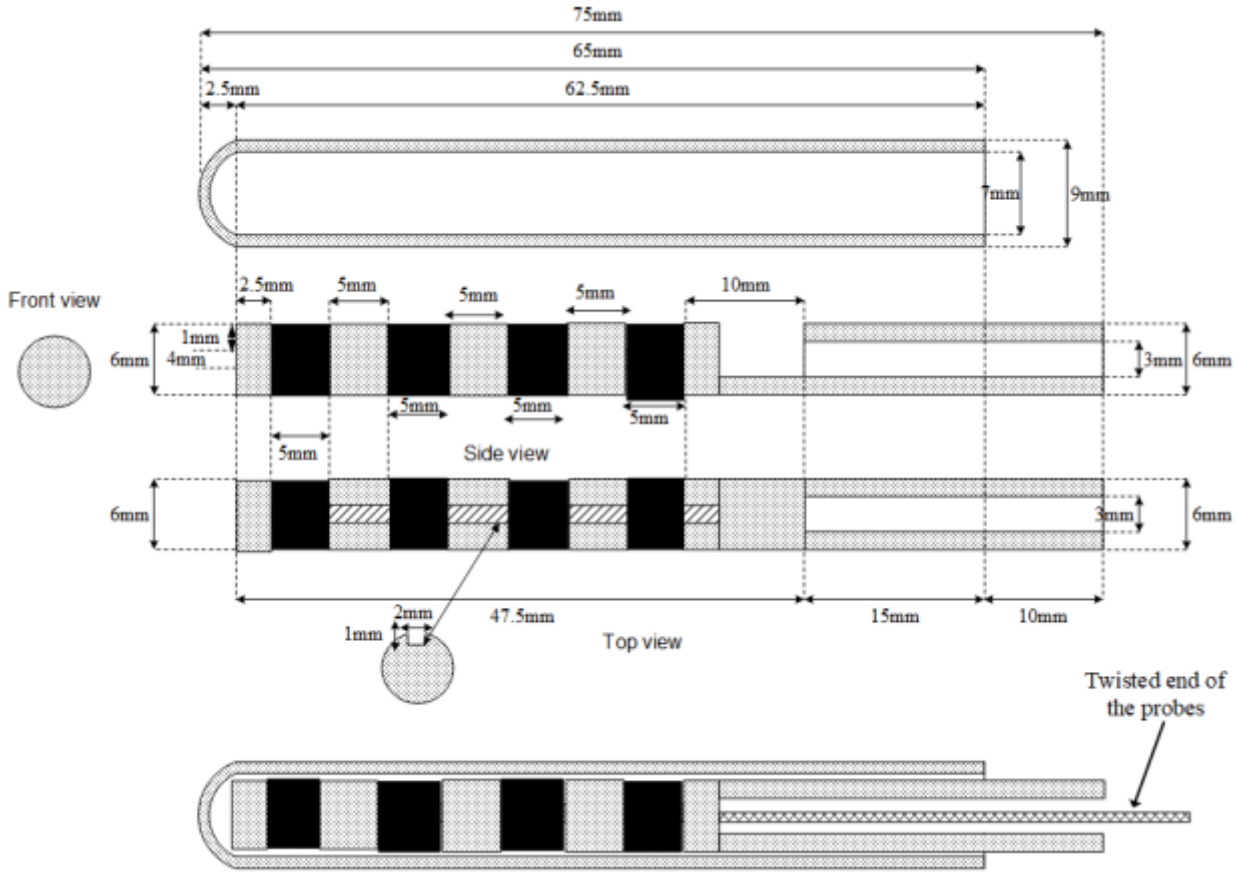

Figure 2.9: Schematic diagram of the radial internal probe array and the alumina tube.

The right-hand end of the assembly is attached to a stainless-steel rod of a rotary manipulator with Torr seal epoxy. The length of the rotary manipulator was extended by adding an extra 18cm long stainless steel hollow rod to the length of the manipulator. This extension rod can be slid in or out of the rotary manipulator to place the probe at a desired minor radial location in the STOR-M tokamak. The total length of the manipulator with the probe is 27.7 cm. The rotary manipulator consists of a circular 8-pin electrical feed-through coupled to a flange adapter by non-magnetic bolts and nuts. Each pair the of pins are soldered to the twisted end of the probe on the vacuum side and a BNC connector on the other end. A stainless-steel bellows are installed on the normal port where the probe is installed to reduce the stress caused by the vacuum chamber, and the vibration resulting from the induced force during plasma discharges. The manipulator allows us to vary the radial location of each magnetic probe. The manipulator makes it possible to scan the tokamak's minor radius from 16 cm down to around r = 8 cm. The probe can be moved outside

the chamber to a position of about r =18 cm when not in use. Figure 2.10 shows the schematic diagram of the installation of the internal magnetic probe on the STOR-M tokamak.

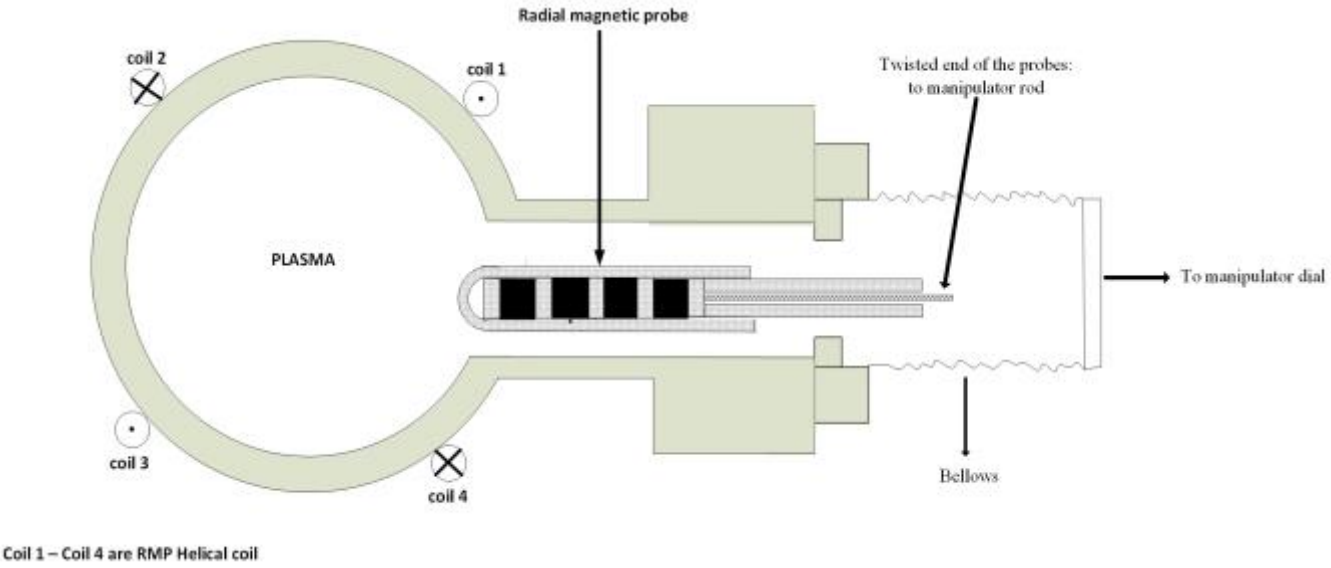

Figure 2.10: Installation of the radial magnetic probe and RMP coil on the STOR-M tokamak.

The signals picked up by the probes are transmitted across the tokamak room to the data acquisition via coaxial cables for processing. The voltage induced in the magnetic probe coil is determined by Faraday's law of electromagnetic induction [41]:

$$V_{in} = -NA\frac{dB}{dt} \tag{2.10}$$

Where N is the number of turns in the magnetic probe coil of area A. Since we are interested in the magnetic field B rather than the time derivative of B, an integrating circuit, such as the one shown in Figure 2.8, is used to obtain a magnetic field proportional to the induced voltage in magnetic coil. Performing numerical integration on the Equation 2.10, we have:

$$B = \frac{-1}{NA}\int_0^T V_{in}dt \tag{2.11}$$

moreover, by substituting Equation 2.9 into Equation 2.11, we have:

$$B = \frac{RC}{NA}V_{out} \tag{2.12}$$

where R is the resistance of the integrator, C is the capacitance, and V_{out} is the output voltage of the integrator.

The magnetic probes are calibrated against the magnetic field induced by the Helmholtz coil system discussed in Section 2.4.5. The Helmholtz coil is one of the various ways to create a known magnetic field. The voltage on the capacitor bank of the Helmholtz coil was kept constant during the calibration process, this in return produces a constant peak current and peak magnetic field. The signal picked up by the magnetic probes at the center of the coils were integrated using an analog integrator. The calibration factor of each of the magnetic probes is calculated by dividing the magnetic field of the Helmholtz coil system by the integrated magnetic probe signals. Twenty samples were collected, the average of the samples was calculated, and their error bars were determined by the standard deviation of the twenty samples. Figure 2.11 shows the magnetic field waveform of the Helmholtz coil and the uncalibrated signals of the magnetic probe array, showing different sensitivities of the probes.

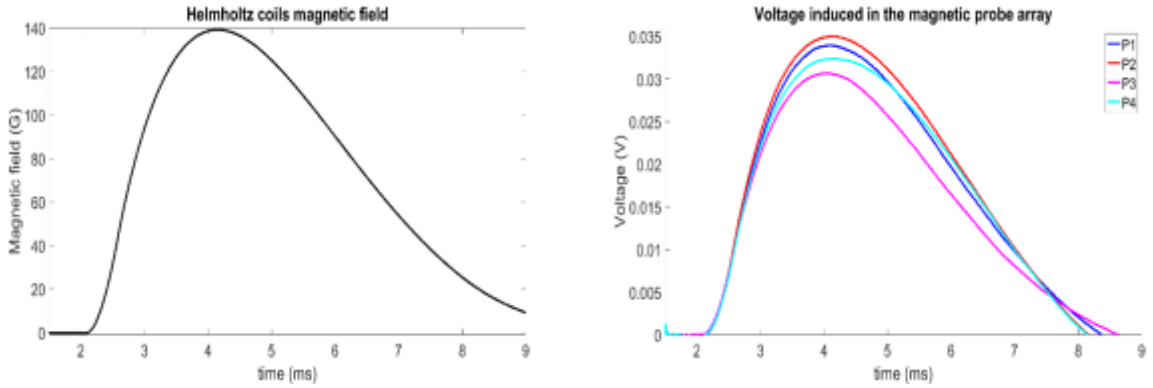

Figure 2.11: (Left) The magnetic field waveform from the Helmholtz coil. (Right) The uncalibrated signals of the internal radial magnetic probe array.

The independent calibration factors that normalize the magnetic probe signals to the magnetic field of the Helmholtz coil are listed in Table 2.3.

Table 2.3: Calibration factors of the internal magnetic probes.

Magnetic Probes	Calibration factors (G/V)
P1	$(4.11\pm0.02)\times10^3$
P2	$(4.00\pm0.02)\times10^3$
P3	$(4.51\pm0.01)\times10^3$
P4	$(4.23\pm0.03)\times10^3$

2.4.8 Rogowski Coil

Rogowski coils are used to measure the total current in the plasma and also in another diagnostic system (such as RMP system). It is a solenoidal coil whose ends are brought together to form a torus [42]. The two types of Rogowski coils that are used to measure current in the STOR-M tokamak include the commercial probe (sometimes referred as Pearson probe) with known calibration factor 100 A/V (where A is ampere and V is volt), and the home-made probe with unknown calibration factor but calibrated against the Pearson probe. The commercial Rogowski coil gets saturated when the accumulated charge carried by the current flowing through it is large due to the ferromagnetic material used in the Pearson probe. The home-made Rogowski coils use non-magnetic material and do not have the issue with the saturation. The commercial Rogowski coils have a built-in integrator, while the home-made coils do not have a built-in integrator. The active integrating circuit described in Section 2.4.6 will be used to integrate the home-made Rogowski coil signals reported in this thesis work. The schematic diagram of Rogowski coil is shown in Figure 2.12:

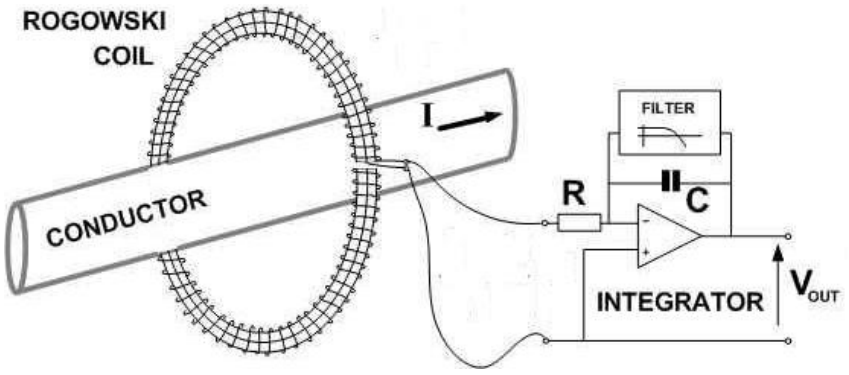

Figure 2.12: Schematic diagram of Rogowski coil with an active integrator. (The figure is taken from [43]).

The Rogowski coil illustrated in Figure 2.12 has an *N*-turn coil wound around a magnetic or non-magnetic material with a uniform cross-section area *A* and a constant turn per unit length *n* (winding density). It works on the principle of Faraday's law of electromagnetic induction. It picks up an induced voltage that is proportional to the rate of change of magnetic flux ψ that is induced by a time-varying current *I* enclosed by the Rogowski coil. The induced voltage is

$$V_{in} = -\frac{d\psi}{dt} \tag{2.13}$$

The flux linking the coil is

$$\psi = nA\mu I \tag{2.14}$$

Where μ is the permeability of the material used. Inserting Equation 2.14 into Equation 2.13 and by performing integration, the current flowing through the center of the Rogowski coil is given by

$$I = \frac{-1}{nA\mu}\int_0^T V_{in}dt \tag{2.15}$$

where *n* is the winding density, *A* is the cross-section area of the coil, V_{in} is the induced voltage, *I* is the total current flowing through the center of the Rogowski coil. For direct current measurement, an analog or digital integrator is required. The signals of the home-made Rogowski coil are integrated by active integrators (discussed in Section 2.4.6) with a time constant of 0.4 ms. If we substitute Equation 2.9 in Section 2.4.6 into Equation 2.15, we have, where V_{out} is the output voltage from the integrator described in Section 2.4.6, the required current *I* measure through the through the home-made Rogowski coil:

$$I = \frac{RC}{nA\mu}V_{out} \tag{2.16}$$

The calibration of the home-made Rogowski coils against the commercial Rogowski coils (Pearson probe) was carried out before installing them on the STOR-M tokamak using the Fast Resonant Magnetic Perturbation (FRMP) current. The FRMP system and its current waveform will be discussed in the next Section.

2.4.9 Resonant Magnetic Perturbations (RMPs) Systems

Resonant magnetic perturbation has been used widely in the magnetic fusion research community to influence the tokamak plasmas with radial magnetic fields to suppress magnetohydrodynamic (MHD) instabilities. The coils that produce these fields are sometimes located outside the vacuum chamber in the smaller tokamaks and inside the vacuum vessel in larger tokamaks. It was first demonstrated in Pulsator tokamak that RMP helps to suppress and control magnetohydrodynamic (MHD) instabilities [44]. MHD suppression has been demonstrated in COMPASS-C tokamak

device [45] using RMP. It is also worth knowing that major disruption could be initiated by an externally applied RMP field as it was demonstrated in Tokoloshe tokamak [46]. Moreover, in an improved confinement mode (H-mode) operation, tokamaks are subjected to another type of instabilities called type-1 edge-localized modes (ELMs) instability. RMP has also been shown to help mitigate this type-1 ELMs instability in DIII-D tokamak [47]. Also, RMP will be one of the techniques to mitigate and control ELMs in ITER [48].

The RMP systems installed on the STOR-M was used to suppress the activities of magnetohydrodynamic (MHD) instabilities. The discussion and the results of the suppression of the MHD activities are reported previously in [11, 37]. The RMP systems installed on the STOR-M tokamak are made up of RMP coil itself, the Slow Resonant Magnetic Perturbations (SRMP) circuit, and Fast Resonant Magnetic Perturbations (FRMP) circuit.

2.4.9.1 RMP coil

The RMP coil, which is made from 30 meters long 8 AWG wire, is externally helically wounded around the STOR-M tokamak chamber at a radius r = 16.4 cm as schematically shown in Figure 2.13. The red and the blue wires carry equal current but in the opposite direction. One blue wire and one red wire are separated from each other poloidally by an angle of 90°. Two sets of helical windings connected in series were made from the wire so that the helicity configuration would be m = 2, n = 1 (where m and n are poloidal and toroidal mode number respectively). The purpose of using two sets of helical windings with a reverse current polarity is to prevent coupling between the RMP coils and the ohmic heating coils. By using two sets of windings with opposite polarities minimizes the transformer effect of other coils on the RMP windings [11].

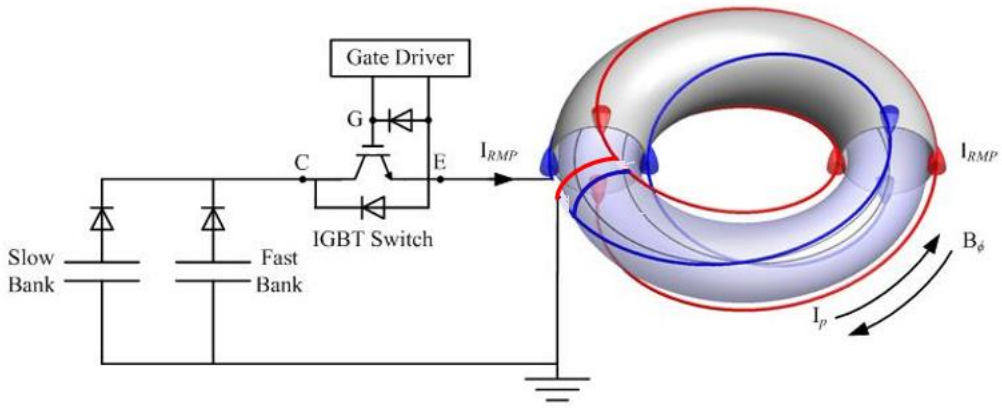

Figure 2.13: Layout of RMP coil in STOR-M tokamak. (The figure is taken from [11]).

2.4.9.2 Slow Resonant Magnetic Perturbation (SRMP)

The SRMP system is used to generate a long pulse magnetic field to suppress MHD activities in the STOR-M tokamak plasma. The SRMP circuit consists of two capacitor banks, Insulated-gate bipolar transistor (IGBT) switch, and trigger circuits. The current is driven through the helical coil described in Figure 2.13 by two capacitor banks; the first bank (50 mF, 450 V) is used to achieve current fast ramp-up and the second bank (420 mF, 100 V) is used to maintain the current flat top. The SRMP capacitor banks are usually fired 15ms after the OH capacitor bank. The current driven through the helical coil is gated (gate width varies from 1-26 ms) by an IGBT switch, and the gated current is monitored by a home-made Rogowski coil. The time duration of the current during an RMP experiment is 8 ms. During this period, suppression of Mirnov (MHD) activities was observed [11]. A current of about 0.93 kA can be driven at a voltage of 100 V on the first capacitor bank and 90 V on the second capacitor bank. A typical SRMP current waveform is shown in Figure 2.14.

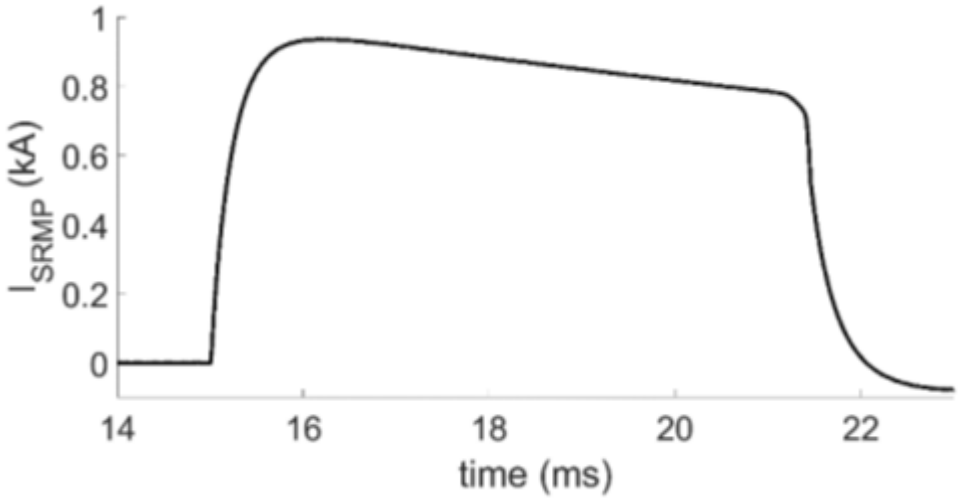

Figure 2.14: Typical SRMP current waveform.

2.4.9.3 Fast Resonant Magnetic Perturbations (FRMPs)

The FRMP system is used to study the shielding effect of plasma on the external magnetic fields such as RMP field. The FRMP current is also driven through the same helical coil in Figure 2.13 above. The FRMP circuit consists of a capacitor bank (2.5 mF, 450 V), Silicon-Controlled Rectifier (SCR) switch and a trigger circuit. The FRMP capacitor bank is fired 3ms after the SRMP capacitor banks, and the current is discharged through the SCR switch. The FRMP current is also is monitored by a home-made Rogowski coil. A current between the range of 0.89-2.5 kA can be driven if the capacitor bank is charged to 400 V. A typical FRMP current waveform is shown in Figure 2.15. It lasts less than 1 ms.

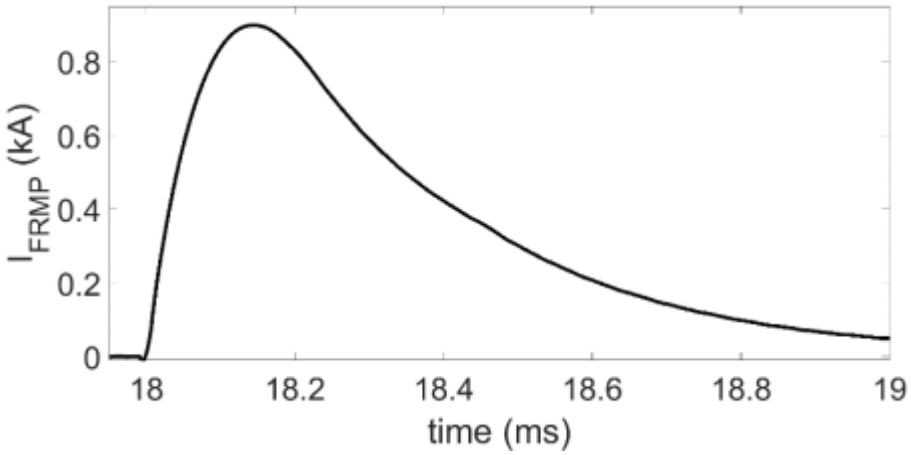

Figure 2.15: Typical FRMP current waveform.

Chapter 3

Effects of Lithium Coating on the Impurities in the STOR-M Tokamak

3.1 Introduction

In this chapter, the effects of lithium coating on the impurities in the STOR-M tokamak was studied with intensified charge-coupled device (ICCD) camera systems, and the results of the study were also reported. Effects of the base pressures on the impurities were also investigated before and after freshly coated lithium. Since lithium was introduced into the tokamak, it is important to determine the lifespan of the coated lithium. The effective lifetime of lithium was determined by continuously running plasma discharge with lithium and then measuring the lithium intensity with the Czerny-Turner Spectrometer after 300, 600 and 900 plasma discharge shots. The measurement of lithium intensity, impurity intensity, and plasma density after several plasma discharge shots provided information to determine the number of discharge after which lithium coating effects will diminish and recoating becomes necessary.

The ICCD camera system used to study the effect of lithium coating, consists of collimators, an optical fiber bundle, an imaging spectrometer, and a PIMAX-3 ICCD camera. The working principle and the features of the PIMAX-3 ICCD camera, calibration, and alignment of imaging spectrometer will be explained in this Chapter. The major impurities monitored during the lithium coating experiment are presented, a method of data analysis employed during the lithium coating experiment will be explained, and finally, the results of the lithium coating will be reported.

3.2 PIMAX-3 Intensified Charge Coupled Device (ICCD) camera

PIMAX-3 ICCD camera is the latest diagnostics system that has just been added to the diagnostics suite on the STOR-M tokamak. This device works on the principle of the photoelectric effect. The ICCD camera is made up of two separate components coupled to one device; the intensifier, which is responsible for converting light into electrons, multiplying the electrons and reconverting the electrons back into the light for the CCD to detect. The CCD converts the intensified light into electron charges. The camera is designed for general macro-imaging and microscopy imaging applications. It uses closeness-focused micro-channel plate (MCP) Gen III filmless image

intensifier fiber-optically coupled to a charge-coupled device array [49]. The camera has a pixel resolution of 1024 pixels by 1024 pixels. The ICCD camera relies on either internal or external trigger for exposure to light. For the experiment reported in this thesis, the camera receives a trigger from a computer generated pulse. This computer generated pulse also controls the discharge of the STOR-M tokamak plasma. The gate delay and the gate width of the camera range from 3×10^{-5} to 2×10^{4} ms.

In operation, data acquired by the ICCD camera is routed to the computer for processing and display. The computer controls both the system configuration and data acquisition via Lightfield software installed on a Windows 10 operating system computer. After the data is converted, it is transferred directly from the camera to the host computer via the high-speed interface cable [49]. The amount of dark charge is reduced by cooling the CCD array using the built-in air-cooling system; this also improves the signal-to-noise ratio. Throughout the experimental time for the experiment reported in this thesis, the sensor temperature was controlled at -29 ℃.

The major components of the ICCD are input windows, photocathode, Microchannel Plate (MCP), phosphor, fiber-optic bundle and CCD array. Figure 3.1 shows the major components of the intensified charge coupled device.

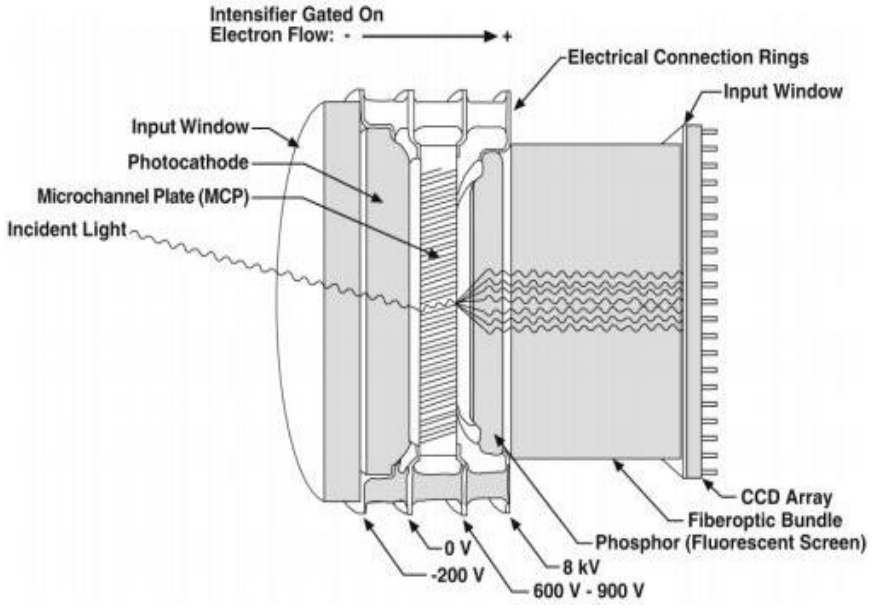

Figure 3.1: Major components of the ICCD. (The figure is taken from [49]).

The ICCD camera is mounted to an imaging spectrometer on an optical bench to record the spectrum of light inputted into the spectrometer as shown in Figure 3.2. The camera is often triggered at 15ms during plasma current plateau to record plasma light for 1ms.

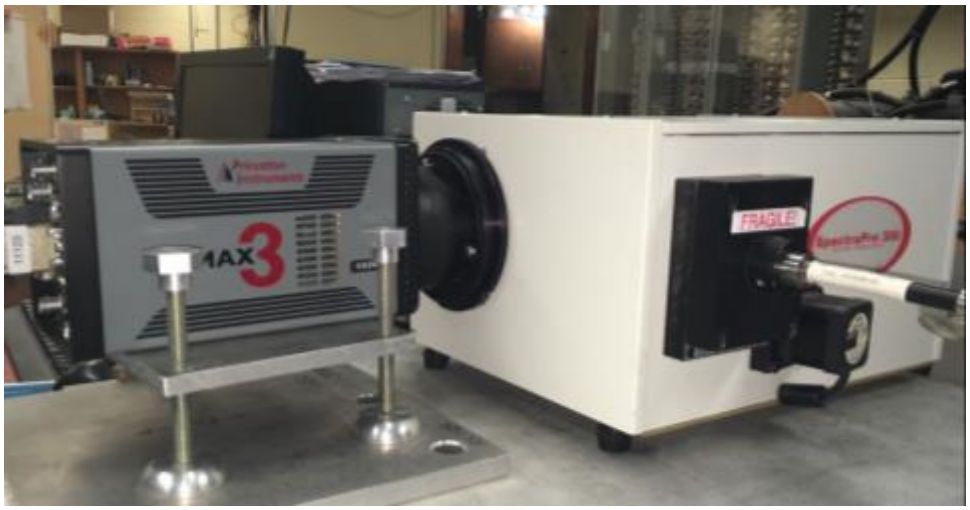

Figure 3.2: ICCD camera mounted to an imaging spectrometer.

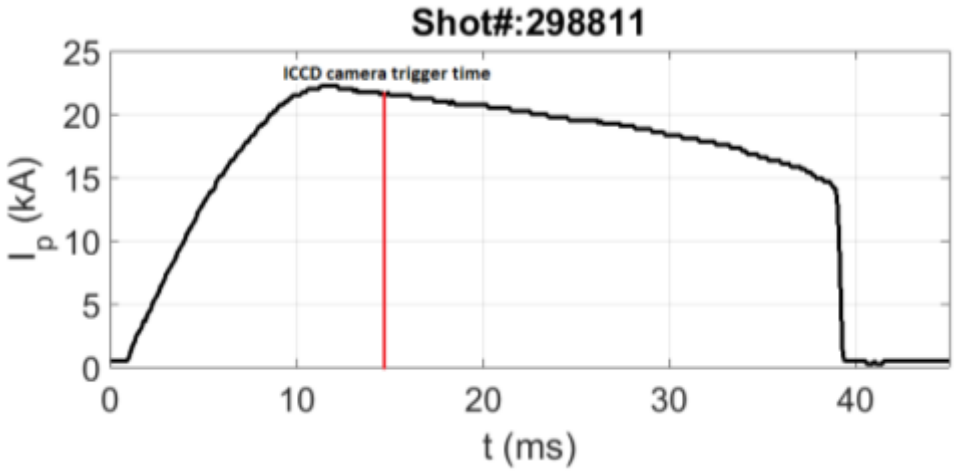

Figure 3.3: Typical plasma current showing the time when ICCD camera was triggered.

3.3 The SpectraPro-300i Imaging Spectrometer

An imaging spectrometer is an instrument that is used to capture the spectral content of light. The imaging spectrometer consists of four mirrors use to focus light to and from the diffraction grating. The SpectraPro-300i imaging spectrometer used during this project is a 300 mm focal length

spectrometer, which has a linear dispersion of 2.7 nm/mm, with an aperture ratio of f/4 and a triple grating turret of 600 grooves/mm at 300 nm blaze wavelength, 1200 grooves/mm at 300 nm blaze wavelength, and 1200 grooves/mm at 500 nm blaze wavelength. The desirable grating is selected through the Lightfield software of the ICCD camera discussed above. The Lightfield software was designed to accommodate any compatible spectrometer software. To improve the spectrometer diffraction efficiency for the selected spectral lines to be measured from STOR-M, 1200 grooves/mm at 500 nm blaze wavelength has been chosen for the experiment reported in this thesis work. The spectrometer has a dual exit port; front and side port. Port selection is made through the computer that controls the system. The ICCD camera discussed in Section 3.2 was attached to the ICCD port (shown in Figure 3.4) of the spectrometer using the spectrometer's factory built-in flanges. The ICCD port has a focal plane that extends 25 mm outside the spectrometer housing. Moreover, when a particular wavelength is entered into the center wavelength of the spectrometer, the spectrum of light corresponding to the wavelength appears at the center region of the ICCD camera sensor. The schematic diagram of the imaging spectrometer is shown in Figure 3.4.

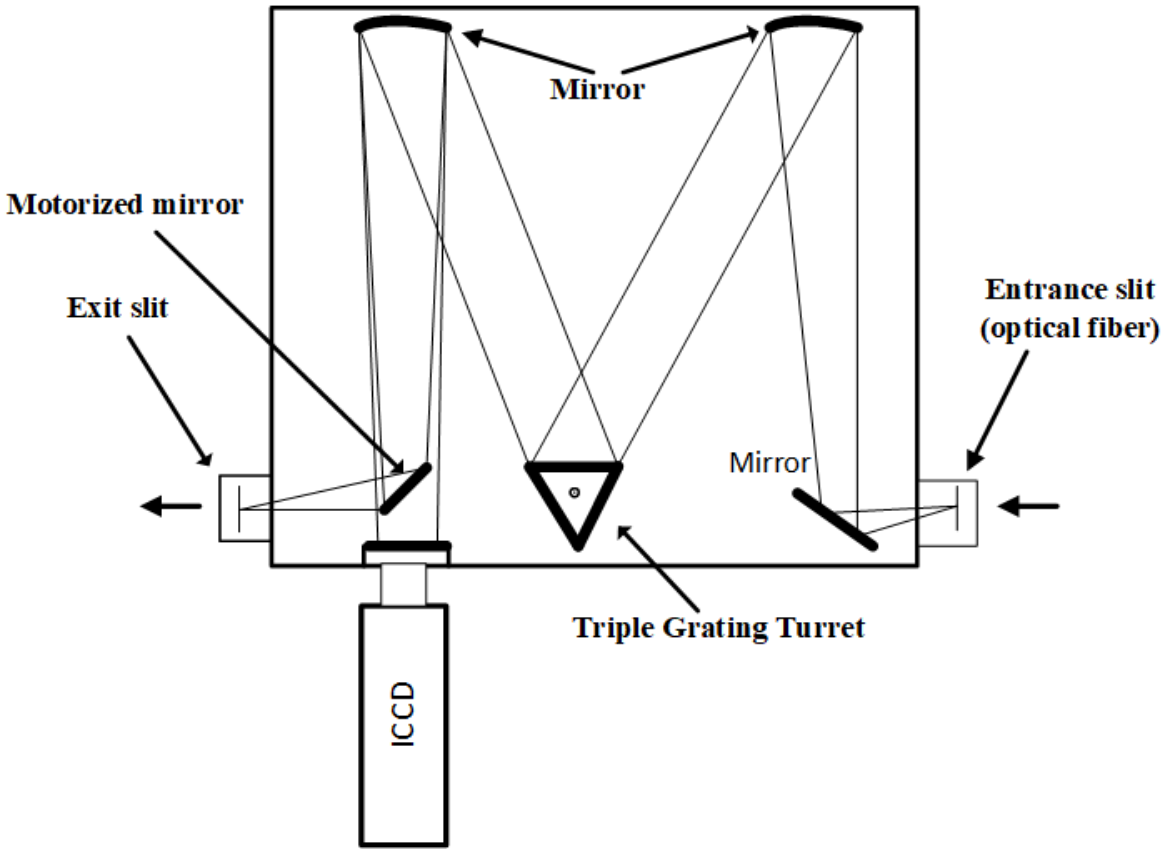

Figure 3.4: Schematic diagram of an imaging spectrometer.

3.4 Optical Fiber Bundle

An optical fiber is used to transmit light from one point to another. A 3-meter-long optical fiber bundle consisting of 12 fibers was used to convey plasma light from the STOR-M tokamak's oval port (the oval port is described in Section 3.5.) to the imaging spectrometer described in Section 3.3. Each one of 12 separate fibers consists of three fibers (25 microns in diameter) and is connected to an optical collimator on one end, and the other ends are arranged to form a narrow entrance slit for the imaging spectrometer. The end view of the entrance slit is shown in Figure 3.5.

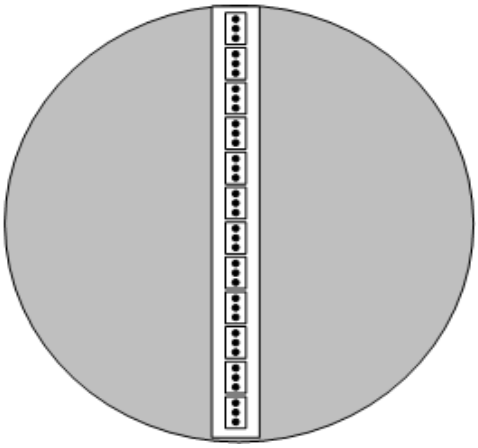

Figure 3.5: End view of the entrance slit.

Meanwhile, only eight channels out of the twelve bundles were fit into the sensor of the ICCD camera; the other four channels are out of the camera view. The collimators, which is the receiving lens of the fiber optic bundle, are used to focus light from the observation oval port of the STOR-M tokamak to the imaging spectrometer's diffraction grating through the optical fiber bundle. The collimator lens that converges acquired light is housed in a black plastic holder with a dimension ××of 2.5 cm×2.1 cm×6.3 cm. Before installing the collimators to the observation port, a spectral lamp was used to shine light onto the input slit of the optical fiber bundle, and the output light was focused to a distance of 39 cm through the collimator. This is because the collimators will collect light at 39 cm from the center of the vacuum chamber. The eight fiber cables used are labeled 'fiber *A*' to 'fiber *H*.'

3.5 The STOR-M Tokamak's Oval Port

The oval port is about 39 cm long (vertically) from the center of the vacuum chamber, the port is divided into eight lines of sight by attaching to the port an evenly spaced collimator holder made from Delrin material. The labeling and the corresponding minor radial location of each port are shown in Table 3.1. The distance between two neighboring lines of sight is 2.6 cm. The collimators were arranged in an array to capture plasma emission at different plasma radius. Figure 3.6 shows the sight of view of the optical fiber bundles. The oval port is offset relative to the tokamak chamber center. That is shifted toward the outer edge of the chamber.

Table 3.1: Labelling and corresponding minor radius of the divided oval port.

Ports	**P1**	**P2**	**P3**	**P4**	**P5**	**P6**	**P7**	**P8**
Radius (cm)	-5.2	-2.6	0	2.6	5.2	7.8	10.4	13.0

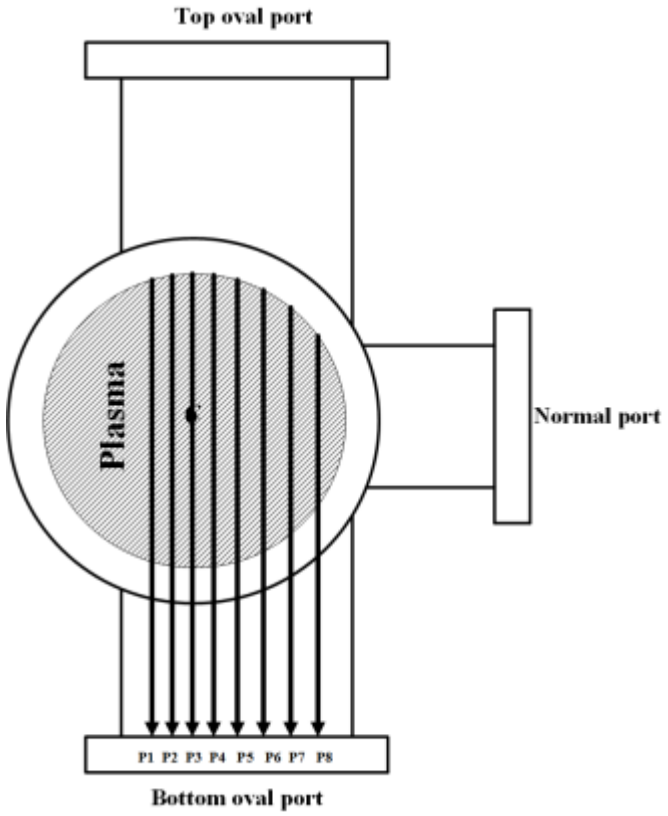

Figure 3.6: Schematic diagram of the optical fiber bundle line of view. (Where the center of the chamber is denoted with solid black dot)

3.6 Mercury-Neon Spectral Lamp

The mercury-neon lamp (Oriel Model no: 6034) is one of the spectral lamps that is widely used for alignment and calibration of optical instruments, such as spectrometer and detector in spectroscopy experiments. A mercury-neon spectral lamp is temperature sensitive. Under normal temperature, the output is dominated by mercury lines. The lamp can also be cooled through forced air to produce neon lines [50]. Since mercury lines do not need to be forced air cool to produce them, the mercury lines were used for intensity and wavelength calibration of the ICCD camera system. The lamp can produce mercury lines with different intensity at different wavelength. The mercury line with the brightest intensity has a wavelength of 435.8 nm. This line was selected and used for the intensity calibration and center wavelength calibration of the ICCD camera and the imaging spectrometer. The results of the alignment and the calibration are reported in Section 3.7.

3.7 Relative Intensity Calibration

The mercury-neon spectral lamp described above in Section 3.6 was used for relative sensitivity calibration and center wavelength verification. To ensure that the spectrum of the impurity line that is being examined truly appears at the center region of the ICCD detector, a center wavelength verification was required. This was performed on the imaging spectrometer and the ICCD detector using the mercury-neon spectral lamp as the light source. This process was done in a dark room to ensure that the light from the spectral lamp was not contaminated by the background light. The center wavelength of the imaging spectrometer was set to 453.8 nm, the wavelength of the mercury line with the brightest intensity. The collimators of the fiber bundles were arranged in a semi-circle, and the spectral lamp was positioned at the center of the semi-circle so that all the collimators collect an equal amount of light if the emission from the spectral lamp is isotropic. Although this assumption may not be accurate because of the non-uniformity of the glass tube of the lamp. Light collected through the collimator was dispersed by the spectrometer, and the spectrum of mercury line was recorded at the center region of the ICCD detector. Only eight channels of the twelve fiber cables appeared on the computer screen, the last four channels (from the bottom of the slit) are out of the view of the ICCD camera as mentioned earlier. The spectrum images of all eight fiber channels captured by the camera appear vertically on the computer screen with ‘fiber *A*’ at the top and ‘fiber *H*’ at the bottom of the ICCD detector as shown in Figure 3.7. In the top sub-panel, the vertical axis is the pixel intensity, and the horizontal axis is the

wavelength. Based on the diffraction grating selected and the wavelength entered for the imaging spectrometer, Lightfield software converted the pixels' number automatically into wavelength.

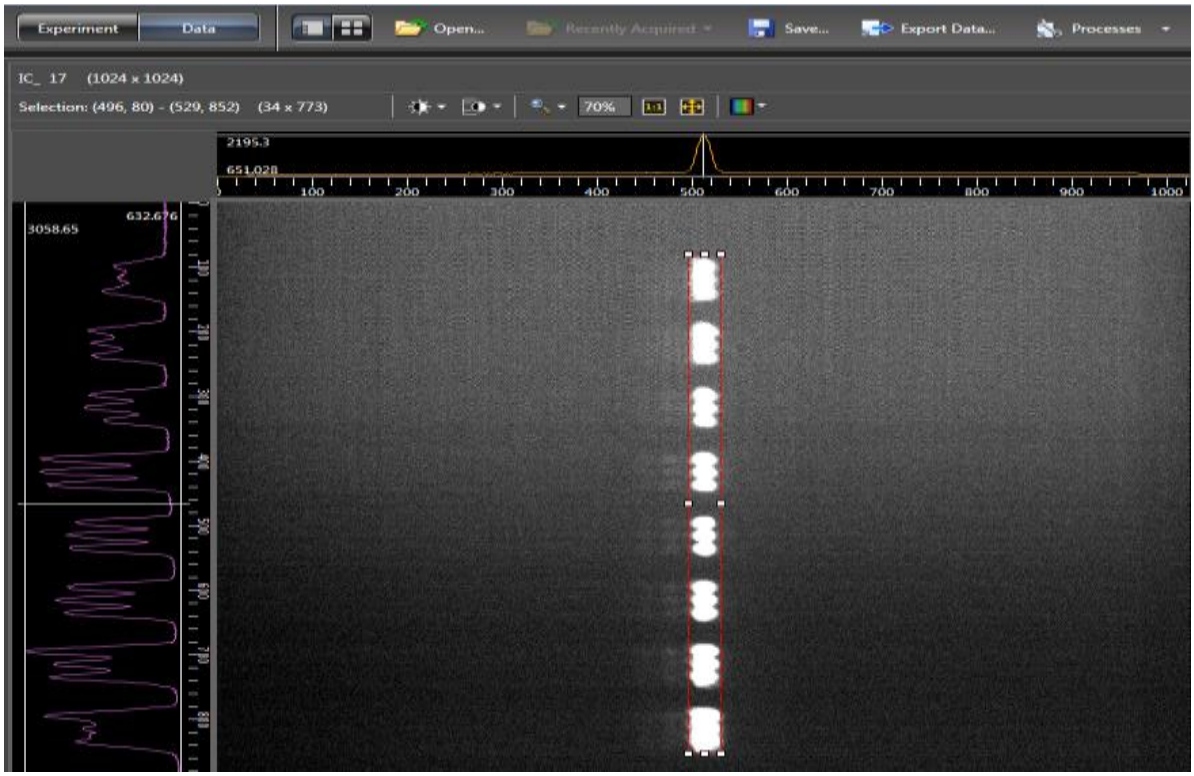

Figure 3.7: Spectrum of Mercury - Neon spectral lamp. The horizontal axis is pixels' number.

The image in Figure 3.7 is the spectrum of mercury-neon line with a wavelength of 435.8 nm as captured by the eight channels of the fiber bundle. A channel, say 'fiber *A*,' composed of 3 dots corresponding to the image of one fiber from the optical fiber bundle. Two adjacent fibers say from the top of 'fiber *A*' to the upper part of 'fiber *B*,' are separated by 100 pixels on the ICCD image. For example, if coordinates of 'fiber *A*' are X=496, Y=80, the next fiber to 'fiber *A*' which is 'fiber *B*' will have X=496, Y=180, etc. All the useful data of all channels are contained within the same numbers of pixel width and height in the image for further data analyses. The spectrum of the light, which is 1024 by 1024 pixels, was exported into an Excel file (.csv) and was processed by a customized MATLAB script. The MATLAB program extracts the region to be processed based on X-coordinate, Y-coordinate, the width, and the height of the pixels inputted to the program. From Figure 3.7 above, the values that correspond to the region highlighted are specified by pixel number coordinate of the left lower corner at (X=496, Y=80), and the range of width=34 (wavelength) and height=773 (for all 8 fiber channels). There are 70 pixels in height for each

channel and they were integrated vertically to get a total of 34 integrated intensity pixels for that channel. These 34 integrated pixels correspond to 34 different wavelengths as dispersed horizontally by the imaging spectrometer based on diffraction grating and the center wavelength inputted for the spectrometer. The integrated intensity is plotted against the corresponding wavelengths to determine the wavelength with the highest intensity. This wavelength corresponds to the wavelength of the mercury line that was entered into the center wavelength of the spectrometer. The plot of the intensity distribution is shown in Figure 3.8 for the integrated images in Figure 3.7.

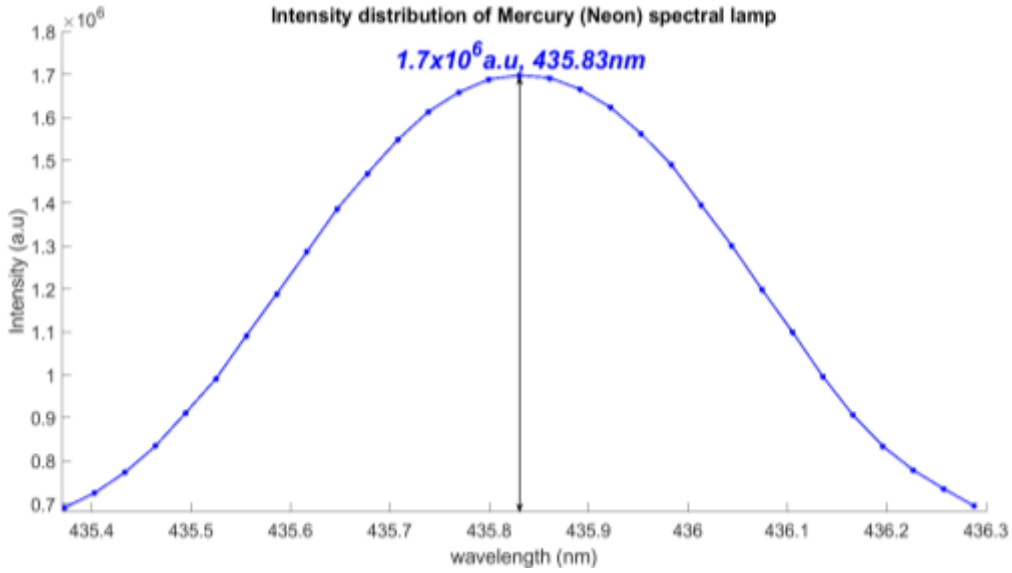

Figure 3.8: Intensity distribution of Mercury-Neon spectral lamp.

From the plot above, the highest integrated intensity, 1.7×10^6 a. u was observed at 435.83 nm; this is approximately equal to the center wavelength that the grating of the spectrometer was set to initially. In conclusion, this confirmed that when the spectrometer's grating is set to the wavelength of a targeted impurity line, the spectrum of the impurity line appears at the center region of the ICCD camera.

The relative sensitivity calibration is necessary to compensate for the different sensitivities of the eight channels of the fiber bundle. The grating of the spectrometer was set to the wavelength of the mercury line with the brightest intensity, 435.8 nm. A fiber channel was used at a time to collect the spectral lamp's light, and the spectrum of the light as dispersed by the spectrometer was recorded by the ICCD camera. This process was also done in a dark room to eliminate background

light. The position of the lamp was fixed as well as the location of the fiber cables. Measurement is done one channel at the time by setting the collimators at the same location with respect to the spectral lamp. The current to the lamp was kept constant throughout the calibration process. The pixel area of each fiber channel is 34 pixels × 70 pixels. The whole pixels, which corresponds to the full sensor of the camera, was exported into an Excel file (.csv), and the pixel area needed for the intensity evaluation were extracted based on the X-coordinate, Y-coordinate, width and height values of the fiber location. The data was processed by a customized MATLAB program written to integrate the intensity of the pixels vertically and horizontally to produce a single intensity value from the pixel area of a particular fiber channel. The integrated intensity was calculated for all the fiber channels, and the third channel, labeled 'fiber *C*' recorded the brightest intensity. The intensity of all other fibers was then normalized to the intensity of 'fiber *C*' by dividing the intensity of 'fiber *C*' by intensity of other fibers to get normalization factor for all the channels. The relative normalization factors of the fibers cables are listed in Table 3.2. The normalization factors were used to multiply the intensity of the fiber channel during data analysis.

Table 3.2: Relative calibration factors of the optical fiber bundle.

Fibers (Channel)	**A**	**B**	**C**	**D**	**E**	**F**	**G**	**H**
Normalization factors	2.24	1.39	1.00	1.69	2.17	2.50	2.26	2.51

3.8 Major Impurities in the STOR-M Tokamak

In the previous spectroscopy experiments conducted on the STOR-M tokamak, impurities from carbon and oxygen have been identified [51]. The type of impurity line observe in any tokamak depends on wall material of the tokamak as discussed in Chapter 1. Impurities can be enhanced in any tokamak by injecting impurity gasses such as methane, helium, and argon into the chamber of tokamaks [10]. Carbon and oxygen emission lines are observed without the introduction of impurity gasses in the STOR-M tokamak. These emission lines have been used in the previous experiment conducted on the STOR-M tokamak to measure the toroidal flow velocity of plasma [10]. Table 3.3 shows the emission lines, the electronic transitions, wavelengths and radial location where the highest intensity of the emission is recorded in the STOR-M tokamak.

Table 3.3: Location of the peak intensity of selected impurity emission lines in the STOR-M tokamak with their transition [52-53].

Emission lines	Electronic transitions	Wavelengths (nm)	Radial location of peak intensity (cm)	References
CIII	$1s^2 2s3s - 1s^2 2s3\text{p}$	464.74	r = 7	[52]
OV	$3p^3D_3 - 3d^3F_4$	650.02	r = 3	[52]
CVI	n=8 – n=7	529.05	r = 0	[53]

3.9 Experimental Data Analysis

One of the features of an imaging spectrometer is its ability to perform the spatially resolved measurement. To show the global intensity of the impurities in Table 3.3 measured by the optical fiber bundle at eight different minor radial locations presented in Table 3.1, during plasma discharge, the intensity of each impurity lines measured by eight channels are summed up for some of the presentations in this thesis. The measurements are performed before and after lithium passivation. The summed intensity was used to compare the percentage change in the total intensity of the impurities. Five (5) samples were collected for each of the impurity lines in some experiment, while two (2) samples were collected for some, the mean and the standard deviation were calculated for the samples. The average intensity with the corresponding error is plotted against the minor radius to give intensity profile for each of the lines.

3.10 Plasma Parameters in the STOR-M Tokamak During Normal Discharge

During normal discharge with lithium coating, the plasma produced in the STOR-M tokamak has the following parameters as plotted in Figure 3.9 for shot #308317. Plasma current I_p is approximately 19 kA, loop voltage V_l is around 3.5 V, line-averaged density n_e is approximately 9.5×10^{12} cm^{-3}, and plasma position is approximately around the magnetic field center. The plasma discharges with similar parameters as plotted in Figure 3.9 were used for the lithium coating experiment.

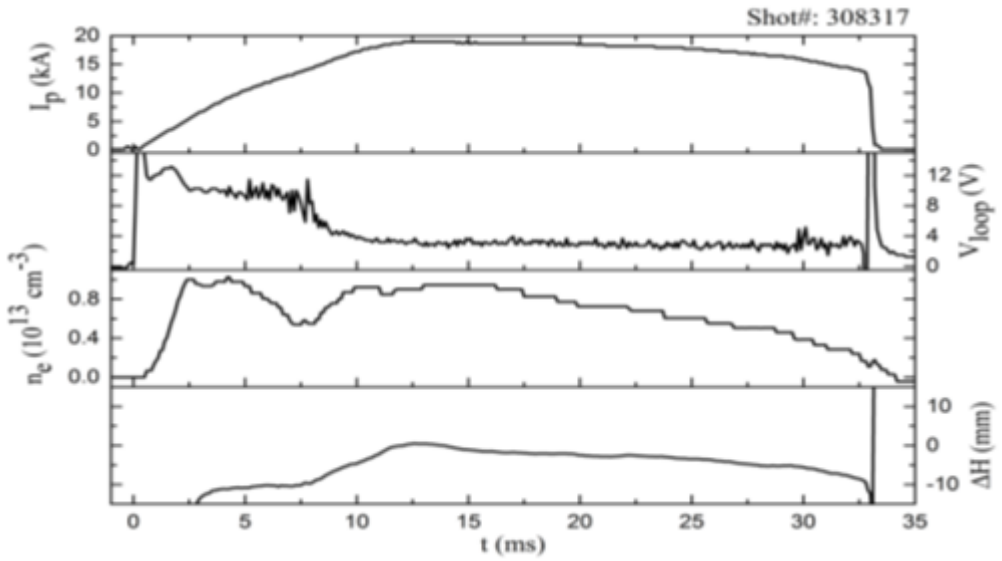

Figure 3.9: Plasma parameters during normal discharge.

3.11 Effects of Lithium Coating on the Impurities

The effect of lithium coating on CIII, CVI and OV intensities was investigated during the stable period of plasma discharge. The plasma discharges during the experiment have similar features as the plot in Figure 3.9. The base pressure during the plasma discharge, with and without lithium, is 0.8×10^{-4} Torr, this is the pressure at which hydrogen gas is constantly fed into the tokamak chamber. Since the spectral lines of the impurities are separated in a wide wavelength range, it was only possible to record the intensity of one impurity line at a time during each plasma discharge. The intensity of an impurity line was captured one after the other. The intensity of the impurities was recorded twice during plasma discharge with similar features, with and without lithium. The average and the standard deviation of the intensities in each case were calculated, and these values were plotted against the STOR-M tokamak minor radius. The minor radius considered is $-5.2\ \text{cm} \leq r \leq 13.0\ \text{cm}$, the optical fibers that captured the plasma light were arranged horizontally at these radii, with innermost fiber located at r = -5.2 cm and outermost located at r = 13.0cm. Although two samples are not enough to estimate standard deviation, it was done anyway so that coated lithium will not lose potency if several samples were recorded. The distance between two neighboring fibers is 2.6 cm. The center wavelength of the spectrometer was set to the wavelength of the emission line to be considered, the ICCD camera was triggered externally through a computer-generated pulse, and the impurity spectrum was recorded only for one

millisecond (1 ms). The intensifier gain of the ICCD camera was set to 50. Figure 3.10 – Figure 3.12 shows the plots of the intensity of the impurity lines versus minor radius before and after lithium coating. The red plot corresponds to the intensity of the impurity line before the lithium coating, and the blue plot is the intensity of the impurity lines after lithium coating. The profiles do not seem to be symmetric, and the exact reasons for it are still under investigation. The plots show that there is a significant reduction in the emission of CIII, CVI, and OV lines after the inner wall surfaces of the STOR-M tokamak was coated with lithium. The result is similar to the results reported in NSTX device [21] and Aditya tokamak [22]. However, oxygen emission was more reduced compared to carbon emission after freshly coated lithium. The results from STOR-M confirms that lithium coating effectively reduces the impurities in the plasma.

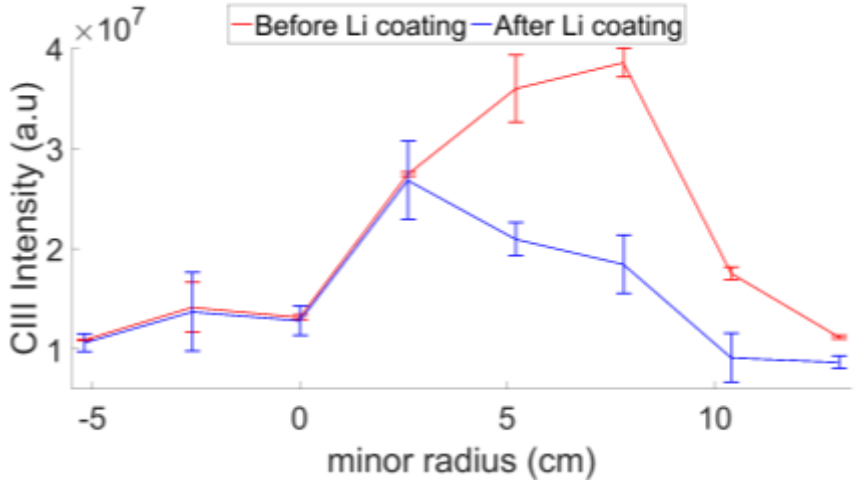

Figure 3.10: Intensity profile of CIII before and after lithium coating.

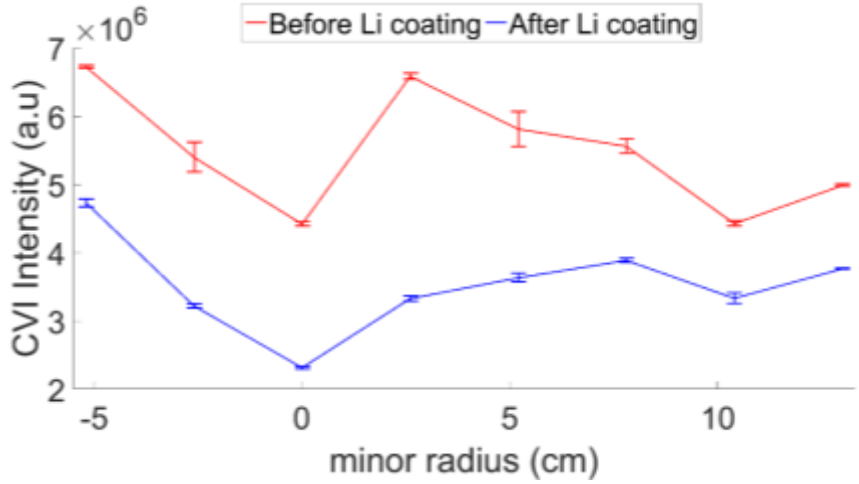

Figure 3.11: Intensity profile of CVI before and after lithium coating.

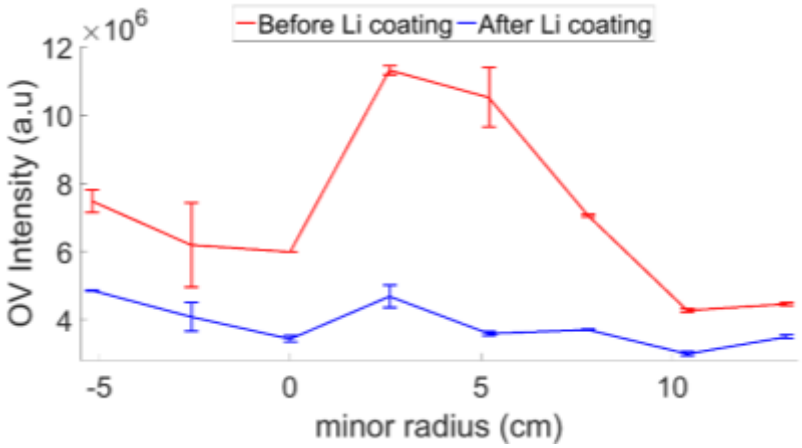

Figure 3.12: Intensity profile of OV before and after lithium coating.

Table 3.4 lists the intensities before and after the lithium coating in the STOR-M tokamak. The intensities were calculated by summing up the intensities of eight lines of sight. The last column shows how much the intensity of each of the impurity lines was suppressed by the coated lithium.

Table 3.4: Quantitative intensity before and after lithium coating.

Impurity lines	**Integrated intensity before Li coating (a.u)**	**Integrated intensity after Li coating (a.u)**	**Percentage decrease**
CIII	1.69×10^8	1.21×10^8	28%
CVI	4.39×10^7	2.82×10^7	36%
OV	5.73×10^7	3.08×10^7	46%

From Table 3.4 above, 28% of CIII (464.74 nm) intensity, 36% of CVI (529.05 nm) intensity and 46% of OV (650.02 nm) intensity were reduced after the lithium coating. The results show that oxygen emission was greatly suppressed compare to carbon emissions as it can also be seen in Figure 3.10 – 3.12.

In a subsequent experiment conducted on the STOR-M tokamak after the freshly coated lithium, it was observed that when the base pressure, the pressure at which hydrogen gas is puffed into the chamber, was increased, the intensities of all the impurity lines were increased linearly. Although the similar result was observed in the impurities without lithium, a clear increase in the intensities as the base pressure was increased was observed after the lithiumization of the chamber. It is worth

noting that a good plasma discharge could not be achieved without lithium at a base pressure of 1.6×10^{-4} Torr, because the density was too high and it was difficult to control plasma, but a good plasma discharge was possible with lithium at that same pressure due to reduced recycling of gas from the chamber wall after lithium coating leading to a decrease in a plasma density. Because we are only interested in the behavior of the impurities and the plasma density as the base pressure is varied, the following base pressures were considered without lithium; 0.6×10^{-4} Torr, 0.8×10^{-4} Torr, and 1.2×10^{-4} Torr. The base pressure at which the intensities and the plasma density were measured with lithium are 0.8×10^{-4} Torr, 1.2×10^{-4} Torr, and 1.6×10^{-4} Torr. Increasing the base pressure does not directly increase the intensity of the impurities. Increasing the base pressure increases the puffed hydrogen gas, and then increase plasma density. It is the interaction of plasma with the walls of the vacuum vessel that liberates impurities. Figure 3.13 shows the plot of the density against the base pressure before and after lithium coating. The red plot is the plasma density before lithium coating, and the blue plot is the plasma density after lithium coating. It can be clearly concluded that lithium coating significantly reduces the recycling and reduce the plasma density under the same base pressure.

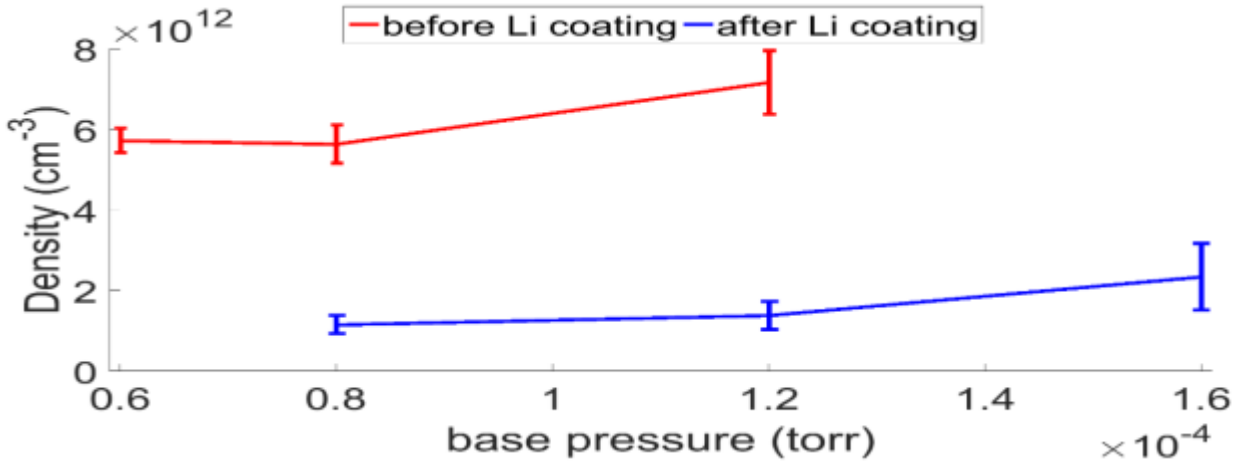

Figure 3.13: Plasma density vs. base pressure before and after lithium.

As it is seen in Figure 3.13 above, the plasma density steadily increases as the base pressure is increased in each case with and without lithium coating. It can also be seen that the plasma density decreased after the lithium coating similar to the behavior of the intensity of the impurities which decrease after the lithiumization of the chamber as shown in Figure 3.10 - 3.12.

The intensities radial profile of the impurity lines, with and without lithium are compared in Figure 3.14. The intensity profiles of the impurities at the base pressure, $P = 1.6 \times 10^{-4}$ Torr is plotted in black color, at $P = 1.2 \times 10^{-4}$ Torr is plotted in blue color, at $P = 0.8 \times 10^{-4}$ Torr is plotted in red color and at $P = 0.6 \times 10^{-4}$ Torr is plotted in magenta color.

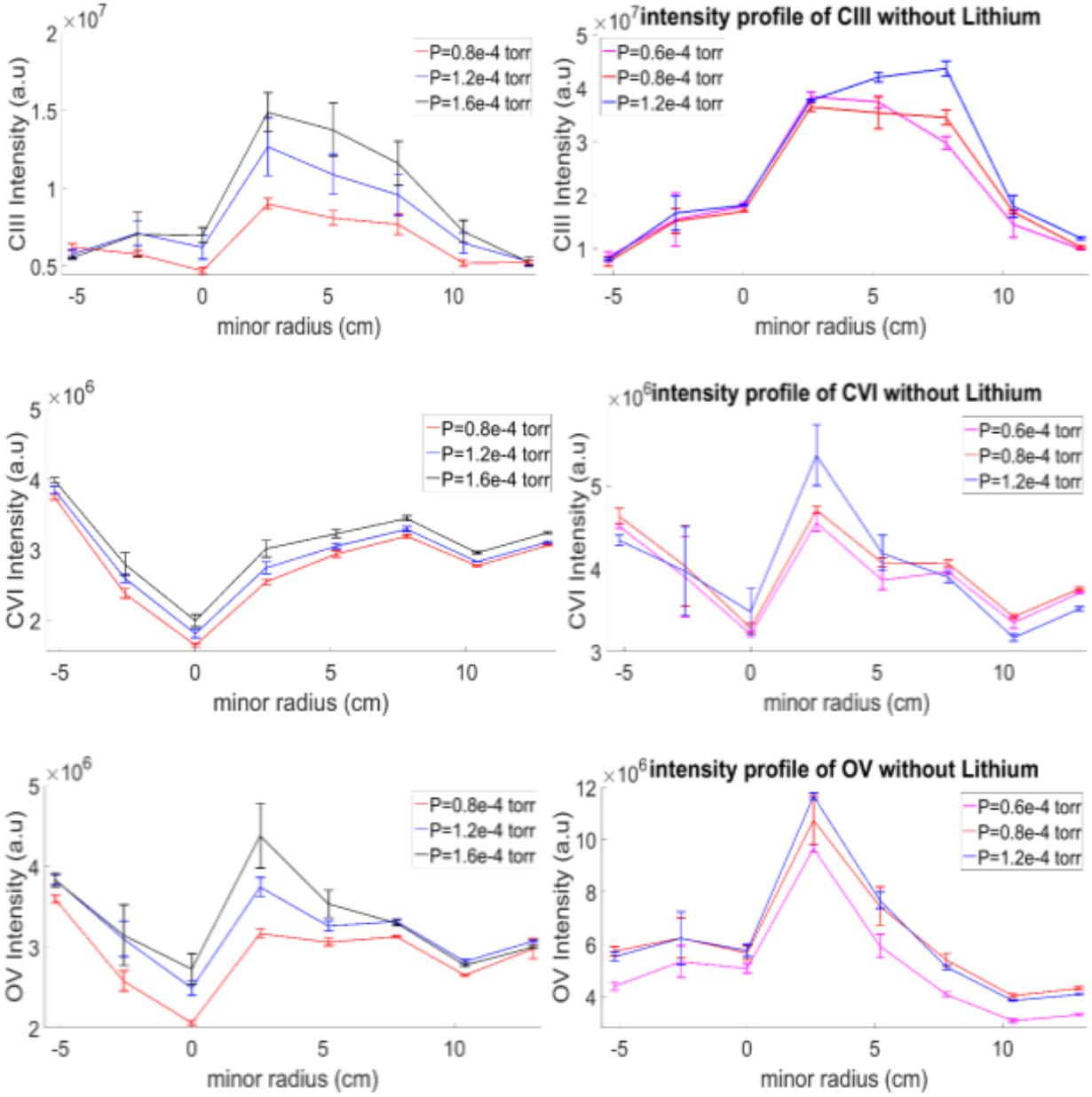

Figure 3.14: Intensity profiles of the impurity lines at different base pressures with lithium (panels on the left), and without lithium (panels on the right).

It can be concluded that by increasing the base pressure, the plasma density is increased as expected. This is part of the reasons why the increase in base pressure increases the impurity intensities since the line emission is proportional to the electron density in the plasma.

3.12 Effective Lifetime of Coated Lithium in the STOR-M Tokamak

A further experiment was carried out to determine how many plasma shots will wear out the coated lithium from the STOR-M tokamak chamber. This experiment was done by continued running the STOR-M tokamak and accumulating plasma discharge over one week for each case considered. The intensity of the impurity lines and that of the lithium were measured after 300, 600, and 900 plasma shots following the lithium coating. The emission line from Li I (670.8 nm) with a transition between $1S^2 2S - 1S^2 2P$ [52] was recorded by the Czerny-Turner Spectrometer discussed in Chapter 2. This information gives us insight into how many plasma discharges it takes before it is needed to re-coat lithium in the STOR-M tokamak. In the EAST machine, the effective lifetime of lithium film was observed to be up to 40 shots. In the STOR-M tokamak, after 300 shots of continuous plasma discharge, the intensity of lithium has reduced to more than half of its initial intensity as shown in Figure 3.15. Each data point in the diagram represent the average over five (5) shots. The measurement of the lithium intensity after 600 and 900 shots of plasma discharges revealed that intensity of the lithium stayed approximately the same with a slight decrease.

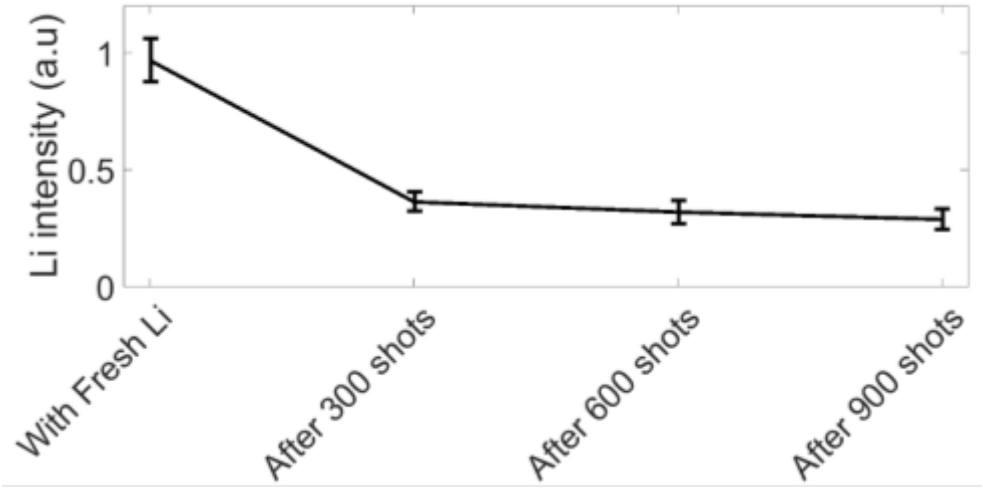

Figure 3.15: Intensity of lithium.

With the decrease in the intensity of the coated lithium, it is expected that the intensity of the emission lines, CIII, CVI, and OV would increase after 300, 600, and 900 plasma shots due to reduced effectiveness of the lithium coating after many shots. Further analysis of the experimental results from the emission line measurement did not conform to our expectations. Figure 3.16 – Figure 3.18 shows the bar plot of the intensities summed up over eight channels of the fiber cables during plasma discharge without lithium, with freshly coated lithium, after 300 shots, after 600 shots, and after 900 shots of plasma discharges.

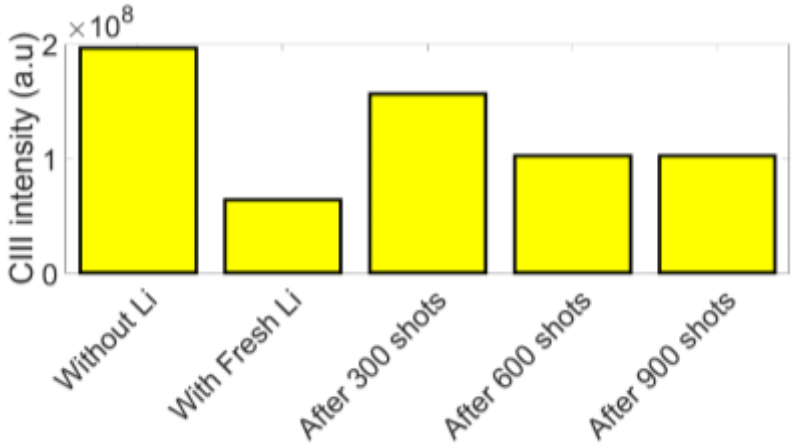

Figure 3.16: Line integrated intensity of CIII.

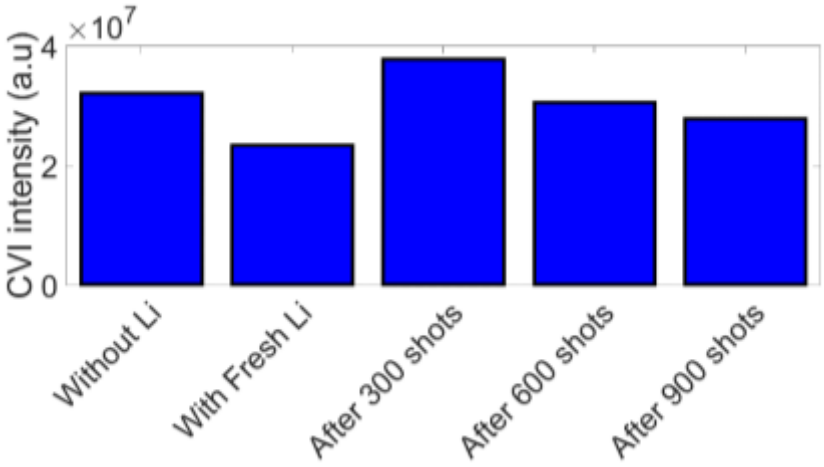

Figure 3.17: Line integrated intensity of CVI.

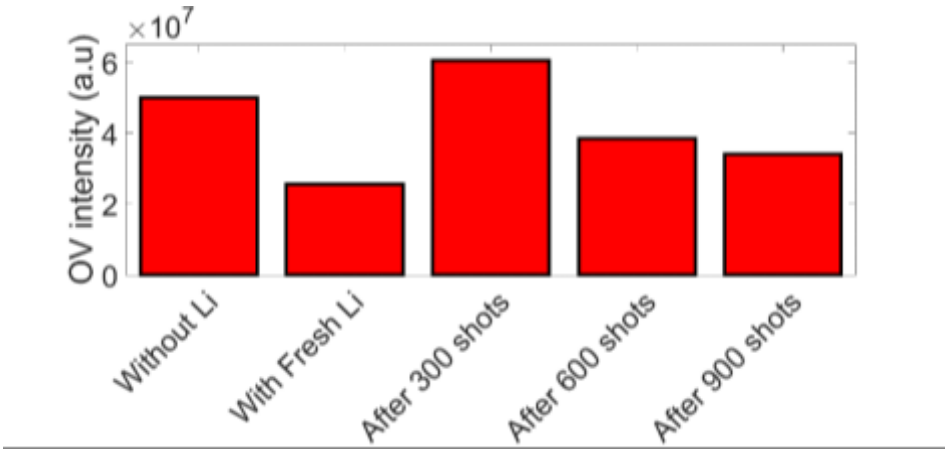

Figure 3.18: Line integrated intensity of OV.

It is seen from the Figures above that without lithium, the intensity of the impurities was large, and intensity decreased with freshly coated lithium, it increased after 300 shots as expected since the lithium coating effects are projected to reduce after many shots. The impurities emission intensities decrease again after 600 and 900 shots. These results appear to disagree with the plot in Figure 3.15 since it is expected that reduced lithium intensity after 600 and 900 shots of plasma discharges would increase the intensity of the impurity. The decrease in the intensity of the impurity line emission intensities after 600 and 900 shots may be attributed to discharge cleaning of the chamber walls which has been noted before without lithium coating. The idea of lithiumization of the inner surface wall was to reduce the high-Z impurities like iron, carbon, and oxygen in tokamaks. Lithiumization of the inner surface of tokamaks is not the only way to lessen the influx of high-Z impurities in tokamaks to achieve proper plasma parameters. Other methods include boronization [54], glow discharge cleaning (GDC) [55], and plasma discharge cleaning [3]. By repetitively running the tokamak, the contamination layers on the wall surfaces are depleted, a low density of impurities are experienced, and a good plasma parameter is achieved.

3.13 Effect of Lithium on Plasma Density

Further analysis of the plasma parameters recorded after the lithium coating experiment showed that plasma density was significantly reduced. This result is similar to the result reported in RFX-mod tokamak [56] and LTX [20]. The density after the lithium coating was low because coated lithium absorbed most of the neutral particles puffed into the chamber. The plasma density could

only be increased by increasing the density of the neutral gas, and the density of the neutral gas is increased by increasing the base pressure. Figure 3.19 showed the plot of the plasma density when the intensities of the impurity were captured without lithium, with freshly coated lithium after 300, 600, and 900 shots of plasma discharge.

The plasma density before lithium coating was compared with the density after freshly coated lithium, density after 300 shots, after 600 shots, and after 900 shots of plasma discharge in Figure 3.19. As it is seen, the plasma density was high before the introduction of lithium, it then dropped to more than half of the initial density (density without lithium) after the freshly coated lithium. The density went up after 300 plasma discharges, even higher than the case without lithium, and become almost constant after the 600 and 900 shots respectively. This result is similar to what was observed in the event of the intensities of the impurity as shown in Figure 3.16 – 3.18, most especially the case of CVI and OV intensities. The intensities of CVI and OV increased after 300 shots more than the case without lithium. It can be concluded that the higher the plasma density, the more plasma-wall interaction is experienced, and the higher the activities of impurities in the tokamak plasmas.

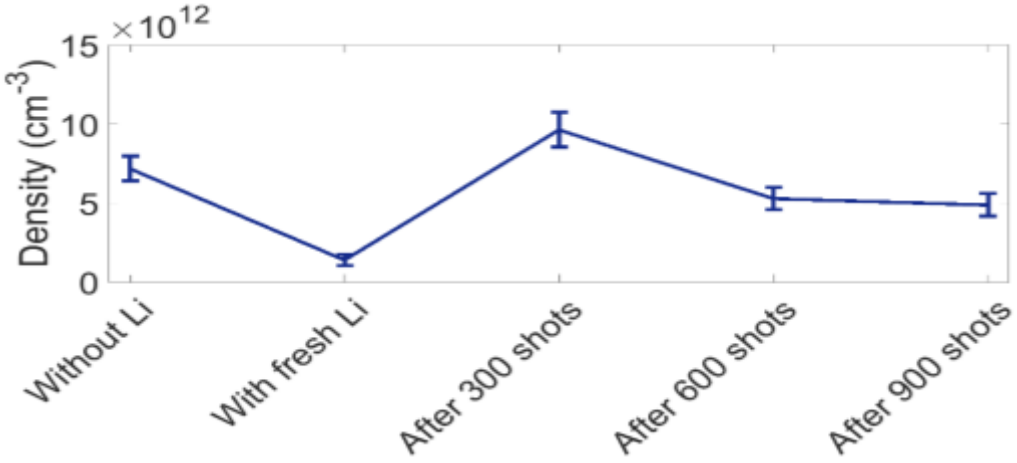

Figure 3.19: Plasma density with and without lithium.

In this Chapter, it has been demonstrated on STOR-M tokamak like other devices that lithium coating is a significant way to reduce wall recycling and suppress unwanted impurities which prevent plasma from being heated to the desired temperature.

Chapter 4

Shielding Effect of Plasma on RMP Fields in the STOR-M Tokamak

4.1 Introduction

Plasma, which is made up of ionized gas (electrons and ions), is a conducting fluid, with electrons carrying the current that flows through it because ions are massive. Plasmas exhibit a character similar to a good conductor when a time-varying magnetic field is applied to them. When magnetic fields are applied to the plasma, an eddy current is induced by the change of the externally imposed magnetic field. The shielding of the external field also leads to the attenuation of the external field compared with the case without plasma. The attenuation of the external fields allows us to determine shielding effect of plasma. The induced magnetic field from the plasma is vectorially added to the applied external magnetic field to produce a resultant field. The resultant magnetic field measured after the application of the external field also experiences a delay in time (phase shift). The attenuation and the phase shift of the plasma response measured will enable us to determine the shielding effect of plasma.

The Resonant Magnetic Perturbation (RMP) system discussed in Chapter 2 of this thesis will be used to apply an external magnetic field to the plasma in STOR-M. The RMP current will be fired with (plasma and chamber wall) and without (chamber walls only) plasma; the induced resultant magnetic fields will be measured by the internal radial magnetic probe described in Chapter 2 of this thesis. The measured magnetic fields will be used to determine the shielding effect of the plasma.

In this Chapter, an overview of the theory of skin depth in plasma will be presented in Section 4.2, the experimental set-up will be discussed in Section 4.3, a method of data analysis will also be presented in Section 4.4, and the experimental results are reported in Section 4.5.

4.2 Skin Effects in Plasma

Skin effect is a phenomenon whereby electromagnetic fields decay as they penetrate into a conducting medium. This effect occurs in metals, plasma, ionosphere, degenerative semiconductors and other media with sufficiently high conductivity [57]. The equation that

describes skin effect in conducting material can be derived from the four Maxwell's equations assuming linear media [41].

$$\nabla \cdot \mathbf{E} = \frac{\rho_f}{\epsilon} \tag{4.1}$$

$$\nabla \cdot \mathbf{B} = 0 \tag{4.2}$$

$$\nabla \times \mathbf{E} = -\frac{\partial \mathbf{B}}{\partial \mathrm{t}} \tag{4.3}$$

$$\nabla \times \mathbf{B} = \mu\sigma\mathbf{E} + \mu\epsilon\frac{\partial \mathbf{E}}{\partial \mathrm{t}} \tag{4.4}$$

Applying the curl to equation (4.3) and (4.4), we have modified field equations for **E** and **B**:

$$\nabla^2\mathbf{E} = \mu\epsilon\frac{\partial^2 \mathbf{E}}{\partial \mathrm{t}^2} + \mu\sigma\frac{\partial \mathbf{E}}{\partial \mathrm{t}} \tag{4.5}$$

$$\nabla^2\mathbf{B} = \mu\epsilon\frac{\partial^2 \mathbf{B}}{\partial \mathrm{t}^2} + \mu\sigma\frac{\partial \mathbf{B}}{\partial \mathrm{t}} \tag{4.6}$$

Assume plane field that propagates in the *z*-direction with a frequency ω, the solution of (4.5) and (4.6) will be;

$$\mathbf{E}(\mathrm{z}, \mathrm{t}) = E_0 e^{j(\tilde{k}z - \omega t)} \tag{4.7}$$

$$\mathbf{B}(\mathrm{z}, \mathrm{t}) = B_0 e^{j(\tilde{k}z - \omega t)} \tag{4.8}$$

The solution of (4.5) and (4.6) using (4.7) and (4.8) gives complex wave vector $\tilde{k}$;

$$\tilde{k}^2 = \mu\epsilon\omega^2 + j\mu\sigma\omega \tag{4.9}$$

Rewrite

$$\tilde{k} = k + j\varkappa \tag{4.10}$$

then

$$\tilde{k}^2 = k^2 - \varkappa^2 + 2jk\varkappa \tag{4.11}$$

Comparing (4.11) with (4.9), and solving a quadratic equation of power 4, we have

$$k = \omega\sqrt{\frac{\epsilon\mu}{2}}\left[\sqrt{1 + \left(\frac{\sigma}{\epsilon\omega}\right)^2} + 1\right]^{\frac{1}{2}} \tag{4.12}$$

$$\varkappa = \omega\sqrt{\frac{\epsilon\mu}{2}}\left[\sqrt{1+\left(\frac{\sigma}{\epsilon\omega}\right)^2}-1\right]^{\frac{1}{2}} \tag{4.13}$$

The imaginary part of (4.10) results in an attenuation of the amplitude of both the electric and magnetic field of (4.7) and (4.8) as the fields penetrate or propagate.

Substituting for $\tilde{k}$ in (4.8) with (4.10), we have for the case of magnetic field only;

$$\boldsymbol{B}(z,t) = B_0 e^{-\varkappa z} e^{j(kz-\omega t)} \tag{4.14}$$

Replacing $e^{j(kz-\omega t)}$ with $\cos(k_0 z - \omega t + \varphi) + j\sin(k_0 z - \omega t + \varphi)$ in (4.14), considering only the real part, and assume the field is in the y-direction, we have:

$$\boldsymbol{B}(z,t) = B_0 e^{-\varkappa z}\cos(k_0 z - \omega t + \varphi)\,\hat{y} \tag{4.15}$$

where $\varphi = (k - k_0)z$ is the phase shift of the field compared with the phase field in vacuum.

The amplitude of the magnetic field is attenuated as the field propagates in the z-direction. The distance it takes to attenuate the magnitude by a factor of 1/e is called the skin depth:

$$d = \frac{1}{\varkappa} \tag{4.16}$$

This parameter measures how far the field penetrates into the conducting material like plasma before being significantly attenuated.

From equation (4.13), $\varkappa$ is a function of σ (conductivity of the material) and ω (frequency of the field), for the case in which the conductivity of the material is far greater than the frequency of the field i.e. $\sigma \gg \epsilon\omega$; equation (4.13) reduces to

$$\varkappa = \sqrt{\frac{\omega\sigma\mu_0}{2}} \tag{4.17}$$

Substitution these into equation (4.16), we have:

$$d = \sqrt{\frac{2}{\sigma\mu_0\omega}} \tag{4.18}$$

Skin depth is inversely proportional to the square root of the conductivity of the media and the frequency of the external field. It is worth noting that the conductivity of a plasma varies with the

plasma temperature and the plasma temperature also varies with the plasma radius. The conductivity of a fully ionized plasma in cgs units [58] is:

$$\sigma = \frac{3m_e}{(16\sqrt{\pi})Ze^2 \ln \Lambda}\left(\frac{2T_e}{m_e}\right)^{\frac{3}{2}} \tag{4.19}$$

where m_e is the electron mass, Z is the ion charge; T_e is the electron temperature and $\ln \Lambda$ is Coulomb logarithm whose value is approximately 15 for burning plasma and other plasmas in a wide range of parameters [42].

In a tokamak, the plasma temperature is not uniform; it is higher at the plasma center compared to the plasma edge. If a field is applied to such a plasma, the magnetic field will experience decay as it propagates into the hottest part of the plasma, because high temperature implies high conductivity and high conductivity results in a short skin depth. The applied field will only travel a small distance before its amplitude is reduced by a factor of *1/e*.

For example, the electron temperature in the STOR-M tokamak was estimated at the plasma edge to be approximately 20 eV. For a hydrogen plasma with Z = 1 and $\ln \Lambda$ = 15, the estimated conductivity is $1.1\times10^5\ \Omega^{-1}$. The frequency of RMP current was also estimated to be 1.5 kHz using Fast Fourier Transform (FFT) command in MATLAB. Based on Equation 4.18, the skin depth at the plasma edge was estimated to be 3.9 cm. This shows that externally applied RMP field will only travel a distance of 3.9 cm before its amplitude is reduced by a factor of *1/e* in the STOR-M tokamak.

It is important to take into consideration of the effect of the STOR-M tokamak vacuum chamber wall; the vacuum vessel is made up of stainless steel; it has a conductivity of $1.5\times10^6\ \Omega^{-1}$. The RMP coil that produces the magnetic field is strapped to this vacuum chamber. The magnetic fields induced by the RMP coils penetrate through the conductor before they reach the plasma. It is expected that the vacuum chamber also contributes to the shielding of the RMP field.

The skin depth of the RMP field due to the STOR-M tokamak vacuum chamber was calculated to be 1.1 cm, but the thickness of the vacuum chamber is 0.4 cm, so it is not likely that the RMP field will be attenuated significantly by the tokamak chamber wall.

4.3 Experimental Set-up

The internal radial magnetic probe array described in section 2.3.7 of this thesis was installed on a normal port close to one of RMP helical coils strapped to the outside walls of the STOR-M tokamak. The coils were installed in such a way that the total induced magnetic field components add up to zero as they propagate to the geometric center (r = 0 cm) of the tokamak chamber. The magnetic probes were designed to measure magnetic fields at four different radial locations during a single plasma discharge. The magnetic probe array was used to measure RMP field in a vacuum (without plasma) and plasma. The signals picked up by the probes were transmitted by BNC cables across the tokamak room to an analog gated integrator, but the gated integrator did not work properly. Therefore, digital integration was employed, and the calibration factors in Table 2.3 is not applicable for the digitally integrated signals. A new calibration process was required for the magnetic probe array before the experiment was conducted. This process involved the use of the calibration factors presented in Table 2.3.

In the case of new calibration, the RMP current was used as a reference current to calibrate the magnetic probes since the RMP coil is located close to the installed internal magnetic probe. The Helmholtz coil could not be utilized for the new calibration because the magnetic probes have already been installed on the tokamak before realizing that the analog gated integrator was not working properly. The RMP capacitor bank was charged to 400 V (kept constant throughout the calibration process). It was discharged in a vacuum (without plasma). The signals picked up by the probes were integrated using the active integrator described in Section 2.4.6. Figure 4.1 shows raw (un-integrated) signals of the magnetic probes.

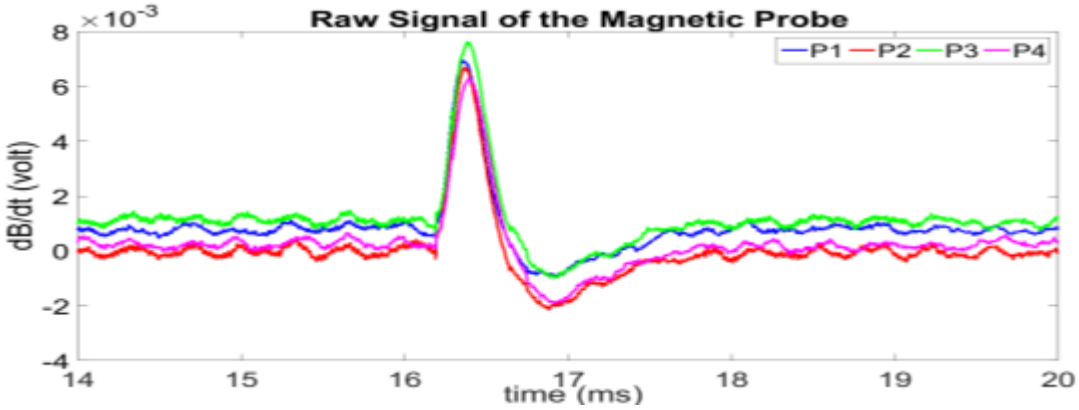

Figure 4.1: Un-integrated signal of the internal magnetic probes.

A typical waveform of the signal integrated by active integrator is shown in Figure 4.2 (left). Five shots (samples) were collected. To eliminate the inconsistency in RMP current that induced the magnetic field picked up by the probes, each amplitude of the magnetic probe signals was divided by the magnitude of the RMP current producing it. The signals integrated with the active integrator were converted to Gauss using the calibration factors in Table 2.3, and the average of the five shots, as well as their standard deviation, were calculated. Another five raw signals of the magnetic probe were collected and integrated digitally using MATLAB "cumsum" command. The waveform of the signal integrated numerically by MATLAB, without calibration, is shown in Figure 4.2 (right). The amplitude of each of the digitally integrated signals was also divided by the magnitude of the RMP current to eliminate inconsistency. The result of the analog integrated signal multiplied by the initial calibration factor was divided by the result of the digitally integrated signal to obtain another set of calibration factors for each of the probes. The result of the new calibration is presented in Table 4.1. These factors were used during the experiment to determine the magnitude of the magnetic field picked up by the internal magnetic probe array described in section 2.4.7.

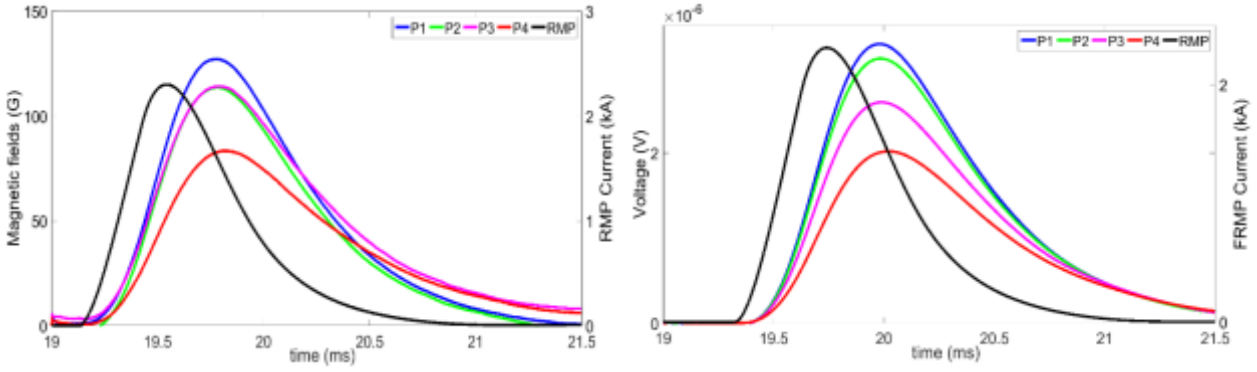

Figure 4.2: Integrated waveform using an analog integrator (left) and digitally integrated waveform (right).

Table 4.1: New calibration factor.

Magnetic Probes	Calibration Factors (G/V)
P1	$(4.00\pm0.03)\times10^{7}$
P2	$(3.80\pm0.27)\times10^{7}$
P3	$(4.40\pm0.16)\times10^{7}$
P4	$(4.10\pm0.63)\times10^{7}$

The DC offsets in Figure 4.1 were removed in Figure 4.2 by subtracting the average of 1000 data point taken before the start (19 ms) of each of the magnetic probe signals from the magnetic probe signals. This correction brings the start of the plots in Figure 4.2 to 0 on the y-axis.

It can be seen in Figure 4.2 that the analog and the digitally integrated waveform of the magnetic probes lag behind the RMP current, the phase shift is due to the chamber walls between the RMP coils (the source field) and the magnetic probes (the probe location). When the RMP field was measured in air, there was no noticeable phase shift between the RMP current waveform and the magnetic probe waveforms. The plot of the waveforms of the RMP current and the magnetic probe is shown in Figure 4.3.

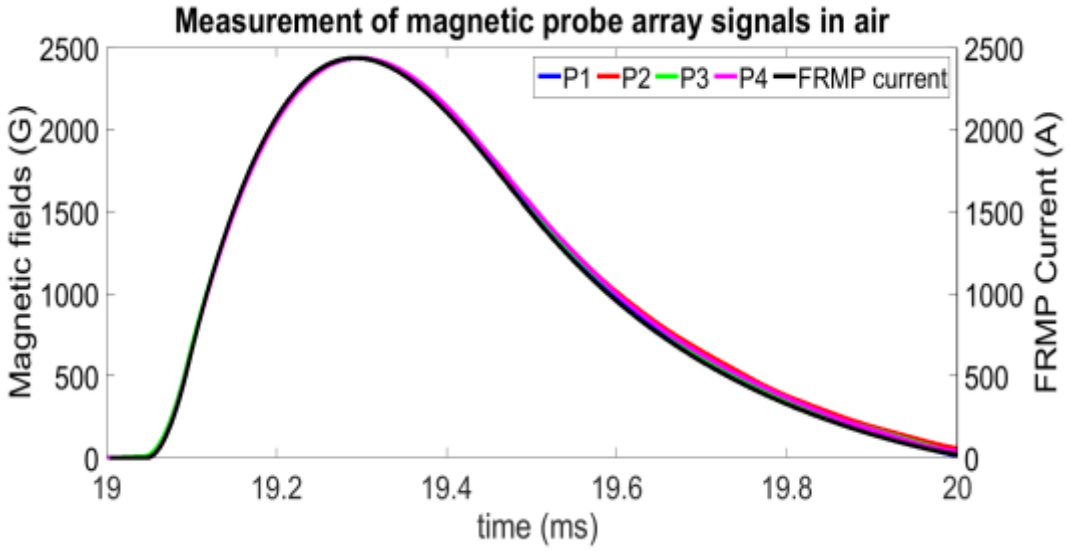

Figure 4.3: RMP magnetic field in air integrated digitally.

The waveforms of the magnetic probes in the Figure 4.3 above were normalized to the RMP current, so that delay in any of the plots will be visible, but it is seen that there was no delay in the peaks of the magnetic probe waveforms compared to the RMP current waveform, since the peaks of all the waveforms perfectly align. This shows that the delay observed in Figure 4.2 was due to the chamber of the vacuum wall.

4.4 Data Analysis

The magnetic fields induced by the RMP coils were measured at different RMP capacitor voltages during plasma discharge. The RMP power supply was discharged during plasma current flat top. Flat top indicates stable plasma as shown in Figure 4.4.

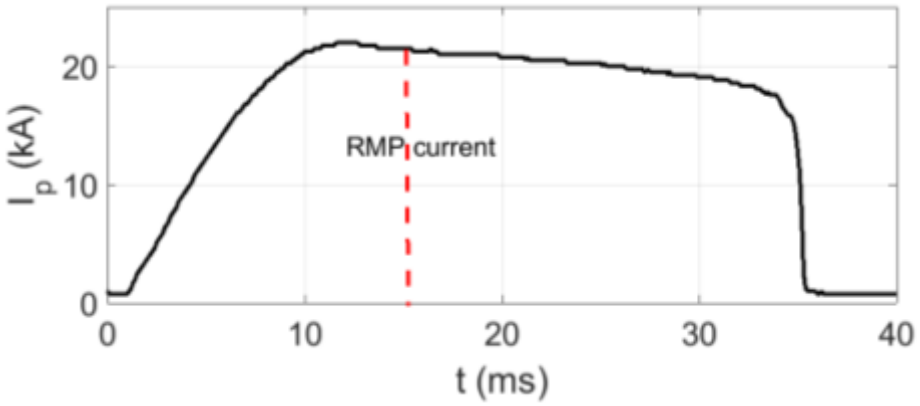

Figure 4.4: Plasma current waveform with the red vertical line indicating the time when the RMP current was applied.

The red dash line in Figure 4.4 indicates the time and the magnitude of the plasma current when RMP current was applied. The amplitude of the plasma current at that period is around 21 kA, and the corresponding time is 16 ms.

The RMP capacitor voltage considered are; 100 V, 150 V, 200 V, 250 V, 300 V, 350 V, and 400 V but a noticeable signal strength picked up by the magnetic probe array after integration and calibration were observed at 400 V. So, the plasma effect experiment was performed at RMP power supply of 400 V. The RMP current to the helical coil was monitored by a home-made Rogowski coil with a calibration factor of 520 amperes/voltage and analog integrator with a time constant of 0.4 ms. The current driven by a capacitor voltage of 400 V is around 0.8 kA.

Besides, the location of the innermost probe in the array (P1) was varied between plasma discharges, and it was observed that the probe perturbs plasma at r = 11.5 cm, and caused plasma disruption. Thus, the plasma effect on RMP field was measured at a minor radius of r = 12.5 cm, 13.5 cm, 14.5 cm and 15.5 cm from the geometric center of the tokamak chamber. The plasma current and loop voltage after a plasma disruption are shown in Figure 4.5 for shot #:301610.

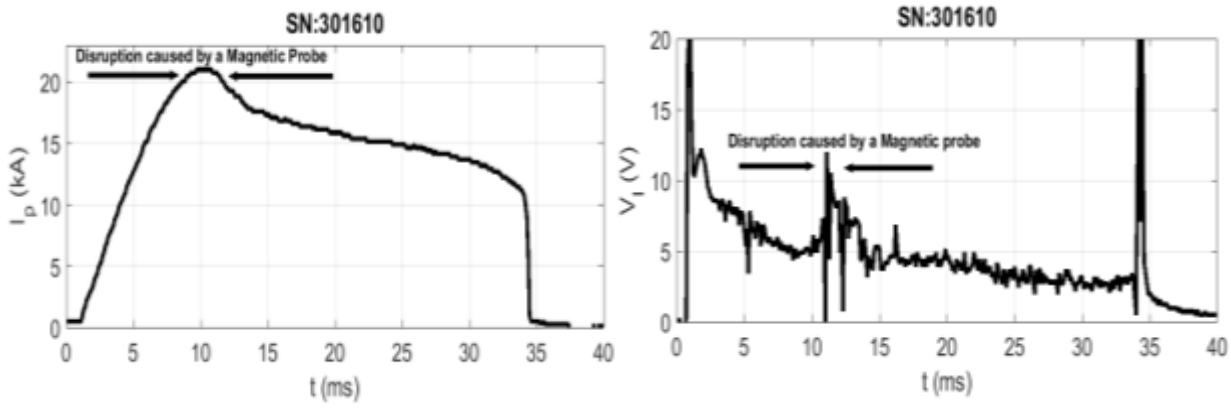

Figure 4.5: Plasma parameters during disruption: plasma current (left) loop voltage (right).

The data acquisition system recorded the magnetic field signals measured by the magnetic probe array after the plasma discharge and then integrated digitally using MATLAB "cumsum" command. The integrated signal was multiplied by the new calibration factor listed in Table 4.1 to convert the pickup signal into a magnetic field in Gauss (G). Each integrated magnetic field of the probes was divided by the amplitude of the source current, RMP current, to determine the field per unit RMP current.

Several discharges were performed for the same minor radii, and the plasma response at four different radii location for a single plasma discharge was measured. These minor radii locations are r = 12.5 cm, 13.5 cm, 14.5 cm, and 15.5 cm, and the magnetic probes P1, P2, P3, and P4 are located at these radii respectively. The plot of the waveform of the magnetic probes (in plasma) multiplied by the new calibration factors (normalized to the RMP current (G/kA)) and the RMP current waveform is shown in Figure 4.6 (top). When the RMP current was applied without plasma, the signals picked up by the probe array have the same characteristics as the case when the RMP current was applied with plasma after integration. The signals drift with time. The plot of the magnetic fields measured in a vacuum with corresponding RMP current is shown in Figure 4.6 (bottom).

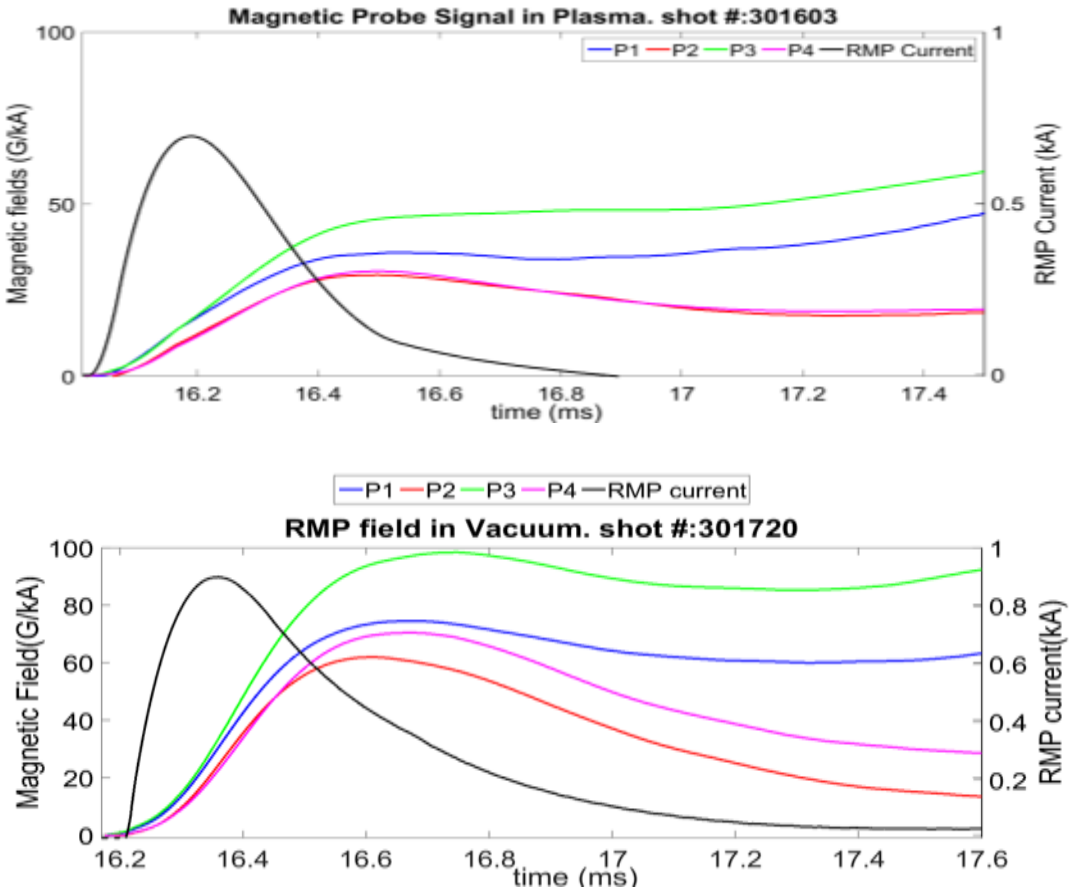

Figure 4.6: Digitally integrated magnetic field measured when RMP current was applied in plasma (top) and in vacuum (bottom).

The black curve is the RMP current, the blue curve is the magnetic field picked up by the probe P1, (innermost probe), the red curve is the magnetic field of P2, the green curve is the magnetic field of P3, and the cyan curve is the magnetic field of P4 (outermost of the probes).

As it is seen in Figure 4.6, the magnetic probe signals do not look like the RMP current waveform that induced them. One of the reasons for the drift is the small DC offset of the signal on top of the induced magnetic field to be measured. For example, the digitizer sometimes induces a small DC offset to the signal measured through it. The DC drift causes a linear increase in the signal after integration. This DC drift and other noises add to the signals picked up by the probes array, distorted and changed the waveform of the probe signals. The DC offset and the noises make it difficult to determine the peak magnitude of the picked-up field. Several discharges were collected for both RMP with, and without plasma, all the signals picked up by the magnetic probes were perturbed by the DC offsets that vary with time.

If the amplitude of the DC offset is known, the value can be subtracted from the total signal picked up by the magnetic probe array to determine the magnetic field of the probes.

The value of the DC offset was calculated numerically using MATLAB. This was done by first of all evaluating the slope of the DC offset added to each signal picked up by the probes. The slope of the DC offset was then used to generate the value of the DC offset. The slope was calculated using the first and the last data point of the plot to be corrected. The equation of a straight line was used to determine the value of the DC offset. The equation of a straight line is written as

$$Y = Y_1 + m(X - X_1) \tag{4.20}$$

where m is the slope of the two distinct points taken, while Y_1 and X_1 are the coordinates of the data point picked at the beginning of the drifted waveform, Y is the value of the DC offset. The result of Equation 4.20, which is Y, was subtracted from the integrated signal picked up by the magnetic probes to eliminate the DC offset. Figure 4.7 shows a typical magnetic probe signal waveform before correction, and the corresponding corrected waveforms.

Figure 4.7 (right) shows the RMP current, and magnetic probes waveforms after the value of the DC offset have been subtracted. Since the main purpose is to evaluate the delay time and the relative amplitudes of the probe signal, the magnetic fields measured by the magnetic probes are normalized to the peak RMP current. The normalization is also necessary to average over many shots during which the RMP currents may not be the same.

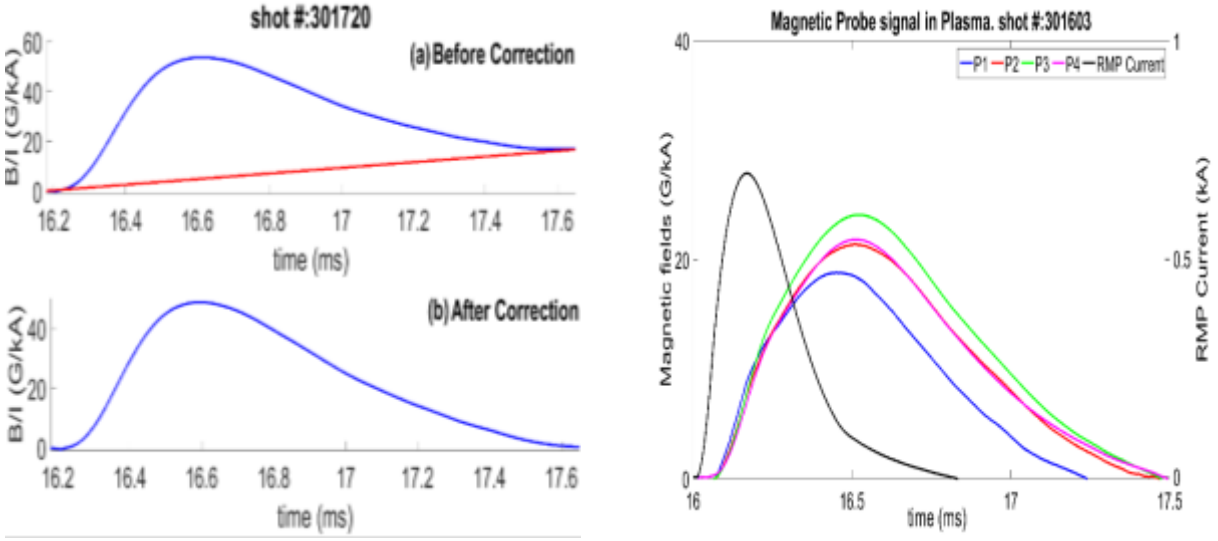

Figure 4.7: Magnetic field waveform: correction process (left) and corrected waveforms (right).

4.5 Experimental Results

The RMP capacitor bank was charged to 400 V to drive a current of about 0.8 kA, and this current was applied to the plasma around 16 ms when the plasma parameters are relatively stable. The plasma parameter during the experiment are current, I_p = 22 kA, loop voltage, V_l = 3 V, and the plasma position is roughly around the geometric center of the tokamak chamber. All the plasma discharges during the experiment have similar features. The plasma shielding effect was evaluated by calculating the difference between the magnitudes of the magnetic probe signals in a vacuum (B_v) and plasma (B_p) at four different radial locations for a single plasma discharge using the corrected waveform as in Figure 4.7. Data for five similar shots were collected. The average of the samples, as well as their standard deviation, were calculated. The magnetic field profile of the effect is plotted in Figure 4.8. The red curve is the RMP field without plasma, the blue plot is the RMP field with plasma, and the green plot is the difference between the magnetic fields measured with plasma and without plasma. The difference between the magnetic fields is the plasma shielding effect. The horizontal axis is the minor radius of the STOR-M tokamak where the fields were measured. The radius r = 12.5 cm is closer to the plasma center than r = 15.5 cm.

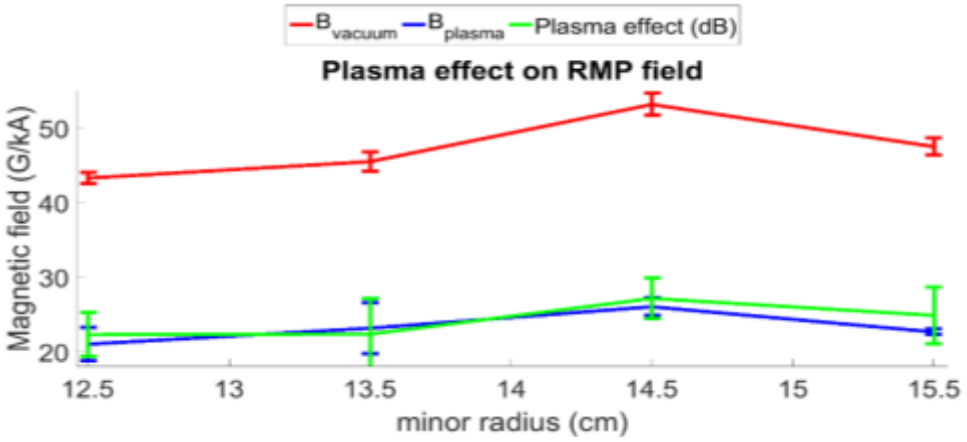

Figure 4.8: Plasma effect on RMP field.

As seen in Figure 4.8, the magnetic field increases as it propagates into the vacuum (without plasma), and it reached a maximum at 14.5 cm and then started to decrease as it propagates into the vacuum chamber. The vacuum field (red curve), the magnetic field measured in plasma (blue curve), and the plasma response (green plot), all behaved similarly as they propagate into the chamber. Moreover, it is seen that the vacuum field (red curve) is approximately 50% greater than

the plasma response measured (blue curve) and the plasma effect (green curve) is almost the same as the total magnetic field measured. The result above justifies the claim that plasma is a conducting medium because approximately 50% of the RMP field were shielded by the plasma. The shielding effect is due to the high temperature of the plasma which indicates high conductivity as shown in Equation 4.19.

The time taken by the RMP fields presented in Figure 4.8 to penetrate the plasma was determined. The time corresponding to the peak of the corrected waveform of the magnetic probe array in Figure 4.7 was used to determine the RMP field penetration time. The penetration time was investigated at four different radial locations from the RMP helical coil located outside the tokamak walls. The RMP field penetration time, t_p is the difference between the vacuum time, t_v and the vacuum-plasma time, t_{vp}. The vacuum time, t_v is the time between the peaking time for the probe signal and the RMP current when the RMP is applied without the plasma. Similarly, t_{vp} is the time difference for the case with plasma. The net plasma response to RMP penetration time was calculated using Equation 4.21

$$t_p = t_{vp} - t_v \tag{4.21}$$

The RMP current waveform and magnetic probe waveforms showing the peaks at which the penetration time was calculated with and without plasma are shown in Figure 4.9 and Figure 4.10.

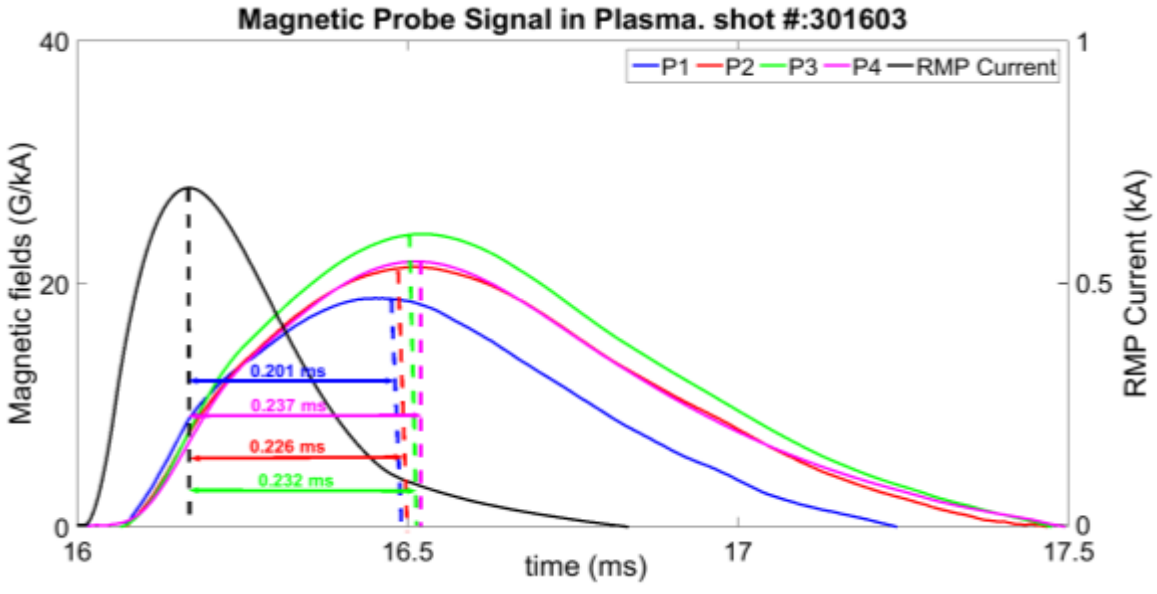

Figure 4.9: RMP field by the magnetic probe array in plasma.

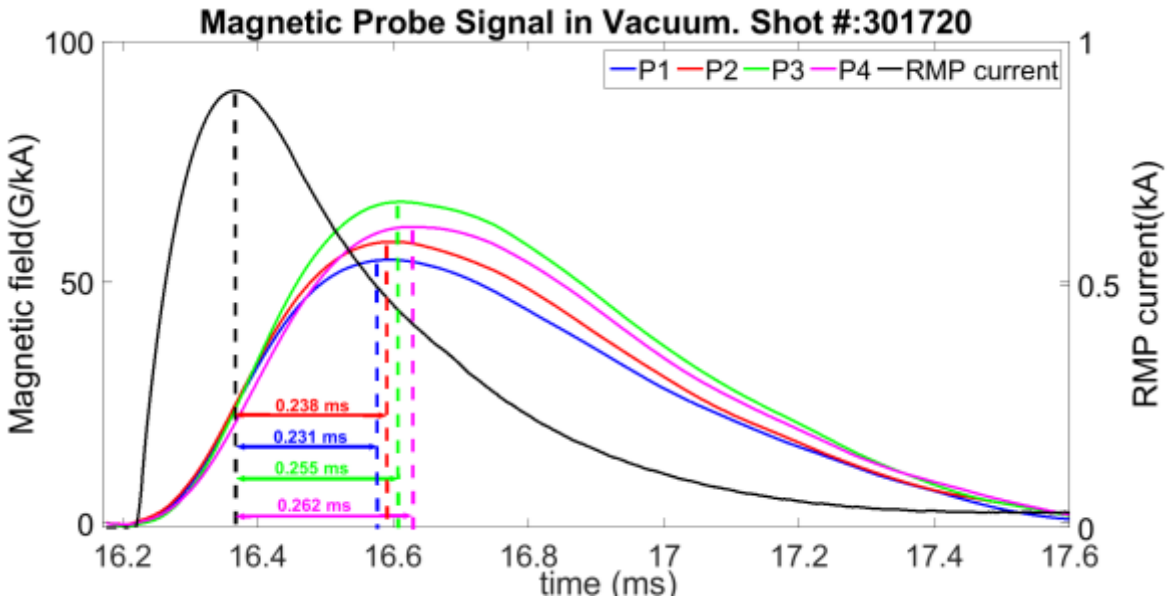

Figure 4.10: RMP field by the magnetic probe array in vacuum.

The magnetic fields induced by the RMP coils, with and without plasma, were measured at minor radii r = 12.5 cm, 13.5 cm, 14.5 cm, and 15.5 cm from the chamber geometric center. The RMP field penetration time profile, as calculated using Equation 4.21, at the four different radial locations is plotted in Figure 4.11.

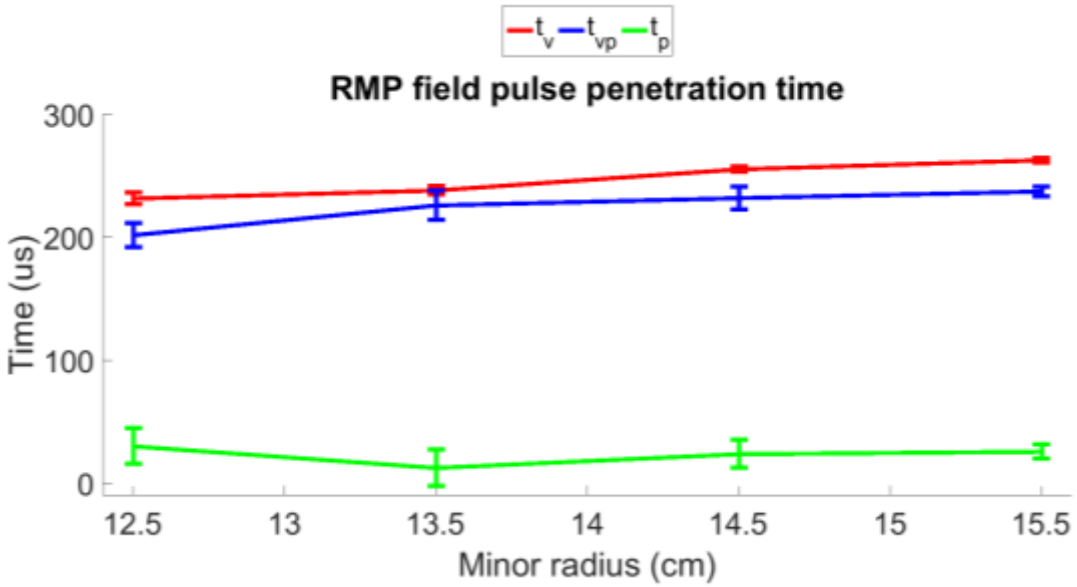

Figure 4.11: RMP field penetration time.

The blue curve is the penetration time through plasma and wall, the red curve is penetration time through the vacuum, and the green curve is the plasma response to the field penetrate time. Minor radius, r = 12.5 cm is inside the plasma, while r = 15.5 cm is the edge of the chamber wall.

Considering the Figure 4.11, in a vacuum (red curve), it took 231.2 us for the RMP pulse to propagate through the chamber wall to the minor radius, r = 12.5 cm, it took 237.8 us to propagate to r = 13.5 cm, it took 255.0 us to propagate to r = 14.5 cm, and 262.4 us to propagate to r = 15.5 cm. These results show that the field penetration time decreases as the field propagates through the vacuum chamber marginally, almost within the error bars of the data. When the RMP field was applied to the plasma, the field penetration time is shorter, 201.4 us to radius r =12.5 cm, 225.6 us to r = 13.5 cm, 231.6 us to r = 14.5 cm, and 237 us to r = 15.5 cm. These do not seem to be expected results. Because plasma is a conducting medium and its conductivity varies with temperature profile, the penetration time of the RMP field should increase as the field penetrates into the core of the plasma. If we assume that the conductivity of the plasma is approximately the same at the edge of the plasma, there should still be an increase in the penetration time as the field propagates into the plasma. The field penetration time (green curve) at r = 12.5 cm is 29.8 us, r = 13.5 cm is 12.2 us and r =14.5 cm is 23.4 us and at r = 15.5 cm is 25.4 us. The change in the penetration time as a function of the probe is not significant if the wavelength of the RMP signal is long compared to the separation distance of the probes. Another feature observed in the probe signal is the broadening of the induced field with respect to the RMP current due to the dispersive nature of the plasma media, this broadening will affect the amplitude of the magnetic field measured and the corresponding time at which the magnetic field signals peaked.

In this particular setup, the phase shift calculated in Section 4.2 is based on a plane wave entering an infinitely large flat surface. In the situation for the RMP coil and the STOR-M tokamak, the response time of the vacuum chamber or the combined system including both the vacuum chamber and the plasma (acts as the secondary winding of a transformer) to the RMP current (acts as the primary winding) is characterized by the resistance R_p and the self-inductance L_p of the secondary winding. For the m = 1 or the n = 1, the response time is expressed by [59]

$$\tau_p = \frac{L_p}{R_p} \tag{4.22}$$

where R_p is plasma resistance, and L_p is plasma inductance.

It was observed in this Chapter that STOR-M tokamak plasma attenuated the RMP fields applied to it. The RMP field applied to the plasma was reduced by 50% compared to the field measured without plasma. It was also observed that time taken for the RMP field to penetrate plasma was short compared to the time required to propagate through the vacuum. The reason for this result is unknown because with plasma being a conducting fluid, any external field applied to it should travel slower. In other words, if the plasma has a small resistance, the time response to an external magnetic field applied to it should be large as in Equation 4.22.

Chapter 5

Summary and Suggested Future Work

5.1 Summary

Impurities are part of the major problems to be resolved in tokamaks before fusion reactors are available for public use because impurities prevent plasma from being heated to the desired temperature. Impurities in tokamaks depend on the type of the material walls a tokamak is made of. Like other tokamak devices, lithium has been demonstrated on the STOR-M tokamak to help reduce the activities of impurities on the plasma. Lithium was introduced into the STOR-M tokamak's chamber using a lithium evaporator. The effects of lithium coating were investigated on the brightest emission lines in the tokamak. The emission lines are from Carbon ions (CIII and CVI) and Oxygen ion (OV).

The result of the experiments showed that with the introduction of lithium in the STOR-M tokamak, 28% of CIII intensity was suppressed, 36% of CVI intensity was suppressed, and 46% of OV intensity was reduced immediately after the freshly coated lithium. The suppression of the intensity of the impurities reveals the chemical activity of lithium for effectively trapping impurities during plasma discharge.

Besides, the further experiment showed that when the base pressure of hydrogen gas was increased, the intensity of the impurities increased before and after the lithium coating. The base pressures considered before lithium are 0.6×10^{-4} Torr, 0.8×10^{-4} Torr, and 1.2×10^{-4} Torr and the base pressures after the lithium coating are 0.8×10^{-4} Torr, 1.2×10^{-4} Torr, and 1.6×10^{-4} Torr. Before the coating of lithium, a good plasma discharge could not be achieved at a base pressure of 1.6×10^{-4} Torr because density was too high, but a good and consistent plasma discharge was possible at that base pressure after the chamber was coated with lithium due to reduced wall recycling. It can be concluded that by increasing the tokamak's base pressure (the constant pressure maintained by adjusting the flow rate of working gas flow in the chamber tokamak through a piezoelectric gas valve), it is possible to bring the electron density back to the desired level. It is important to reduce the recycling so that the electron density during the discharge can be feedback-controlled by gas puffing rather than dictated by uncontrollable out-gassing during the discharge.

Compared with the case without lithium coating with the same gas puffing amount the observed reduction of electron density is a desired result.

Further investigation showed that after 300 shots of continuous plasma discharge following lithium coating, the intensity of the impurities increased by approximately 50% compared to the intensity with freshly coated lithium. The intensities decreased after 600 shots and remained almost the same after 900 shots. The intensity of the impurities after 300 shots of plasma discharges is in line with the reduction of the intensity of lithium emission after 300 shots because the intensity of lithium was reduced by half of its initial intensity after 300 shots, and intensity of impurities increased. The intensity of lithium emission decreased further after 600 shots and remained the same after 900 shots. It was expected that intensity of the impurities would increase after 600 and 900 shots because of the reduction in the intensity of the coated lithium, but the reverse was the case. The decrease of the intensity of the impurities could be because of the wall conditioning, which has been observed in the STOR-M tokamak before. As plasma is discharged repetitively, impurities are liberated from the plasma facing materials and are puffed out of the chamber, this explained why the intensity of the impurities reduced even though lithium was no longer playing any suppression role. Moreover, the depletion of the lithium after 300 shots of plasma discharges could be attributed to either the redistribution of the coated lithium to another part of the tokamak walls or puffing out of the lithium from the tokamak chamber. This study provides a guideline for future lithium coating experiments on the STOR-M to determine how frequent lithium coating is required to maintain its effectiveness. Current experiments with low lithium coating dose of 100 mg suggest that coating has to be re-applied less than 300 shots. Since no data was collected for the number of shots between freshly coated chamber and 300 shots, the exact number of shots a load of lithium coating can last is still unknown and remains as a future work.

It was also noted that plasma density after the freshly coated lithium decreased rapidly, increased after 300 shots, declined after 600 shots and stayed the same after 900 shots. These results suggest that when the inner walls of a tokamak are coated with lithium, the lithium reduces wall recycling and helps to control the intrinsic plasma density. The out-gassing from the wall through plasma-wall interaction in the case without lithum explains why the density is high compared with the case with lithium coating.

In the other experiment, the internal radial magnetic probe array was used to study the shielding effects of plasma on an external magnetic field generated by the resonant magnetic perturbations (RMP) coils. The magnetic field induced by the RMP coils with and without plasma were measured at four radial locations at the plasma edge. The net plasma effect was obtained by the difference between the two fields induced with plasma (vacuum chamber and plasma) and without plasma (vacuum chamber only). It was observed that plasma attenuates the applied RMP field as expected because the RMP field measured in plasma was 50% lesser than the RMP field measured in vacuum. The result shows that plasma is a good conductor, as the conductivity of a plasma can be determined by its ability to shield the external magnetic field greatly.

The time that is taken for the RMP field to propagate through the vacuum chamber and the plasma was also investigated. It was observed that the penetration time of the RMP field in the vacuum was greater than the RMP penetration time with plasma, that is, the applied RMP field propagates longer in a vacuum than in plasma. This result is unconventional because when a field is applied to a conductor, the field takes a longer time to penetrate. However, the reason for this unconventional result is still under investigation on the STOR-M tokamak.

5.2 Suggested Future Work

As discussed in Section 3.9 that impurities intensity measured by the collimators were not symmetric when the intensity distribution was plotted, the significant large asymmetry may be due to the stray intensities measured along with the intrinsic intensities by the collimators during plasma discharges. The stray intensities may come from either the reflection from the chamber wall or the emission caused by the plasma colliding with the material wall of the tokamak. In any future spectroscopy experiments, plasma position should be monitored from discharge to discharge to ensure that plasma is properly positioned and aligned along the magnetic field axis to eliminate the direct emission from the chamber wall due to the interaction of plasma with the impurities on the wall.

Moreover, one possible reason for why it was impossible to determine the RMP penetration time is because the radial locations where the RMP fields are being measured may be too close to the RMP coils. In the future, the issue can be resolved by increasing the distance between the RMP

coils and the magnetic probes. This can be done by locating the RMP coil on one side of the chamber and the magnetic probes on the other side. In this configuration, the RMP will be traveling through the plasma diameter. The RMP frequency should be reduced to increase skin depth effect on the RMP field.

REFERENCES

[1] International Atomic Energy Agency, *Fusion Physics*. Vienna: IAEA, 2012.

[2] W. Biel, "Tritium Breeding and Blanket Technology," 2014.

[3] J. Wesson, *Tokamak*. Oxford Science Publication, 2011.

[4] "New dawn: Chinese Scientists move step closer to creating 'artificial sun' in quest for limitless energy via nuclear fusion," 2016. [Online]. Available: http://www.scmp.com/tech/science-research/article/1909796/new-dawn-chinese-scientists-move-step-closer-creating. [Accessed: 18-Jun-2017].

[5] ITER, "The way to new energy." [Online]. Available: https://www.iter.org/mach. [Accessed: 25-Aug-2016].

[6] ITER, "ITER glossary." [Online]. Available: https://www.iter.org/glossary. [Accessed: 26-Aug-2016].

[7] R. Majeski, H. Kugel, R. Kaita, S. Avasarala, M. G. Bell, R. E. Bell, L. Berzak, P. Beiersdorfer, S. P. Gerhardt, E. Granstedt, and others, "The impact of lithium wall coatings on NSTX discharges and the engineering of the Lithium Tokamak eXperiment (LTX)," *Fusion Eng. Des.*, vol. 85, no. 7, pp. 1283–1289, 2010.

[8] G. Bateman, "MHD instabilities." MIT Press, Cambridge, MA, 1978.

[9] C. Xiao, D. Liu, S. Livingstone, A. K. Singh, E. Zhang, and A. Hirose, "Tangential and vertical compact torus injection experiments on the STOR-M tokamak," *Plasma Sci. Technol.*, vol. 7, no. 2, pp. 2701–2704, 2005.

[10] Y. Liu, "Toroidal Flow Velocity Measurement in the STOR-M Tokamak by Ion Doppler Spectroscopy," University Of Saskatchewan, Canada, 2012.

[11] S. Elgriw, "Effects of Resonant Magnetic Perturbations on the STOR-M Tokamak Discharges," University of Saskatchewan, Canada, 2014.

[12] D. K. Morozov, E. O. Baronova, and I. Y. Senichenkov, "Impurity radiation from a tokamak plasma," *Plasma Phys. Reports*, vol. 33, no. 11, pp. 906–922, 2007.

[13] E. Proust, L. Anzidei, G. Casini, M. D. Donne, L. Giancarli, and S. Malang, “Breeding blanket for DEMO,” *Fusion Eng. Des.*, vol. 22, no. 1–2, pp. 19–33, 1993.

[14] A. R. Raffray, M. Akiba, V. Chuyanov, L. Giancarli, and S. Malang, “Breeding blanket concepts for fusion and materials requirements,” *J. Nucl. Mater.*, vol. 307–311, no. 1 SUPPL., pp. 21–30, 2002.

[15] ITER, “Tritium Breeding.” [Online]. Available: www.iter.org/mach/TritiumBreeding. [Accessed: 01-Aug-2016].

[16] G. Zuo, J. Hu, J. Li, N. Luo, L. Hu, J. Hu, K. Chen, A. Ti, and L. Zhang, “Primary Results of Lithium Coating for the Improvement of Plasma Performance in EAST,” *Plasma Sci. Technol.*, vol. 646, no. 6, pp. 646–650, 2010.

[17] “Lithium.” [Online]. Available: en.wikipedia.org/wiki/Lithium. [Accessed: 26-Aug-2016].

[18] R. Majeski, “The Lithium Tokamak Experiment (LTX).” [Online]. Available: http://www.pppl.gov/sites/pppl/files/LTX.pdf. [Accessed: 26-Aug-2016].

[19] “Lithium Tokamak Experiment (LTX) device.” [Online]. Available: en.wikipedia.org/wiki/Lithium_Tokamak_Experiment. [Accessed: 26-Aug-2016].

[20] D. P. Lundberg, “Fueling Studies on the Lithium Tokamak Experiment,” Princeton University, 2012.

[21] M. G. Bell, H. W. Kugel, R. Kaita, L. E. Zakharov, H. Schneider, B. P. LeBlanc, D. Mansfield, R. E. Bell, R. Maingi, S. Ding, S. M. Kaye, S. F. Paul, S. P. Gerhardt, J. M. Canik, J. C. Hosea, and G. Taylor, “Plasma Response to Lithium-Coated Plasma-Facing Components in the National Spherical Torus Experiment,” *Plasma Phys. Control. Fusion*, vol. 51, no. 124054, pp. 1–12, 2009.

[22] M. B. Chowdhuri, R. Manchanda, J. Ghosh, S. B. Bhatt, A. Kumar, B. K. Das, K. A. Jadeja, P. A. Raijada, M. Kumar, S. Banerjee, N. Ramaiya, A. Mali, K. M. Patel, V. Kumar, P. Vasu, R. Bhattacharyay, R. L. Tanna, Y. S. Joisa, P. K. Atrey, C. V. S. Rao, D. C. Reddy, P. K. Chattopadhyay, R. Jha, and Y. C. Saxena, “Improvement of Plasma Performance with Lithium Wall Conditioning in Aditya Tokamak,” *Plasma Sci. Technol.*, vol. 15, no. 2, pp. 123–128, 2013.

[23] J. S. Hu, J. Ren, Z. Sun, G. Z. Zuo, Q. X. Yang, J. G. Li, D. K. Mansfield, L. E. Zakharov, and D. N. Ruzic, "An overview of lithium experiments on HT-7 and EAST during 2012," *Fusion Eng. Des.*, vol. 89, no. 12, pp. 2875–2885, 2014.

[24] J. Ren, J. S. Hu, G. Z. Zuo, Z. Sun, J. G. Li, D. N. Ruzic, and L. E. Zakharov, "First results of flowing liquid lithium limiter in HT-7," *R. Swedish Acad. Sci. Phys. Scr.*, vol. 2014, no. T159, pp. 1–5, 2014.

[25] J. Sánchez, M. Acedo, A. Alonso, J. Alonso, P. Alvarez, E. Ascasíbar, A. Baciero, R. Balbín, L. Barrera, E. Blanco, J. Botija, A. de Bustos, E. de la Cal, I. Calvo, A. Cappa, J. M. Carmona, D. Carralero, R. Carrasco, B. A. Carreras, F. Castejón, R. Castro, G. Catalán, A. A. Chmyga, M. Chamorro, L. Eliseev, L. Esteban, T. Estrada, A. Fernández, R. Fernández-Gavilán, J. A. Ferreira, J. M. Fontdecaba, C. Fuentes, L. García, I. García-Cortés, R. García-Gómez, J. M. García-Regaña, J. Guasp, L. Guimarais, T. Happel, J. Hernanz, J. Herranz, C. Hidalgo, J. A. Jiménez, A. Jiménez-Denche, R. Jiménez-Gómez, D. Jiménez-Rey, I. Kirpitchev, A. D. Komarov, A. S. Kozachok, L. Krupnik, F. Lapayese, M. Liniers, D. López-Bruna, A. López-Fraguas, J. López-Rázola, A. López-Sánchez, S. Lysenko, G. Marcon, F. Martín, V. Maurin, K. J. McCarthy, F. Medina, M. Medrano, A. V. Melnikov, P. Méndez, B. van Milligen, E. Mirones, I. S. Nedzelskiy, M. Ochando, J. Olivares, J. L. de Pablos, L. Pacios, I. Pastor, M. A. Pedrosa, A. de la Peña, A. Pereira, G. Pérez, D. Pérez-Risco, A. Petrov, S. Petrov, A. Portas, D. Pretty, D. Rapisarda, G. Rattá, J. M. Reynolds, E. Rincón, L. Ríos, C. Rodríguez, J. A. Romero, A. Ros, A. Salas, M. Sánchez, E. Sánchez, E. Sánchez-Sarabia, K. Sarksian, J. A. Sebastián, C. Silva, S. Schchepetov, N. Skvortsova, E. R. Solano, A. Soleto, F. Tabarés, D. Tafalla, A. Tarancón, Y. Taschev, J. Tera, A. Tolkachev, V. Tribaldos, V. I. Vargas, J. Vega, G. Velasco, J. L. Velasco, M. Weber, G. Wolfers, and B. Zurro, "Confinement transitions in TJ-II under Li-coated wall conditions," *Nucl. Fusion*, vol. 49, no. 10, pp. 1–10, 2009.

[26] D. K. Mansfield, D. W. Johnson, B. Grek, H. W. Kugel, M. G. Bell, R. E. Bell, R. V Budny, C. E. Bush, E. D. Fredrickson, K. W. Hill, D. L. Jassby, R. J. Maqueda, H. K. Park, A. T. Ramsey, E. J. Synakowski, G. Taylor, and G. A. Wurden, "Observations concerning the injection of a lithium aerosol into the edge of TFTR discharges," *Nucl. Fusion*, vol. 41, no. 12, pp. 1823–1834, 2001.

[27] G. Mazzitelli, M. L. Apicella, D. Frigione, G. Maddaluno, M. Marinucci, C. Mazzotta, V. Pericoli Ridolfini, M. Romanelli, G. Szepesi, and O. Tudisco, "FTU results with a liquid lithium limiter," *Nucl. Fusion*, vol. 51, no. 7, pp. 1–7, 2011.

[28] A. Hirose, C. Xiao, O. Mitarai, J. Morelli, and H. M. Skarsgard, "STOR-M Tokamak Design and Instrumentation," *Phys. Canada*, vol. 62, no. 2, pp. 111–120, 2006.

[29] B. D. Bondarenko, "Role played by O A Lavrent'ev in the formulation of the problem and the initiation of research into controlled nuclear fusion in the USSR," *Physics-Uspekhi*, vol. 44, no. 8, pp. 844–851, 2001.

[30] Merriam-Webster, "Dictionary." [Online]. Available: http://www.merriam-webster.com/dictionary/tokamak. [Accessed: 29-Feb-2016].

[31] F. F. Chen, *Introduction to Plasma Physics and Controlled Fusion*. Springer Science+Business Media, LLC, 2006.

[32] EuroFusion, "Magnets: Research for Tomorrow's Energy Supply." [Online]. Available: https://www.euro-fusion.org/fusion/jet-tech/magnets/. [Accessed: 20-May-2016].

[33] *Active Control of Magneto-hydrodynamic Instabilities in Hot Plasmas*, vol. 83. 2015.

[34] "Magnetic configuration of the tokamak," 2001. [Online]. Available: http://www-fusion-magnetique.cea.fr/gb/fusion/physique/configtokamak.htm. [Accessed: 29-Mar-2017].

[35] "The tokamak." [Online]. Available: http://www.ccfe.ac.uk/tokamak.aspx. [Accessed: 01-Feb-2016].

[36] "STOR-M Tokamak." [Online]. Available: http://plasma.usask.ca/fusion/storm.php. [Accessed: 14-Jun-2017].

[37] S. Elgriw, "Investigation of Magnetohydrodynamic Fluctuation Modes in the STOR-M Tokamak," University of Saskatchewan, 2009.

[38] J. E. Morelli, "Plasma Position Control in the STOR-M tokamak : A Fuzzy Logic Approach," University Of Saskatchewan, 2003.

[39] "Helmholtz Coil." [Online]. Available: en.wikipedia.org/wiki/Helmholtz_coil. [Accessed: 01-Apr-2016].

[40] Learning about Electronics, “LM741 Op-Amp pinout connections.” [Online]. Available: http://www.learningaboutelectronics.com/Articles/LM741-op-amp-pinout-connections. [Accessed: 01-Dec-2016].

[41] D. J. Griffiths, *Introduction to Electrodynamics*, 3rd ed. Upper Saddle River, New Jersey: Pearson Addison Wesley, 1999.

[42] I. H. Hutchinson, *Principles of Plasma Diagnostics*, 2nd ed. Cambridge University Press, United Kingdom, 2002.

[43] “Rogowski coil.” [Online]. Available: http://www.instructables.com/id/Make-a-Rogowski-coil/. [Accessed: 06-Jul-2017].

[44] W. Engelhardt, G. Fussmann, J. Gernhardt, E. Glock, F. Karger, O. Kliiber, G. Lisitano, H. M. Mayer, K. McCormick, D. Meisel, H. Murmann, S. Sesnic, and F. Wagner, “The Pulsator Tokamak,” *Nucl. Fusion*, vol. 25, no. 9, pp. 1059–1063, 1985.

[45] T. C. Hender, R. Fitzpatrick, A. W. Morris, P. G. Carolan, R. D. Durst, T. Edlington, J. Ferreira, S. J. Fielding, P. S. Haynes, J. Hugill, I. J. Jenkins, R. J. La Haye, B. J. Parham, D. C. Robinson, T. N. Todd, M. Valovic, and G. Vayakis, “Effect of resonant magnetic perturbations on COMPASS-C tokamak discharges,” *Nucl. Fusion*, vol. 32, no. 12, pp. 2091–2117, 1992.

[46] D. E. Roberts, D. Sherwell, J. D. Fletcher, G. Nothnagel, and J. A. M. de Villers, “Major disruptions induced by helical coils on the Tokoloshe tokamak,” *Nucl. Fusion*, vol. 31, no. 2, pp. 319–340, 1991.

[47] T. E. Evans, R. A. Moyer, J. G. Watkins, T. H. Osborne, P. R. Thomas, M. Becoulet, J. A. Boedo, E. J. Doyle, M. E. Fenstermacher, K. H. Finken, R. J. Groebner, M. Groth, J. H. Harris, L. G. Jackson, R. J. La Haye, C. J. Lasnier, S. Masuzaki, N. Ohyabu, D. G. Pretty, H. Reimerdes, T. L. Rhodes, D. L. Rudakov, M. J. Schaffer, M. Wade, G. Wang, W. P. West, and L. Zeng, “Suppression of Large Edge Localized modes in High Confinement DIII-D Plasmas with a Stochastic Magnetic Boundary,” *Nucl. Mater.*, vol. 92, no. 23, pp. 691–696, 2004.

[48] T. E. Evans, M. E. Fenstermacher, R. A. Moyer, T. H. Osborne, J. G. Watkins, P. Gohil, I.

Joseph, M. J. Schaffer, L. R. Baylor, M. Becoulet, J. A. Boedo, K. H. Burrell, J. S. Degrassie, K. H. Finken, T. Jernigan, M. W. Jakubowski, C. J. Lasnier, M. Lelmen, A. W. Leonard, J. Lonnroth, E. Nardon, V. Parail, O. Schmitz, B. Unterberg, and W. P. West, "RMP ELM suppression in DIII-D plasmas with ITER similar shapes and collisionalities," *Nucl. Fusion*, vol. 48, no. 24002, pp. 1–10, 2008.

[49] "User's manual for PI-MAX 3 ICCD Camera," Princeton Instruments, a division of Roper Scientific, Inc. Trenton, NJ, USA, Sep-2012.

[50] Oriel_Instruments, "Typical Spectra of ORIEL calibration lamps," *User Manuals*. [Online]. Available: https://www.newport.com/medias/sys_master/images/images/h55/hfd/8797293281310/Typical-Spectra-of-Spectral-Calib-Lamps.pdf. [Accessed: 20-May-2016].

[51] W. Zhang, C. Xiao, G. D. Conway, O. Mitarai, A. Sarkissian, H. M. Skarsgard, L. Zhang, and A. Hirose, "Improved confinement and edge plasma fluctuations in the STOR-M tokamak," *Am. Inst. Phys.*, vol. 4, no. 10, pp. 3277–3284, 1992.

[52] A. Kramida, Y. Ralchenko, J. Reader, and NIST Atomic Spectra Database Team, "NIST Atomic Spectra Database (version 5.3)," *National Institute of Standards and Technology, Gaithersburg, MD*, 2015. [Online]. Available: http://physics.nist.gov/asd. [Accessed: 20-Aug-2016].

[53] G. R. McKee, D. J. Schlossberg, and M. W. Shafer, "Ultrafast ion temperature and toroidal velocity fluctuation spectroscopy diagnostic design," *Am. Inst. Phys.*, vol. 79, no. 10, pp. 1–4, 2008.

[54] D. Mueller, P. H. LaMarche, M. G. Bell, W. Blanchard, C. E. Bush, C. Gentile, R. J. Hawryluk, K. W. Hill, A. C. Janos, F. C. Jobes, D. K. Owens, G. Pearson, J. Schivell, M. A. Ulrickson, C. Vannoy, K. L. Wong, and H. F. Dylla, "Dicharge Cleaning on Tokamak Fusion Test Reactor after Boronization," *Vac. Sci. Technol.*, vol. 9, no. 5, pp. 2713–2715, 1991.

[55] S. Ishii, "Discharge cleaning for a tokamak," *Plasma Phys. Fusion Technol.*, vol. 15, no. 23, pp. 489–498, 1983.

[56] S. D. Bello, P. Innocente, M. Agostini, A. Alfier, F. Auriemma, A. Canton, L. Carraro, R. Cavazzana, G. De Masi, G. Mazzitelli, S. Munaretto, and P. Scarin, “Lithiumization effects on density control and plasma performance in RFX-mod experiment,” pp. 1–8, 2010.

[57] A. S. Razumovsky, “Skin Effect,” vol. 4, pp. 541–543, 1992.

[58] N. A. Krall and A. W. Trivelpiece, *Principles of Plasma Physics*. San Francisco, 1986.

[59] J. A. Romero, J.-M. Moret, S. Coda, F. Felici, and I. Garrido, “Development and Validation of a Tokamak Skin Effect transformer Model,” *Nucl. Fusion*, vol. 52, no. 2, pp. 1–17, 2012.